2018-03-28

Nano-pore Confinement Adsorption and Diffusion Effects on Duvernay Gas Condensate Production Behavior

Shihan, Zhang

UNIVERSITY OF CALGARY

Nano-pore Confinement Adsorption and Diffusion Effects on Duvernay Gas Condensate Production Behavior

by

Shihan Zhang

A THESIS

SUBMITTED TO THE FACULTY OF GRADUATE STUDIES

IN PARTIAL FULFILMENT OF THE REQUIREMENTS FOR THE

DEGREE OF MASTER OF SCIENCE

GRADUATE PROGRAM IN CHEMICAL AND PETROLEUM ENGINEERING

CALGARY, ALBERTA

MARCH, 2018

Abstract

In recent years, shale exploration and production becomes economic by establishing multi-stage hydraulic fracturing along horizontal wells. However, shales are different than conventional reservoirs by complex phase behaviors, fluid storage mechanisms, and flow mechanisms. In order to evaluate the shale gas reservoir behaviors, the effect of nano-pore confinement because of extremely small pore sizes is included. Critical properties are altered by the confinement effect, resulting in a gas phase behavior difference than that in conventional reservoirs. Moreover, to describe the shale gas storage mechanisms, an adsorption effect is considered. It is widely believed that without considering adsorbed gases, an under-estimation of reserves by more than 10% may happen. Additionally, in order to model the gas flow mechanisms in shale, multi-mechanistic flow regimes are applied in both matrix and fractures. Due to the nature of ultra-low permeability in the matrix, fluid flow is responding not only to a pressure gradient, but also to a concentration gradient.

Acknowledgements

I would like to thank my supervisor Dr. Zhangxing John Chen, not only for his infinite help and insightful comments throughout my research, but also for his care and mentorship during my study here at the University of Calgary. Without his patience and encouragement, this work would not have been possible. Dr. Chen is not only an amazing supervisor, but he is also a wonderful mentor in my life who guided my thoughts.

I would also like to thank Dr. Robert Gordon Moore and Dr. Shengnan Nancy Chen for their valuable suggestions and also their interests in serving as my committee members.

Additionally, I would like to thank our Reservoir Simulation Group for supporting me with resources and finical help during my study. Also, special thanks go to our group members, Dr. Kai Zhang and Ms. Jamie McInnis, for their significant contributions to my academic and research.

Finally, I would like to thank my families for their supports and all my friends for helping and the memorable time we share.

Table of Contents

List of Tables

List of Figures and Illustrations

List of Symbols, Abbreviations and Nomenclature

Symbol	Definition
A	Helmholtz free energy
a	Van der Waals attraction correction factor
A_p	Transversal section area of the pore
b	Van der Waals molar volume correction factor
C_1	Fitting parameter, dimensionless
C_2	Fitting parameter, dimensionless
c_i	Moles of concentration
D_i	Pore diffusion coefficient,cm^2/s
$D_{i,eff}$	Effective pore diffusion coefficient,cm^2/s
J_i	Diffusion mas flux, $\mathrm{mol \cdot cm/cm^3/s}$
K_{rg}	Relative permeability of gas phase, dimensionless
K_{ro}	Relative permeability of oil phase, dimensionless
K_m	Matrix permeability, md
m	Mass, lbs
M	Molecular weight, lbm/lbmole
n	Total number of components, lbmol/kg
n_i'	Total number of moles adsorbed from mixture, lbmol/kg
P	Average reservoir pressure, psia
P_L	Langmuir pressure, psia

P_c	Critical pressure, psia
P_{cb}	Critical pressure at bulk, psia
P_{pc}	Pseudo critical pressure of the gas mixture, psia
P_{ci}	Critical pressure of a single component i, psia
P_{cp}^*	Critical pressure at nanoscale, psia
ΔP_c^*	Relative deviated critical pressure, dimensionless
R	Gas universal constant, J/K-mole
r_p	Pore radius, nm
T	Average reservoir temperature, ºF
T_c	Critical temperature, ºF
T_{pc}	Pseudo critical temperature of the gas mixture, ºF
T_{ci}	Critical temperature of a single component i, ºF
T_{cb}	Critical temperature at bulk, ºF
T_{cp}^*	Critical temperature at nanoscale, ºF
ΔT_c^*	Relative deviated critical temperature, dimensionless
T_r	Reduced temperature, ºF
V	Volume
V'	Volume of adsorbed phase
x_i	Liquid phase mole fraction of component i
y_i	Gas phase mole fraction of component i

Greek

α	Langmuir adsorption constant the amount adsorbed
σ	Molecule diameter, nm
φ	Fugacity coefficient
φ_a	Fugacity coefficient of adsorbed phase
μ	Viscosity, cp
μ_i'	Adsorbed phase viscosity, cp
ρ_b	Bulk rock density, g/cc
ρ_{CH4}	Mass density of methane in pore, g/cc
ρ	Free gas phase density, g/cc
ρ_s	Adsorbed phase density, g/cc
$\rho_{s,mix}$	Adsorbed phase density of the gas mixture, g/cc
ω	Acentric factor to measure the non-sphericity
γ_i	Activity coefficient in adsorbed phase of component i
Φ_g	Gas phase potential
β_p	Non-Darcy flow coefficient.

Superscript

‘	Adsorbed phase
0	Standard stat
*	Before contact with adsorbent

Chapter One: **Introduction**

1.1 Introduction

In recent years, industries have moved toward exploration and production from unconventional energy resources such as tight oil and gas, shale oil and gas, coalbed methane (CBM), and gas hydrates. In the past, the technical challenges and high operation costs limited exploration and production from unconventional oil and gas reservoirs. However, as the technology improved, shale gas production becomes economical by drilling horizontal wells and establishing multi-stage hydraulic fracturing along the wells. According to the Alberta Energy Regulator (2015), the recoverable shale gas in place in Alberta, Canada is 3,424 trillion cubic feet, while that of shale oil is 423.6 billion barrels. However, the daily production of shale oil and gas in Alberta, Canada is neglectable. Therefore, shale oil and gas demonstrate high reserves but low exploration and production, which indicates that the production of shale and tight resources is expected to offset the decline in conventional productions. Additionally, according to the National Energy Board (2014), shale gas accounted for approximately 4% of the total Canadian natural gas production while tight gas accounted for 47% of that. By 2025, the National Energy Board (NEB) expects that tight and shale gas productions together will account for about 80% of new drillings and represent 50% of Canada's natural gas productions. By 2035, the NEB (2013) expects conventional gases account for only 6% of Canada's natural gas productions, while tight gases make up 62% and shale gases account for 28%. As a result, shale and tight gas will play a more important role in future gas production.

In the 1990s, shale oil and gas were classified to be unrecoverable resources due to the technical limits and the nature of shale low permeability and small pore size. In recent years, this type of reservoirs is still considered to be the most challenging reservoirs due to their complex phase

behaviors, unique fluid storage mechanisms, and fluid flow mechanisms. Accordingly, understanding these properties becomes extremely requisite for future oil and gas productions. In this study, I will establish a compositional gas condensate model by considering a nano-pore confinement effect, an adsorption effect, and a diffusion effect, respectively.

In order to evaluate shale gas phase behaviors, a nano-pore confinement effect is included in the present work. Due to the nature of extremely small pore sizes, generally 2 nm to 50 nm diameters for shale reservoirs, there exist the interactions between molecules and pore walls, which is known as nano-pore confinement (Rahmani, 2012). To achieve a successful evaluation of this phenomenon, a correlation suggested by Zarragoicoechea and Kuz (2004) is applied to modify critical properties to demonstrate how these properties affect phase behaviors. Recently, Bilgesu (2013) developed an adsorbed phase density corrector to account for how the adsorbed phase density affects critical properties, since a sorption process may exist on shale surfaces.

By considering shale fluid storage, an adsorption effect is described in the present work. A sorption process occurs in organic matters and adsorbed gas is released from organic matrix as pressure depletes (Lu et. al, 1995). Based on previous research (Rajput, 2016), not considering this adsorption storage mechanism will lead to an under-estimation of reserves by more than 10%. Therefore, accurately estimating adsorbed gases will become important in shale gas reservoirs. In order to model the effect of adsorption, a variety of theoretical methods are developed in this study including a Monolayer Langmuir Model, which is then extended to an Extended Langmuir Model. The most common way to simulate the effect of adsorption in commercial simulators is the Extended Langmuir (EL) Model, which is the extension of Monolayer Langmuir (ML) model by extending a single component system to a multi-component system. However, this method does not take the thermodynamic consistency of adsorption in shales into account. Accordingly, an ideal

adsorbed solution theory (IAST) is applied to take a compositional change into account and then incorporated with the EL model.

Moreover, for considering flow mechanisms in shales, multi-mechanistic flow regimes are implemented in both matrix and fractures. Due to the nature of low permeability in the matrix (Ghorayeb and Firoozabadi, 2000), a flow regime is not only contributed by a pressure gradient, but also contributed by a concentration gradient. Therefore, a multi-mechanistic flow containing both convective flow (Darcy's Law) and diffusive flow (Fick' Law) in the matrix is performed. With the knowledge of effective coefficients, correlations in CMG GEM (2016) will be applied to calculate gas and liquid phase diffusional fluxes. Similarly, due to the presence of freeways in fractured zones, a higher velocity than the normal Darcy's flow velocity may occur. Consequently, a multi-mechanistic flow containing both Darcy's flow and non-Darcy flow in fractured zones is imposed. In this approach, a Forchheimer equation beta correction will be implemented to adjust the non-Darcy flow coefficients.

To achieve modelling of the aforementioned processes, a compositional reservoir simulator will be used to model the shale gas condensate phase behaviors and gas production performances. First, in WinProp (2016), a compositional Duvernay gas condensate model with nano-pore confinement and adsorption effects considered is developed to estimate the shale gas phase behaviors. Additionally, in CMG GEM (2016), a three-dimensional, three-phase, dual-porosity and dual-permeability compositional Duverany gas condensate model is established to display shale gas production performances. In this way, this study will be able to describe how these phenomena in shales affect fluid behaviors and oil and gas production profiles

1.2 Problem Statement

The objective of this study is to develop a compositional gas condensate model to describe how shales are different from conventional reservoirs. In addition, during this research study, the following questions will be addressed:

I. The best way of hydraulic fracture modeling: Do the results display a difference between a planar fracture model and a complex fracture model? Are there any differences upon considering a flow-back process?

II. Is nano-pore confinement important for Duvernay shale gas condensate reservoirs? What is the best option to model the confinement effect? What does the comparison of results yield between only considering the effect of a nano-pore size and considering the effects of both a nano-pore size and the adsorbed phase density? What impacts do they have on future oil and gas production profiles?

III. Is a sorption process important for Duvernay shale gas condensate reservoirs? What is the best option to model the adsorption effect? What does the comparison of results generate among the ML model, the EL model, and the IAST-EL model? What impacts do they have on future oil and gas production profiles?

IV. Is diffusive flow important for Duvernay shale gas condensate reservoirs? What impact does it have on future oil and gas production profiles?

Chapter Two: **Literature Review**

2.1 Numerical Modeling of Shale Reservoirs

2.1.1 Naturally Fractured Shale

In this study, a naturally fractured Duvernay shale gas condensate reservoir is modelled. Shale and tight formations are generally naturally fractured, which evidences that this type of reservoirs contains two parts of porous domains as the matrix and fractures. The matrix has very low permeability, generally less than 0.001 mD, but relatively high porosity, which acts as storage units and contains most of fluids. On the other hand, fractures have very low porosity but comparatively higher permeability, which acts as freeways for the fluid flow.

This type of reservoirs has not been deeply studied by researchers, since it used to be not economic due to the nature of its low permeability in the matrix and small pore sizes in the range of nano meter. In recent years, as energy deficiency increases, shale gas condensate operations become economic by drilling horizontal wells and establishing multi-stage hydraulic fracturing along the wells. This fracturing process usually operates by injecting slick water with cross linkers to increase reservoir pressure above the principal stress to create network fractures, which act as freeways to connect the matrix-fractures.

However, shale gas reservoirs are significantly different from conventional gas reservoirs by the phase behaviors, fluid storage mechanisms, and fluid flow mechanisms. Therefore, understanding these properties become extremely needed for future productions. This study will establish a gas condensate model by considering confinement, adsorption, and diffusion effects, respectively.

For considering the phase behavior, the effect of confinement is included in this research. Due to the nature of extremely small pore sizes, the phase behavior in the shale gas reservoirs is different from that in conventional reservoirs. There exist the interactions between molecules and pore walls

as pore sizes decrease to nano meter ranges, which is known as confinement. Critical properties including critical pressure and critical temperature will be altered by the confinement effect (Rahmani, 2012). Consequently, the two-phase envelope will also shrink to demonstrate that the phase behavior in the shale gas reservoirs is different than that in conventional reservoirs.

For considering the fluid storage mechanism, an adsorption effect is described in the present work. Gas are stored as free gas and adsorbed gas in shales initially. Shale matrix acting as storage units and porosities are distinguished into three different types: inorganic matter, organic matter, and nature fractures originally (Lu et. al, 1995). A sorption process only occurs in the organic matter; i.e., adsorbed gases will be released from the organic matrix as pressure depletes. During the fluid flow-back period, free gases transport to the fractured zones and will be produced first as pressure drops. When pressure depletes further under the dew point pressure, adsorbed gas will be released from the matrix.

Moreover, for considering the flow mechanism, multi-mechanistic flow regimes are applied in both matrix and fractures. Due to the nature of low permeability in the matrix, a flow regime is not only contributed by a pressure gradient. But also, transportation is contributed by a concentration gradient (Ghorayeb and Firoozabadi, 2000). Accordingly, a multi-mechanistic flow containing Darcy's flow and diffusive flow in the matrix is imposed. Similarly, due to the existence of freeways in fractured zones, a higher velocity than the normal Darcy's flow velocity occurs. Therefore, a multi-mechanistic flow containing Darcy's flow and non-Darcy flow in fractured zones is implemented in the present work.

This study will discuss how these phenomena in shales affect fluid phase behaviors and future gas production behaviors. First, different approaches will be established to model the naturally fractured reservoirs and the hydraulic fracturing process. Next, a nano-pore confinement effect on

phase behaviors in shales will be described in Chapter 3 and modelling of adsorption phenomenon in shales will be conducted in Chapter 4.

2.1.2 Dual-Porosity Model

Dual-porosity modelling is a common way to model naturally fractured reservoirs. In order to describe this dual-porosity method, Warren and Root (1963) developed a sugar-cube model to represent a reservoir porosity system, as shown in Figure 2.1. This methodology suggests that using a cubic grid system to describe the matrix porosity and fracture porosity in the same grid block in reservoir modelling is effective. Therefore, each grid block has both matrix property and fracture property.

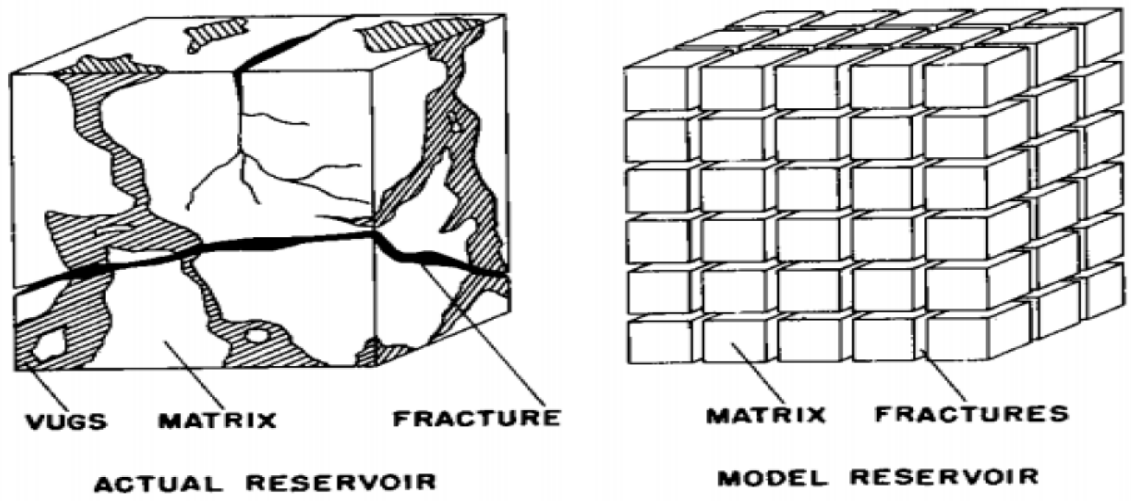

Figure 2.1: Sugar cube model (Warren and Root, 1963)

However, there are limitations of a dual-porosity model. That is, permeability is only assigned to the fractures, since fracture permeability is significantly larger than the matrix permeability, which

means there is no fluid flow taking place between the matrix blocks. In other words, fluid flow between the matrix and matrix will be ignored in this mechanism, as shown in Figure 2.2.

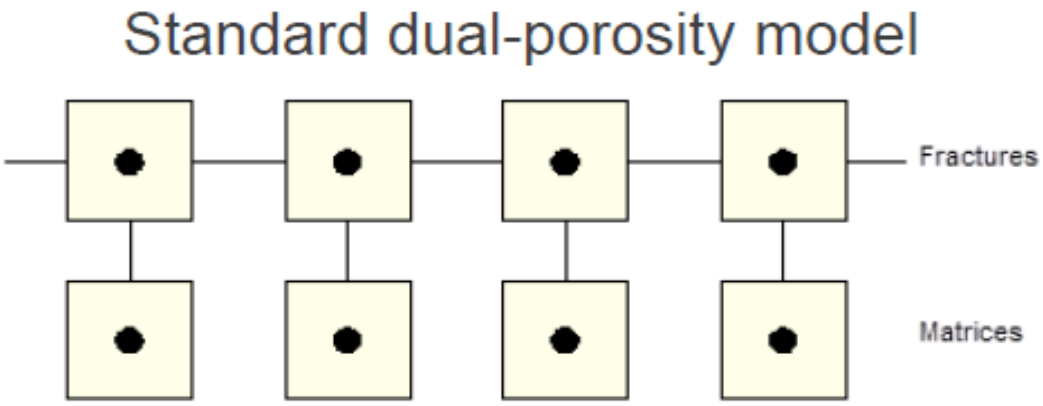

Figure 2.2: Standard dual-porosity model (Modelling of Shale, Tight Oil and Gas Reservoirs CMG, 2015)

2.1.3 Dual-Permeability Model

The dual-permeability method is developed based on previous work to assign permeability values to both matrix and fractures in the same grid block. Therefore, simulators can not only model the fluid flow between the matrix and fractures, but also can model the fluid flow between the matrix and matrix, as shown in Figure 2.3. In the matrix, multi-mechanistic flow containing Darcy's flow and diffusive flow is present in shales as we discussed previously. A diffusional flux can play a significant role, which contributes to the fluid flow; i.e., it can be the main driving force at the matrix-matrix and matrix-fracture interfaces. Consequently, diffusive flow between the matrix-matrix should be accounted by assigning permeability values to the matrix.

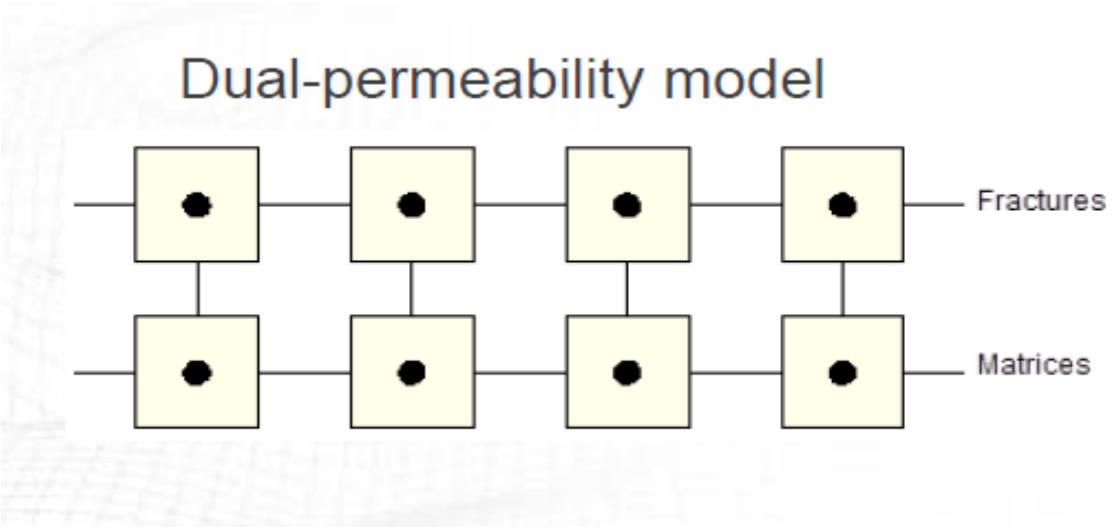

Figure 2.3: Standard dual-permeability model (Modelling of Shale, Tight Oil and Gas Reservoirs CMG, 2015)

However, there still exist limitations of this dual-permeability model. Shale matrix has three distinct porosities including inorganic matter, organic matter, and natural fractures. A sorption process only occurs in the organic matter, which means adsorbed gas are stored on organic surfaces. Therefore, a triple-porosity and triple-permeability model is required to distinguish these three different porosity parts. Sun et al. (2015) conducted a case study to compare a single porosity model, a single permeability model, a dual-porosity model, a dual-permeability model, and also a triple-porosity model. This approach ended up with a conclusion that the dual-permeability method was sufficient to model shale reservoirs and more complex models would not improve the modelling results. Since this study will validate results through the commercial simulator CMG GEM (2016), a dual-permeability model will be used to balance the accuracy and computational time.

2.2 Hydraulic Fracture Modeling in Shale Reservoirs

2.2.1 Planner Facture Model

As we described, due to the low permeability of matrix in shale reservoirs, hydraulic fracturing needs to be conducted to improve the connection between the matrix-matrix and matrix-fractures. In reality, fracture growth is similar to Figure 2.4. How to incorporate this fracture growth process in a reservoir simulator is a complex task. There is lots of ongoing research on the fracture growth modelling in simulators. A planner fracture model with a locally refined grid system in fractured zones is developed to simulate a fracture network in CMG software (Warpinski et. al, 2008). Due to the extremely low permeability of the matrix, pressure transients in shales and other tight reservoirs are extremely slow. This type of reservoir cannot be assumed to be a pseudo steady state and the flow behaviors need to be modeled more explicitly. Therefore, the Locally Spaced-Logarithmically Refined-Dual Permeability method (LS-LR-DK) is implemented to solve the aforementioned problem (Warpinski et. al, 2008). Since the fastest flow speed occurs around fractures, local refinement is used to simulate more accurately around the fractured zones. As the slowest flow speed occurs where the fracture zones are far away, a logarithmically spaced grid is used at such places. In this way, such models have more refinements around the fractured zones and less refinements where the fracture zones are far away to balance the accuracy and computational time. This planner fracture methodology can be adjusted by modification of the fracture porosity, fracture permeability, fracture width, fracture half-length, and fracture spacing.

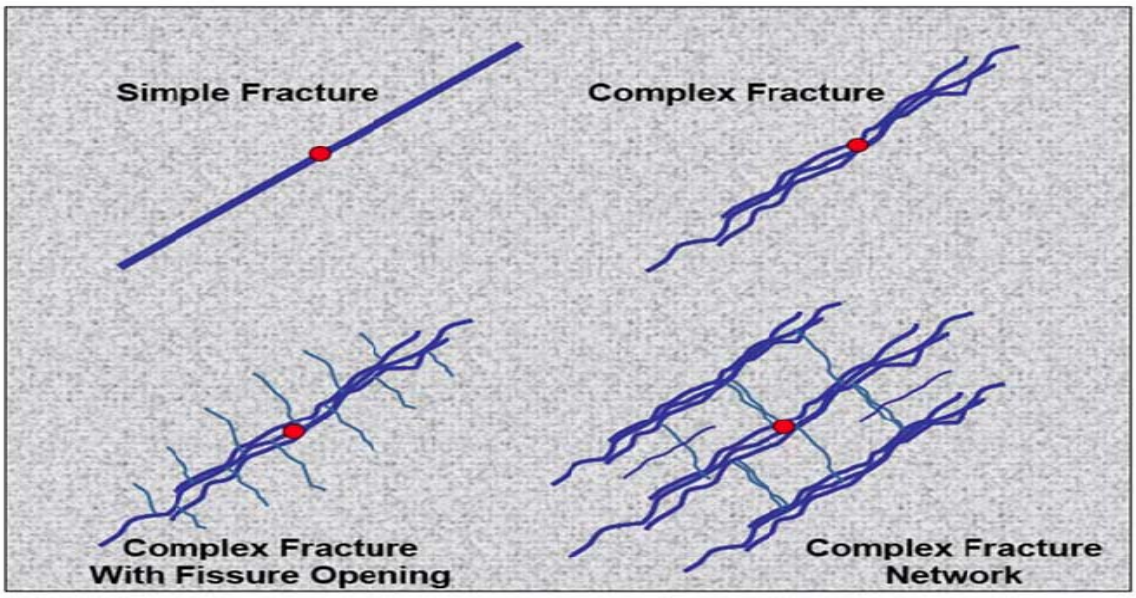

Figure 2.4: Types of fracture growth (Warpinski et. al, 2008)

Nevertheless, there still exist limitations of the planner fracture method to model the pressure depletions in fractured zones. That is mainly because in this method real fractures are represented by a 2 feet thick pseudo fracture, which uses a 2 feet thick pseudo fracture to simulate the real fracture growth, and such fracture permeability is corresponding to an effective permeability in a 2 feet grid cell. However, if the pressure depletion is significantly large around the fractured zones, a 2 feet thick pseudo fracture is not sufficient and an even finely gridded cell is required.

2.2.2 Complex Facture Model

Accordingly, the present approach extended a planner fracture model by adding a stimulated reservoir volume to depict network fractures, named a complex fracture model. A stimulated reservoir volume (SRV) uses an even finer gridded cell near the fractured zones to depict the network factures and it can be adjusted by modification of the fracture porosity, fracture

permeability, and fracture width (Mayerhofer, 2010). Therefore, a complex fracture model will increase the refinement area around the fractured zones and reduce computational time where fractured zones are far away.

This study will simulate network fractures using both a planner fracture model and a complex fracture model through the CMG GEM (2016) and compare their results.

2.2.3 Modeling of Non-Darcy Flow in Fractures

By establishing hydraulic fracturing along wells, the fluid flow capacity will increase and then result in an increment of velocity higher than the normal range of Darcy flow around the fractured zones, which is known as the non-Darcy flow, as shown in Figure 2.5. Such an increment of velocity will require an extra definition to depict this changing of pressure potential.

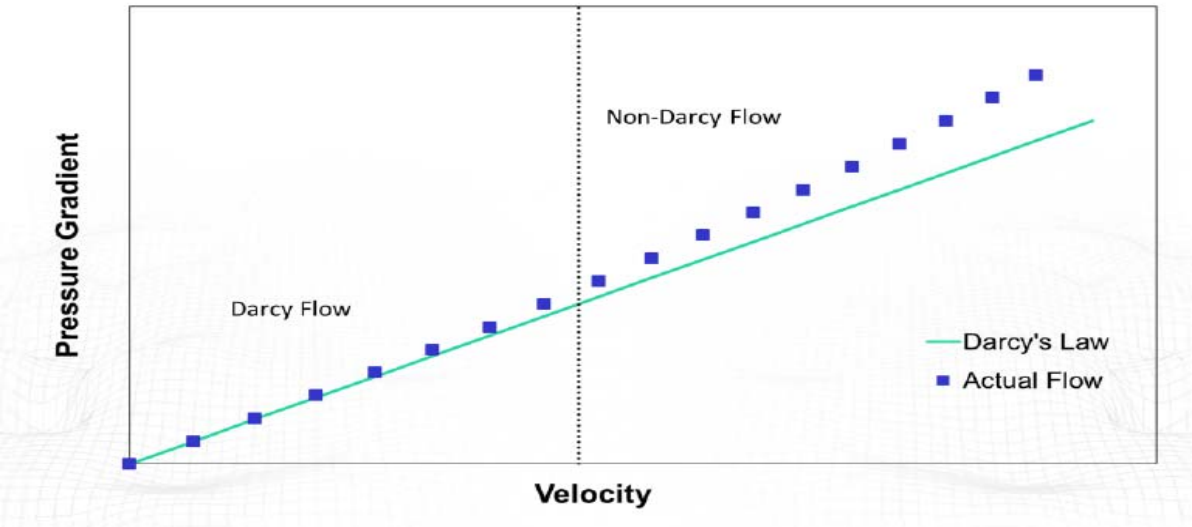

Figure 2.5: Pressure gradient with velocity of actual flow (Modelling of Shale, Tight Oil and Gas Reservoirs CMG, 2015)

In porous media, this extra velocity flow can be modelled by the Forchheimer equation to yield a relationship between the pressure gradient and the gas flow velocity as follows:

$$-\nabla\Phi_g = \frac{\mu_g}{KK_{rg}}\overrightarrow{u_g} + \beta\left|\overrightarrow{u_g}\right|\overrightarrow{u_g} \tag{2.1}$$

$$\beta_p = \frac{\alpha_p}{(KK_{rp})^{N1_p}(\emptyset S_p)^{N2_p}} \tag{2.2}$$

where Φ_g stands for the gas phase potential and β_p is the non-Darcy flow coefficient.

The value of $N1_p$ is highly related to the fracture width; i.e., $N1_p$ increases as the fracture width increases. Generally, a larger width, larger than real, is used during the modelling of hydraulic fracturing. Since a larger width will reduce the computational time and yield a result at the acceptable level. Therefore, the non-Darcy flow coefficient will be underestimated, which means that the calculated velocity will be lower than the actual velocity to result in an underestimation of the fluid flow. There is lots of research going on concerning the predication of the beta factor (Cooke, 1973), which represents the non-Darcy flow caused by a higher velocity than the normal range. Cooke (1973) presented that there is a very large non-Darcy effect in shales and provided a suggestion of coefficient values. Similarly, Evans and Civan (1994) collected 183 data sets from a variety of porous media under different conditions and provided a reasonable beta estimation. In this approach, the Forchheimer equation beta correction will be applied to adjust the non-Darcy flow in CMG GEM (2016):

$$\beta_{coor} = \left(\frac{K_f}{K_{eff}}\right)^{2-N1g} = \left(\frac{W_{grid}}{W_f}\right)^{2-N1g} \tag{2.3}$$

2.2.4 Modeling of Flow-Back

As we know, horizontal multi-stage hydraulic fracturing needs to be established for tight and shale reservoirs due to the low permeability in the matrix. During this fracturing process, slick water incorporated with linear gels will be injected to a reservoir to increase the pressure beyond its principal stress to create fractures. Therefore, during the fluid flow-back period, there will be water remaining in the reservoir. This phenomenon can be modeled by rewriting the initial water saturation of the fractured zones to depict the water remaining when the flow-back process has been completed. As a result, a relatively higher initial water saturation is left around the stimulated regions and linearly decreases away from the stimulated regions, as shown in Figure 2.6. Similarly, the conductivity yields the same trend, since hydraulic fracturing increases the permeability and the exposure areas around the stimulated regions.

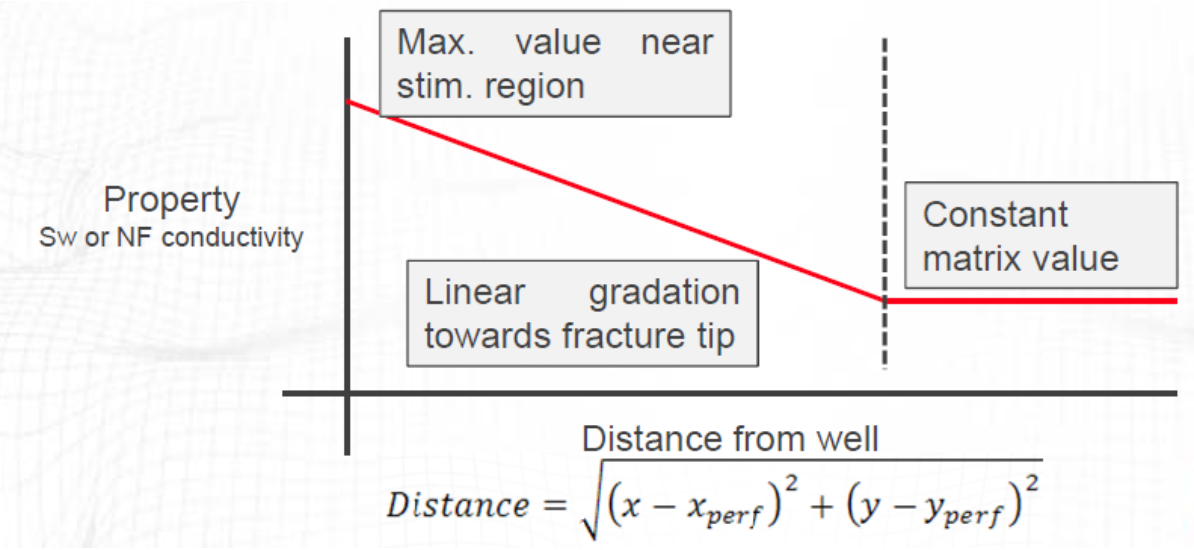

Figure 2.6: Water saturation with distance from well (Modelling of Shale, Tight Oil and Gas Reservoirs CMG, 2015)

2.3 Confinement Effect in Shale Gas Reservoirs

As pore sizes decrease to nano-scale, there exist the interactions between molecules and pore walls. That is known as the confinement effect and it will lead to the thermo-physical properties different from their bulk values (Gelb et al., 1999). Previously, Ortiz et al. (2005) showed that critical properties such as critical pressure and critical temperature tend to decrease with declining pore sizes when considering the effect of confinement, and then the two-phase envelope will also shrink. Similarly, Rahmani (2012) investigated the effect of pore confinement on single and multi-component shale gas thermodynamics, and found that critical properties and the fluid behaviors confined in small micro-pores are significantly different than their bulk values. A number of theoretical studies shown that a pore size in the range of 2 nm to 50 nm can causes a significant shift of critical properties and fluid phase behaviors (Firincioglu et. al, 2012).

To quantify the effects of molecule-wall interactions on the phase behaviors, there are two main different methods, including the modification of critical properties as a function of pore sizes, and the inclusion of capillary pressures during the equilibrium calculations (Nojabaei et. al, 2013). For numerical simulators, such as CMG WinProp, it is only able to use the method of modifying critical properties. Accordingly, the modification of critical properties such as critical temperatures and critical pressures will be utilized to simulate the confinement effect in this study.

In order to take the confinement effect into account, a correlation developed by Zarragoicoechea and Kuz (2004) based on the van der Waal equation of state is applied to modify critical property shifting of a pure gas component, which then results in how these properties affect the phase behaviors. The Zarragoicoechea and Kuz (2004) equation demonstrates that critical temperature and critical pressure will shift as a function of the pore radius.

First, a reduced axial pressure by using the van der Waals parameters based on the Helmholz

free energy in a pore space can be expressed as (Zaraagoicoechea, 2004):

$$P_{ZZ}^{*} = \frac{T^{*}}{v^{*}-b} - \frac{a-2\left(\frac{c_1}{\sqrt{A_p}}\right)-2\left(\frac{c_2}{A_p}\right)}{v^{*2}} \tag{2.4}$$

where

$a = \frac{16\pi}{9}$

$b = \frac{2\pi}{3}$

$c_1 = 4.6571$

$c_2 = -2.1185$

$A_p = \pi\left(\frac{r_p}{\sigma}\right)^2$

When considering the confinement effect, the equation parameters are adjusted to be:

$$P_{ZZ}^{*} = \frac{T^{*}}{v^{*}-b_{adj}} - \frac{\left(\frac{a_{adj}}{a}\right)\left[(a-2\left(\frac{c_1}{\sqrt{A_p}}\right)-2\left(\frac{c_2}{A_p}\right)\right]}{v^{*2}} \tag{2.5}$$

For each single component, its bulk properties are calculated using equations as:

$$T_{cb}^{*} = \frac{8a_{adj}}{27b_{adj}} \tag{2.6}$$

$$P_{cb}^{*} = \frac{8a_{adj}}{27b_{adj}^{2}} \tag{2.7}$$

$$V_{cb}^{*} = 3b_{adj} \tag{2.8}$$

By combination of such bulk property equations and equation (2.5), the fluid component parameters inside pore spaces can be described as:

$$T_{cp}^{*} = \frac{8a_{adj}}{27b_{adj}}\left(\frac{a_{adj}}{a}\right)\left[(a - 2\left(\frac{c_1}{\sqrt{A_p}}\right) - 2\left(\frac{c_2}{A_p}\right)\right] \tag{2.9}$$

$$P_{cp}^{*} = \frac{\left(\frac{a_{adj}}{a}\right)\left[(a-2\left(\frac{c_1}{\sqrt{A_p}}\right)-2\left(\frac{c_2}{A_p}\right)\right]}{27b_{adj}^{2}} \tag{2.10}$$

Therefore, a relationship between the dimensionless temperature shifting and a pore size is established by using the aforementioned two correlation sets equation (2.11). The relationship between dimensionless pressure shifting and a pore size can be expressed based on the same method (Zarragoicoechea, 2004), which is shown as equation (2.12):

$$\Delta T_{c}^{*} = \frac{T_{cb}^{*} - T_{cp}^{*}}{T_{cb}^{*}} = 0.9409\left(\frac{\sigma}{r_p}\right) - 0.2415\left(\frac{\sigma}{r_p}\right)^{2} \tag{2.11}$$

$$\Delta P_{c}^{*} = \frac{P_{cb}^{*} - P_{cp}^{*}}{P_{cb}^{*}} = 0.9409\left(\frac{\sigma}{r_p}\right) - 0.2415\left(\frac{\sigma}{r_p}\right)^{2} \tag{2.12}$$

where

$$\sigma = 0.244^{3}\sqrt{\frac{T_{cb}^{*}}{P_{cb}^{*}}}$$

r_p is the pore radius in nm, σ is the molecule diameter in nm, T^*_{cb} is the fluid critical temperature at bulk in ºF, T^*_{cp} is the fluid critical temperature under a pore confinement effect in ºF, ΔT^*_c is the dimensionless critical temperature shifting, P^*_{cb} is the fluid critical pressure at bulk in psia, P^*_{cp} is the fluid critical pressure under a pore confinement effect in psia, and ΔP^*_c is the dimensionless critical pressure shifting.

These correlations demonstrate critical temperature and critical pressure shifts as a function of the pore radius. Since a pore size is extremely small as nano scale in shale formations, critical property shifting should be considered due to the presence of a confinement effect. However, all these shifting equations ignore an adsorption effect on organic rich shale surfaces, which will also change critical properties. Rahamani (2012) stated that because of the adsorption phenomenon in organic rich shale formations, this confinement effect can be even more significant than only considering pore sizes' effect. Additionally, the free gas density yields a decrement trend as pressure decreases, and then the density difference between free gas and adsorbed gas will become even larger, which indicates that the adsorbed phase density needs to be adjusted. Therefore, this study will overcome aforementioned problems by adding an adsorbed density correction in Chapter 3 and demonstrate how this density correction factor will affect the confinement effect in nano-scale shale reservoirs.

There was lots of work developed previously to present the importance of adjusting an adsorbed phase density (Akkutlu, 2012). Ray (2010) conducted an experiment to describe the molecular density of methane at 176 ºF in organic pores, as shown in Figure 2.7. The vertical axis stands for the density of methane in g/cc and the horizontal axis stands for the distance from the pore walls in Å. From this experiment, adsorption layers are found to be the closest to the surfaces and have heavier density. Next to adsorption layers are the phase-transition layers, which have smaller

density and are more mobile to move out of pores. In addition, transition layers have the adsorption and desorption process under equilibrium. Next to the phase-transition layers are free gases in the centres of pores, which have the smallest density and become the easiest one to move out of pores. Consequently, adsorption layers are the closest to the pore walls and under the strongest influence of the molecule-wall interactions to become even harder to move out. The adsorbed phase density, therefore, becomes a crucial parameter that needs to be included in the confinement system. In this study, a semi-analytical correlation between critical properties and the adsorbed phase density will be presented later in Chapter 3.

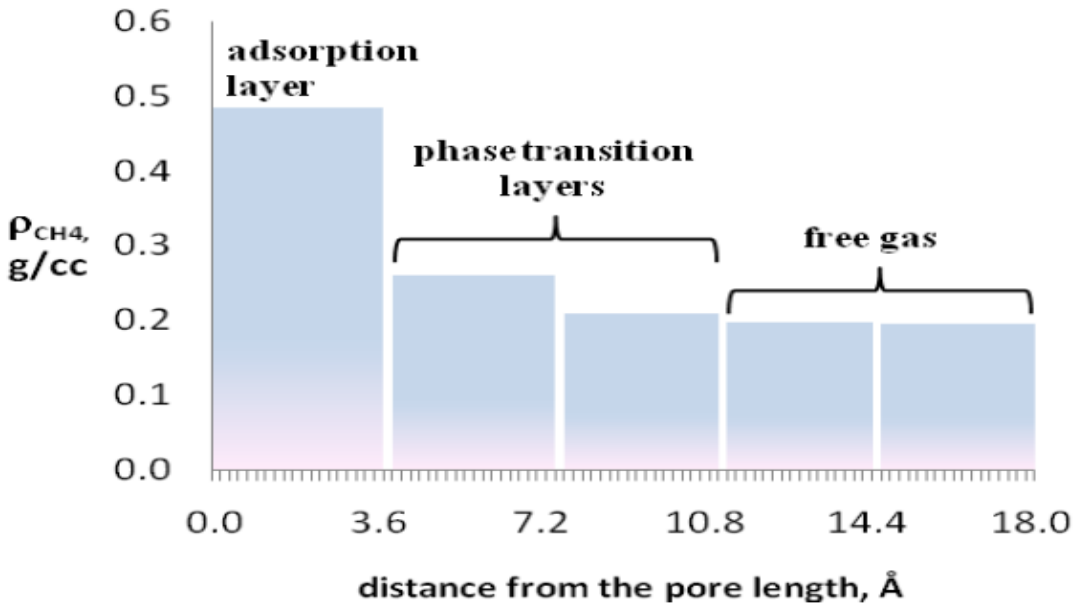

Figure 2.7: Molecular layer density of methane at 176 ºF across the half-length of a 3.6 nm organic slit-pore (Ray, 2010).

Moreover, Kai (2016) developed the total energy difference of CH_4 and C_2H_6 in a nanotube, as shown in Figure 2.8. In this approach, CH_4 has been found to be closer to the centre of the nanotube compared with C_2H_6, which means C_2H_6 is much closer to the wall. As we described earlier, if the component is closer to walls, it will be under a stronger influence of the molecule-wall interactions and become harder to move out of the nanotube. Accordingly, C_2H_6 is harder to move out of pores and CH_4 is easier to move out of pores in this case. The conclusion can be extended to light components that are less likely to be adsorbed in pore spaces and can move out of the pore spaces easily. This phenomenon also is indicative of the fact that the adsorbed phase density is an important parameter that needs to be included in the confinement system, since it is denser than free gases and under stronger interactions.

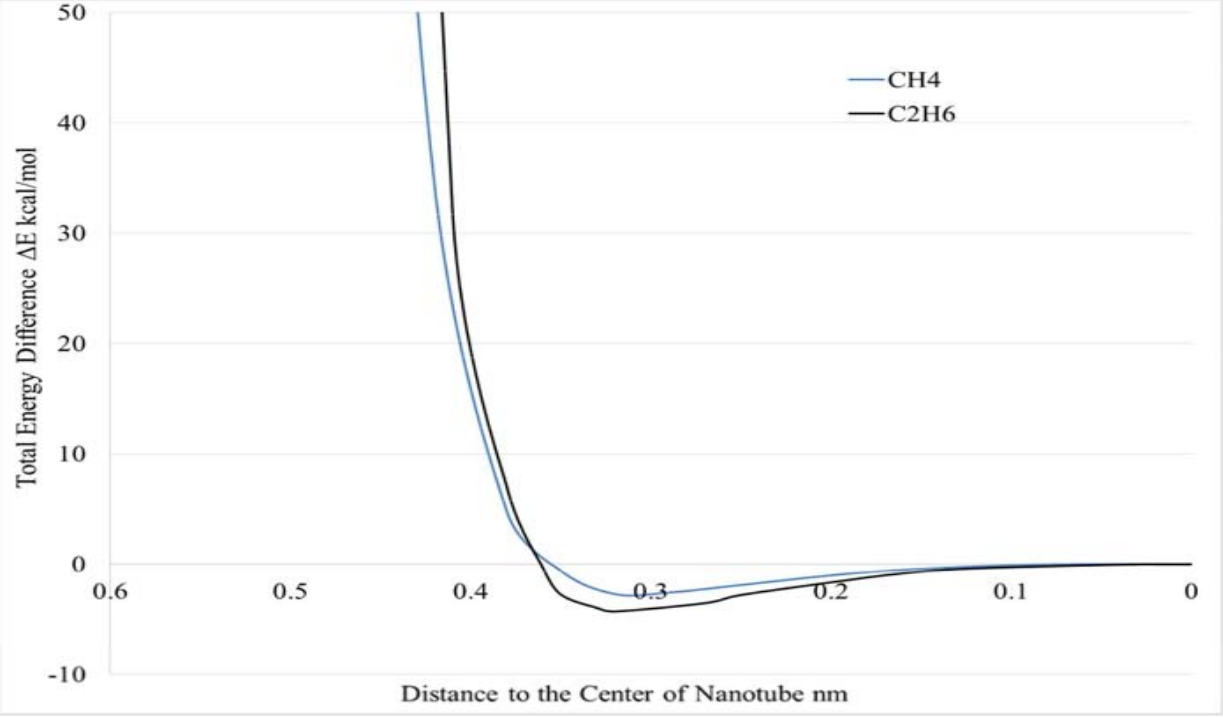

Figure 2.8: Total energy difference between CH_4 and C_2H_6 in nanotube (Zhang, 2016)

2.4 Adsorption Effect in Shale Gas Reservoirs

Gas is stored as both free gas and adsorbed gas in shale reservoirs. Shale matrix acts as the storage units and the porosities are distinguished into three different parts: inorganic matter, organic matter, and nature fractures originally. A sorption process occurs in the organic matter and adsorbed gases are stored on organic surfaces. As pressure depletes under the dew point pressure, the condensate will dropout and adsorbed gas will be released from organic matrix to contribute to the gas production. Based on previous research (Rajput, 2016), without considering this storage mechanism will lead to an under-estimation of reserves by more than 10%. Figure 2.9 presents the adsorbed fluids' contribution to the total gas in place, which is based on the data from Sportfire and published resources.

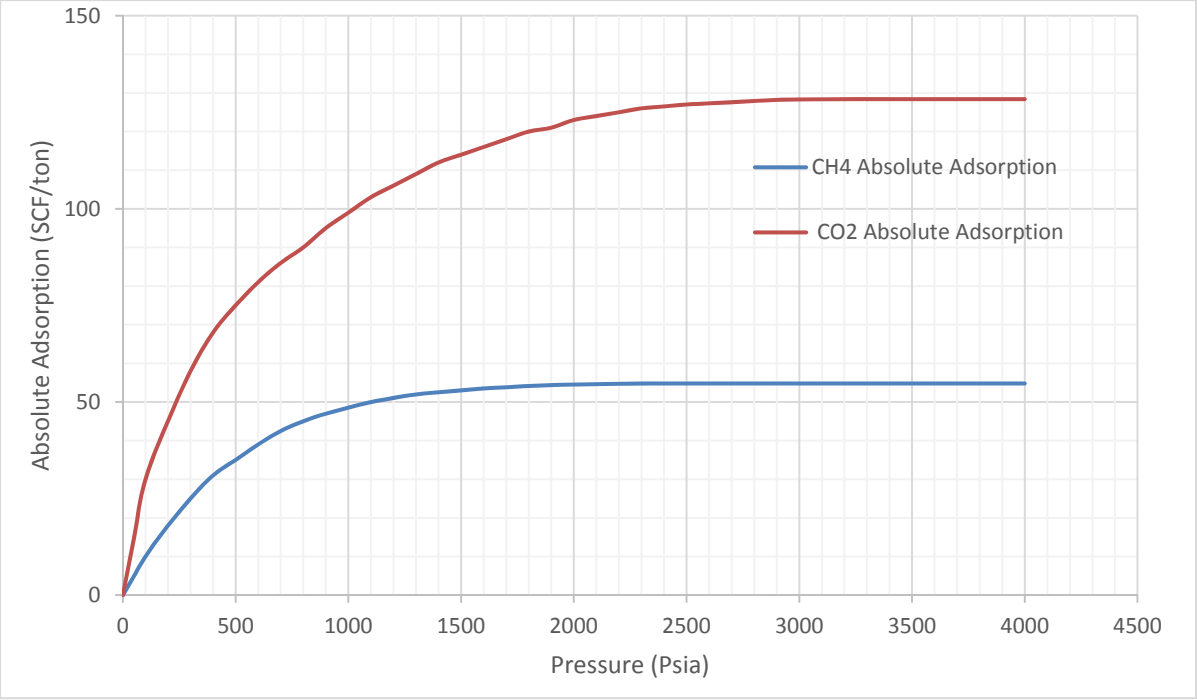

Figure 2.9: Absolute adsorption with pressure of CH_4 and CO_2

Since the effect of adsorption needs to be considered in shale gas reservoirs, its modelling, therefore, becomes crucial. In order to model such an effect, a variety of theoretical methods are developed including the Monolayer Langmuir Method, the Extended Langmuir Method, and also the ideal adsorbed solution theory combined with the Extended Langmuir Method (Myers et. al, 1965). The methodology used for simulating an adsorption effect in CMG GEM (2016) is the Extended Langmuir (EL) Method, which is the extension of the Monolayer Langmuir (ML) model by extending a single component system to a multi-component system. Equation (2.13) represents a ML model for a single component system and equation (2.14) presents an EL model for a multi-component system (Arri et al., 1992), shown as:

$$V_i = \frac{V_{Li} P_g}{P_{Li} + P_g} \tag{2.13}$$

$$V_i = \frac{V_{Li}(P_g y_i)}{P_{Li} + \sum_j \frac{P_{Li}}{P_{Lj}} (y_i P_g)} \tag{2.14}$$

where

V_i= Adsorbed volume of component i in unit of SCF/ton

V_{Li}= Langmuir volume constant of pure component i in unit of SCF/ton

y_i= Gas phase molar composition of component i

P_g= Gas phase pressure in unit of psia

P_{Li}= Langmuir pressure constant of pure component i in unit of psia

As seen from the Ml and EL equations, the sorption limits keep the same for all components. In other words, the adsorbed phase is only regarded as a free gas phase and the compositional change

during depletion is neglected. However, in reality, as reservoir pressure depletes, the liquid will also drop out in the bulk; i.e., compositions will not only be the gas phase. Therefore, a compositional change will take place in shale reservoirs, which evidences that thermodynamics is inconsistent.

In order to take the thermodynamic consistency into account, Myers and Prausnitz (1965) proposed the ideal adsorbed solution theory (IAST). In the IAST, the adsorbed phase is treated as an ideal solution, and a hypothesis is proposed that the free gas phase and adsorbed gas phase equilibrium is under the same way of the vapor phase and liquid phase equilibrium. Then, based on this ideal gas-adsorbed phase equilibrium assumption, Manik (1999) suggested equation (2.15) to describe the thermodynamic equilibrium between the free gas phase and the adsorbed gas phase as follows:

$$P_g \varphi_i y_i = P_i{}^0 \varphi_i{}^0 x_i{}^0 \tag{2.15}$$

where

P_g= Gas phase pressure in unit of psia

$P_i{}^0$= Pressure of pure component i at standard condition in unit of psia

φ_i= Gas phase fugacity coefficient of pure component i

$\varphi_i{}^0$= Gas phase fugacity coefficient of pure component i at standard condition

y_i= Gas phase molar composition of component i

$x_i{}^0$= Adsorbed phase molar composition of component i at standard condition

Due to high costs and low economical returns, there were limited studies about the adsorption effect in shale gas condensate reservoirs, especially limited studies including a compositional change during the sorption process. However, as multi-stage hydraulic fracturing along horizontal wells becomes economic for shale formations, fully understanding the effect of adsorption in a thermodynamically-consistent way becomes significant. Subsequently, in Chapter 4, I will describe the EL model and the IAST-EL model as well as how these methods affect oil and gas production in detail.

2.5 Diffusion Effect in Shale Gas Reservoirs

In conventional reservoirs, Darcy's flow is used to describe the relationship between a fluid flow rate and a pressure gradient. However, as permeability decreases to micro or nano Darcy, the time of transient flow will be longer and the pressure gradient will not respond to the flow mechanism (Ertekin et. al, 1986). A concentration gradient needs to be considered as another important driving mechanism (Ghorayeb and Firoozabadi, 2000). Therefore, a flow regime is not only contributed by a pressure gradient, which is known as convective flow (Darcy's Law). But also, the transport is contributed by a concentration gradient, which is known as diffusive flow (Fick' Law). This indicates that if its permeability is in the order of nano Darcy to micro Darcy, multi-mechanistic flow needs to be performed, which contains both the convective flow and diffusive flow.

Moreover, since the adsorption effect is included in this study, the modelling of diffusive flow becomes even more crucial. As pressure drops to a dew point pressure, not only will the liquid drop out, but also the desorption process exists. This dropped out liquid and desorbed fluid will block the fluid flow path and gas will lose flowing capacity at pore surfaces. Consequently, a diffusional flux can play an important role in the flow mechanism, which acts as the main driving

force at the matrix-matrix and matrix-fracture interfaces (Lenormand et. al, 1998). Therefore, modelling of the diffusive flow becomes even more significant if the effect of adsorption is included.

There is lots of work on this type of study that demonstrates the presence of such an effect and the importance of diffusion for fractured reservoirs (Ayala et. al, 2006). These researchers all ended up with a conclusion that diffusional mass transfer at surfaces can determine the recovery efficiency.

In order to fully understand the diffusive flow, a diffusional flux equation is described in terms of a concentration gradient as:

$$J_i = -\bar{\rho} \sum_{k=1}^{nc-1} D_{ik}^{Fick} \nabla x_k \tag{2.16}$$

In this study, changing of a diffusional flux across the boundaries and the matrix–fracture interfaces will be ignored to balance the computational time. Then the diffusional flux equation can also be described in terms of the effective diffusion coefficient as follows:

$$N_i = -D_{i,eff} \nabla c_i \tag{2.17}$$

Therefore, the effective coefficients can be obtained from these equations. With the values of the effective coefficients, correlations in the CMG GEM (2016) will be applied to calculate the gas and liquid phase diffusional fluxes. Details about the diffusion effect on oil and gas production behaviors will be presented in Chapter 5

Chapter Three: **Confinement Effect on Shale Gas Condensate Phase Behavior**

3.1 Methodology

3.1.1 EOS Development

An equation of state (EOS) is a mathematical way to measure a relationship between pressure, volume, and temperature, also known as PVT. It is widely used to describe the phase behaviors such as the fluid properties, phase transitions, and mixture phase equilibrium. The van der Waals equation of state (1873) investigates real gas phase behaviors and then many different types of EOSs have been established, including the Peng-Robinson (PR) and Soave-Redlich-Kwong (SRK) EOSs. In these EOSs, real gas is modeled by adding constants, including constant a to account for pressure drops due to molecular force attractions, constant b to account for the volume of molecules that has been ignored, and the acentric factor to measure the non-sphericity of molecules (McCain, 1990). However, due to the presence of extremely small pore sizes and the adsorption on organic surfaces for shale reservoirs, the aforementioned EOSs are of limited use. Therefore, the van der Waals EOS is extended by adding parameters to take a pore radius and the adsorbed phase density into account.

First, the van der Waals equation of state (1873) is expressed as:

$$P = \frac{RT}{V-b} - \frac{a}{V^2} \tag{3.1}$$

The van der Waals equation of state can be extended by adding parameters of critical temperature, critical pressure, and an acentric factor. For WinProp (2016) calculations, the Peng-Robinson EOS parameters are applied:

$$P = \frac{RT}{V-b} - \frac{a(T)}{V^2+Vb(1+c)-cb^2} \quad (3.2)$$

where

$$b = \frac{\Omega_b R T_c}{P_c}$$

$$a(T) = \frac{\Omega_a R^2 {T_c}^2}{P_c}\alpha(T)$$

$$\alpha(T) = (1 + k(1 - T_r^{0.5}))^2$$

$$k(\omega) = C_0 + C_1\omega + C_2\omega^2$$

a accounts for molecular force attraction, b accounts for the volume of molecules that has been ignored, and ω is the acentric factor to measure the non-sphericity of molecules.

3.1.2 Adsorbed Phase Density

Since the hydrocarbon-hydrocarbon interactions and the eccentricity have been ignored in this study, Dubinin (1960) proposed that the adsorbed phase density is related to constant b. Subsequently, Rahmani (2012) extended this approach and demonstrated a correlation to estimate the initial amount of gas that has been adsorbed, where constant b is expressed as a function of critical pressure and critical temperature. Accordingly, the adsorbed phase density equation can be described as:

$$\rho_s = \frac{M}{b} \quad (3.3)$$

where

$b = \frac{RT_c}{8P_c}$

$a = \frac{27R^2{T_c}^2}{64P_c}$

T_c is the critical temperature in ºF, P_c is the critical pressure in psia, M is the molecular weight in $\frac{\text{lbm}}{\text{lbm mole}}$, and ρ_s is the adsorbed phase density in g/cc.

Based on such an equation, the adsorbed phase density for a pure component can be calculated. However, because a reservoir contains multi-components, this research needs to evaluate the adsorbed phase density as a gas mixture. Then Kay's mixing rule is applied (Kay, 1969):

$$\rho_{s,mix} = \sum_i^n x_i \rho_s \tag{3.4}$$

where

$P_{pc} = \sum_i^n x_i P_{ci}$

$T_{pc} = \sum_i^n x_i T_{ci}$

A pseudo-critical temperature and pseudo-critical pressure are imposed to evaluate the adsorbed gas mixture and then substituted back to the density equation to estimate the adsorbed phase density as a gas mixture.

3.1.3 Adsorbed Phase Density Correction

In Chapter 2, a correlation between the critical property shifting and the pore radius is established. Now, how the adsorbed phase density affects the critical property shifting also needs to be included. Bilgesu (2013) developed ρ_{corr} to modify the confinement equation with the assumption

that the adsorbed phase density is treated as a constant. Also, by applying a gas law, a proportional correlation between the pressure and density can be established as $P \propto \rho$, while an inverse proportional correlation between temperature and density can also be established as $T \propto \frac{1}{\rho}$. Bilgesu (2013) presented the following shifting equations by considering both a pore size and the adsorbed phase density correction:

$$\Delta T_c^* = \frac{T_{cb}^* - T_{cp}^*}{T_{cb}^*} = \frac{0.9409}{\rho_{corr}}\left(\frac{\sigma}{r_p}\right) - \frac{0.2415}{\rho_{corr}}\left(\frac{\sigma}{r_p}\right)^2 \quad (3.5)$$

$$\Delta P_c^* = \frac{P_{cb}^* - P_{cp}^*}{P_{cb}^*} = 0.9409\,\rho_{corr}\left(\frac{\sigma}{r_p}\right) - 0.2415\,\rho_{corr}\left(\frac{\sigma}{r_p}\right)^2 \quad (3.6)$$

where

$$\sigma = 0.244^3\sqrt{\frac{T_{cb}^*}{P_{cb}^*}}$$

$$\rho_{corr} = \frac{\rho}{\rho_s - \rho}$$

r_p is the pore radius in nm, σ is the molecule diameter in nm, ρ_{corr} is the dimensionless density correction by considering the adsorbed phase, T_{cb}^* is the fluid critical temperature at bulk in ºF, T_{cp}^* is the fluid critical temperature under a pore confinement effect in ºF, ΔT_c^* is the dimensionless critical temperature shifting, P_{cb}^* is the fluid critical pressure at bulk in psia, P_{cp}^* is the fluid critical pressure under a pore confinement effect in psia, and ΔP_c^* is the dimensionless critical pressure shifting.

3.2 Confinement Effect Case Study when Considering a Pore Size - Case One

In this study, a PVT model that uses Duvernay gas condensate data is established and then property shifting parameters are added to see how the confinement affects phase behaviors. First, the equations that were suggested by Zarragoicoechea and Kuz (2004) are applied to modify the critical temperatures and critical pressures. These corrected values are used to calculate the phase envelope and other fluid properties for a gas mixture by using WinProp (2016). The correlations described in Chapter 2, equations (2.11) and (2.12), are used in this approach, which only consider the influence of a pore size. Moreover, the adsorbed phase density correction has been ignored in this case. Table 3.1 shows the compositions and properties of components that are used in this case, which are based on the information from Accumap.

Table 3.1: Component compositions and properties for case one

Component	Composition	MW	P_{cb}^{*} (atm)	T_{cb}^{*} (K)	σ (nm)
CO_2	0.0053	44.01	72.80	304.20	0.030
N_2	0.0057	28.01	33.50	126.20	0.028
CH_4	0.6845	16.04	45.40	190.60	0.030
C_2H_6	0.1016	30.07	48.20	305.40	0.037
C_3H_8	0.0505	44.10	41.90	369.80	0.043
IC_4	0.0082	58.12	36.00	408.10	0.049
NC_4	0.0127	58.12	37.50	425.20	0.049
IC_5	0.0164	72.15	33.40	460.40	0.054
NC_5	0.0138	72.15	33.30	469.60	0.055
FC_6	0.0308	86.00	32.46	507.50	0.057
C_{7+}	0.0705	145.00	22.38	641.58	0.078

Figure 3.1 shows the dimensionless critical temperature and critical pressure differences by changing of the pore sizes. This shifting becomes larger as the pore size decreases, which can conclude that the confinement effect needs to be included if the pore size is less than 50 nm. Since the adsorbed phase density correction has been ignored in this study, the values of the dimensionless temperature shifting and pressure shifting are the same since the same equation is applied. Therefore, dimensionless critical property shifting is imposed to represent both the dimensionless critical temperature and critical pressure differences.

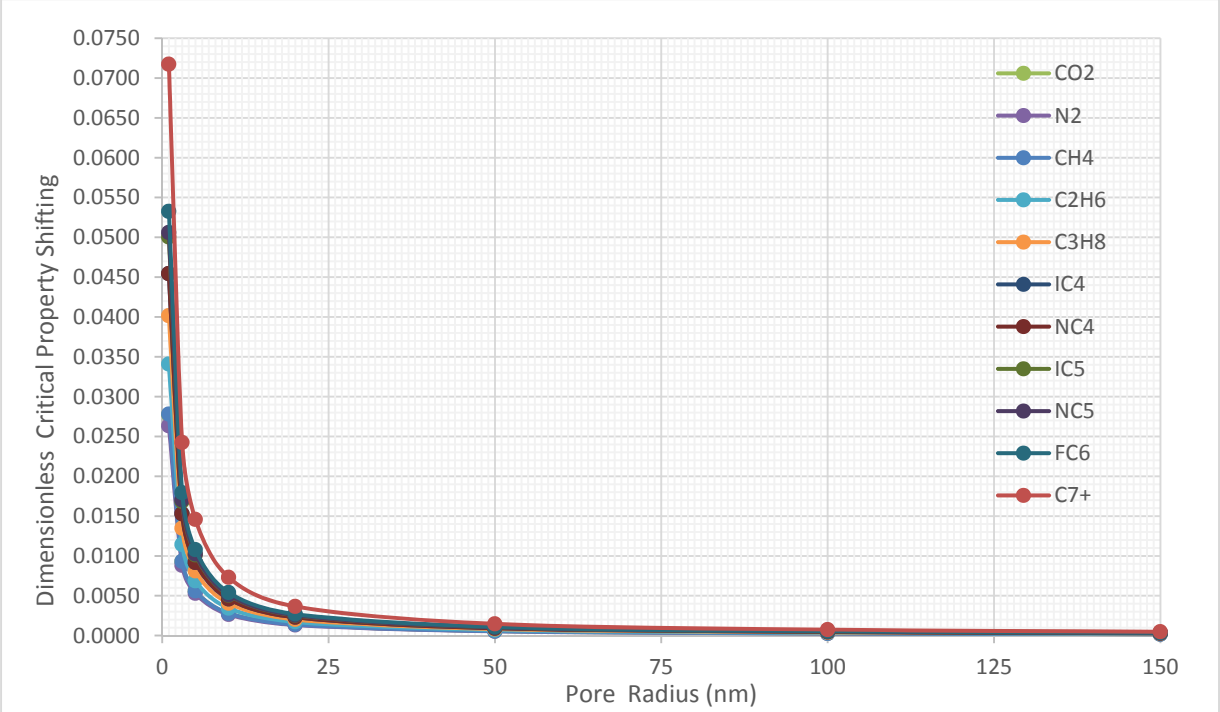

Figure 3.1: Dimensionless critical property shifting with pore radius

As discussed in Chapter 2, the dimensionless critical property difference is larger for those heavy components compared to the light components. Figure 3.2 presents that the dimensionless critical property shifting increases with the increasing of molecular weights at different pore sizes. Also,

it is found that this shifting phenomenon becomes extremely significant as the pore size decreases, which supports the conclusion that the confinement effect needs to be considered for shale reservoirs' phase behavior modeling.

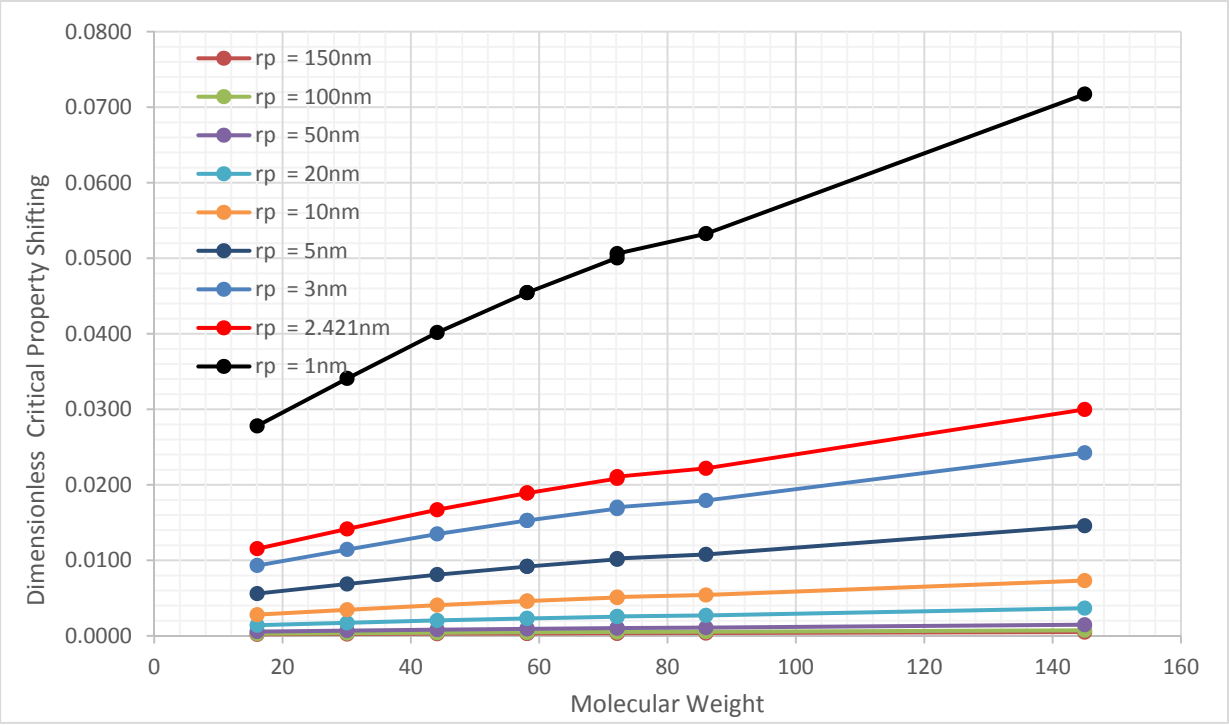

Figure 3.2: Dimensionless critical property shifting with molecular weights at different pore sizes

Similarly, Figure 3.3 shows that the critical temperature deviation is changing with the pore radius and Figure 3.4 shows the critical pressure deviation is changing with the pore radius. Both plots indicate that the deviation starts when the pore radius is decreased to 50 nm and this deviation becomes significantly large when the pore radius is decreased to 5 nm.

In this research, the pore radius is calculated to be 2.4 nm, which is based on the knowledge of the matrix porosity and matrix permeability. Since the pore size is comparably smaller than 50 nm,

the confinement effect must be included to deepen the understanding of the adsorption effect on shale gas condensate production behaviors.

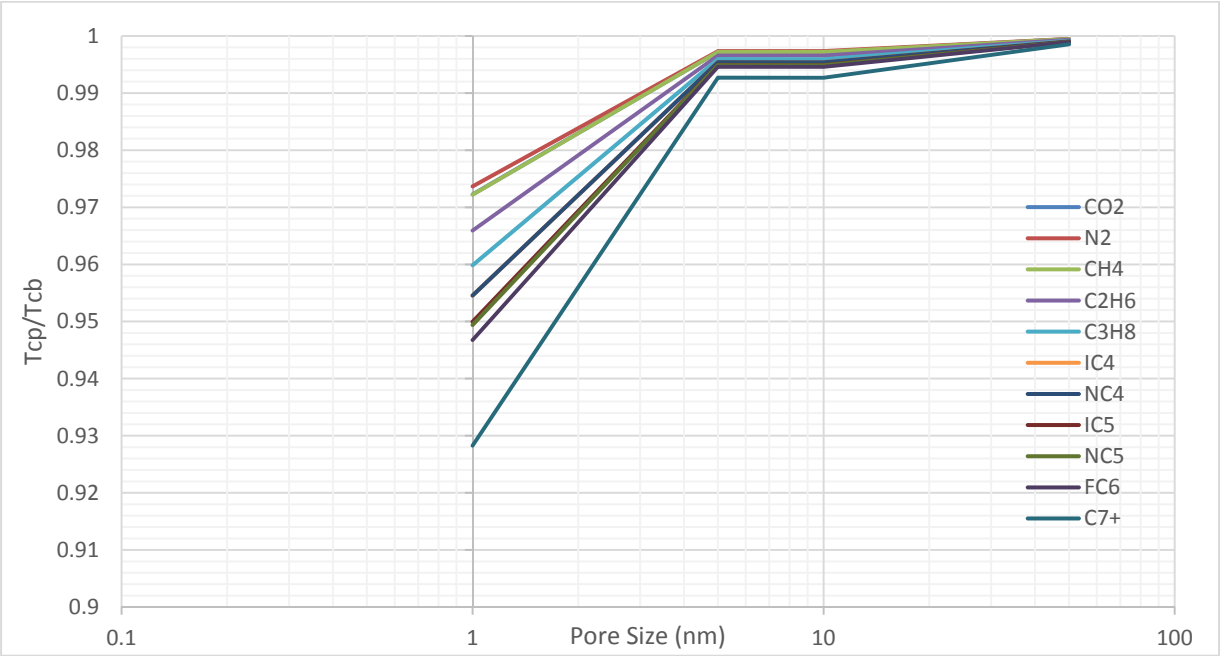

Figure 3.3: Critical temperature deviation changing with pore radius trend

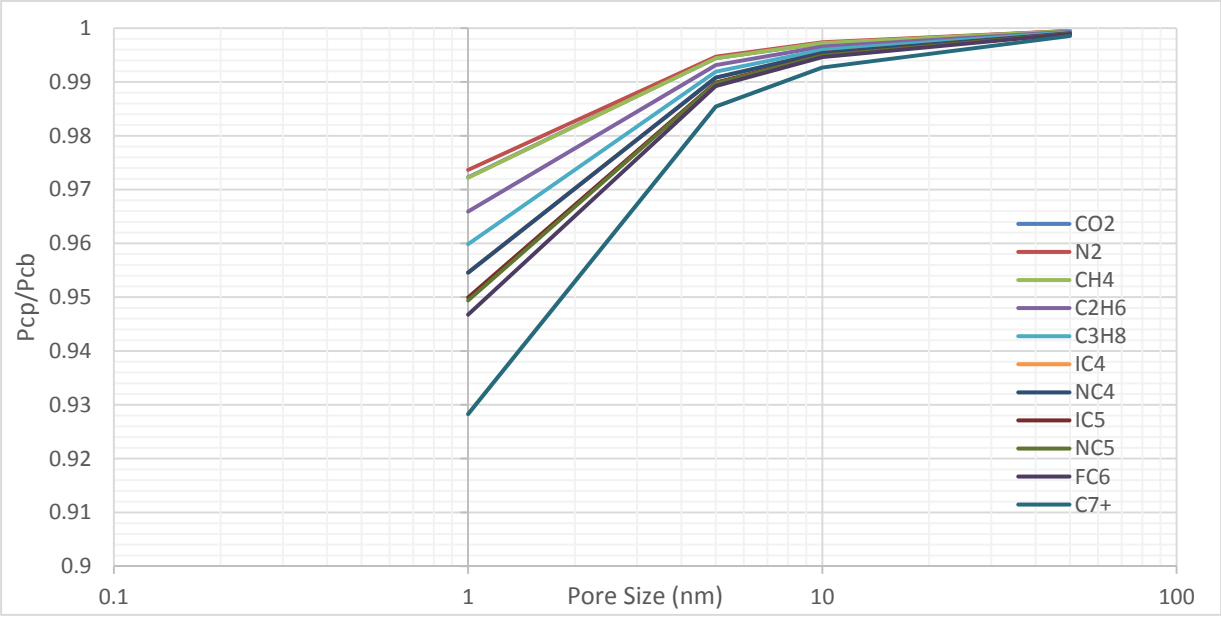

Figure 3.4: Critical pressure deviation changing with pore radius trend

Then adjusted critical temperatures and pressures are calculated at different pore sizes as 50 nm, 10 nm, 5 nm, 2.4 nm, and 1 nm for comparison. These adjusted property values are shown in Table 3.2, Table 3.3, and Table 3.4. Then these corrected critical values are substituted back to WinProp (2016) to generate the phase envelopes and fluid properties for comparison.

Table 3.2: Adjusted critical properties at r_p = 2.4 nm

		Bulk Property		r_p = 2.4 nm		
Component	Composition	P_{cb}^* (atm)	T_{cb}^* (K)	$\Delta T_c^* \& \Delta P_c^*$	P_{cp}^* (atm)	T_{cp}^* (K)
CO_2	0.0053	72.80	304.20	0.0115	71.963	300.701
N_2	0.0057	33.50	126.20	0.0109	33.134	124.821
CH_4	0.6845	45.40	190.60	0.0115	44.877	188.402
C_2H_6	0.1016	48.20	305.40	0.0142	47.518	301.077
C_3H_8	0.0505	41.90	369.80	0.0167	41.200	363.626
IC_4	0.0082	36.00	408.10	0.0189	35.319	400.383
NC_4	0.0127	37.50	425.20	0.0189	36.791	417.159
IC_5	0.0164	33.40	460.40	0.0208	32.704	450.805
NC_5	0.0138	33.30	469.60	0.0211	32.598	459.702
FC_6	0.0308	32.46	507.50	0.0222	31.740	496.240
C_{7+}	0.0705	22.38	641.58	0.0300	21.705	622.343

Table 3.3: Adjusted critical properties at r_p = 50 nm and at r_p = 10 nm

	r_p = 50 nm			r_p = 10 nm		
Component	$\Delta T_c^* \& \Delta P_c^*$	P_{cp}^* (atm)	T_{cp}^* (K)	$\Delta T_c^* \& \Delta P_c^*$	P_{cp}^* (atm)	T_{cp}^* (K)
CO_2	0.0006	72.759	304.030	0.0028	72.597	303.351
N_2	0.0005	33.482	126.133	0.0027	33.411	125.865
CH_4	0.0006	45.375	190.493	0.0028	45.273	190.067
C_2H_6	0.0007	48.167	305.190	0.0034	48.034	304.350
C_3H_8	0.0008	41.866	369.500	0.0041	41.730	368.300
IC_4	0.0009	35.967	407.724	0.0046	35.835	406.224
NC_4	0.0009	37.465	424.809	0.0046	37.328	423.245
IC_5	0.0010	33.366	459.933	0.0051	33.231	458.067
NC_5	0.0010	33.266	469.118	0.0051	33.129	467.193
FC_6	0.0011	32.425	506.952	0.0054	32.285	504.761
C_{7+}	0.0015	22.343	640.639	0.0073	22.213	636.892

Table 3.4: Adjusted critical properties at r_p = 5 nm and at r_p = 1 nm

	r_p = 5 nm			r_p = 1 nm		
Component	$\Delta T_c^* \& \Delta P_c^*$	P_{cp}^* (atm)	T_{cp}^* (K)	$\Delta T_c^* \& \Delta P_c^*$	P_{cp}^* (atm)	T_{cp}^* (K)
CO_2	0.0056	72.394	302.503	0.0277	70.781	295.765
N_2	0.0053	33.323	125.531	0.0263	32.618	122.876
CH_4	0.0056	45.146	189.534	0.0278	44.138	185.303
C_2H_6	0.0069	47.869	303.302	0.0341	46.557	294.991
C_3H_8	0.0081	41.560	366.803	0.0402	40.217	354.950
IC_4	0.0092	35.669	404.353	0.0454	34.364	389.555
NC_4	0.0092	37.156	421.296	0.0454	35.796	405.876
IC_5	0.0101	33.062	455.740	0.0500	31.729	437.360
NC_5	0.0102	32.959	464.793	0.0506	31.615	445.834
FC_6	0.0108	32.110	502.031	0.0532	30.732	480.476
C_{7+}	0.0146	22.050	632.224	0.0717	20.771	595.559

Figure 3.5 shows the phase envelope differences between the basic case, which has no confinement effect considered, and the one with the confinement considered at r_p = 2.4 nm. An envelope shrinkage is observed with the consideration of the confinement effect. The initial reservoir temperature is just a little beyond the critical temperature in both cases to demonstrate that this reservoir is a gas condensate reservoir.

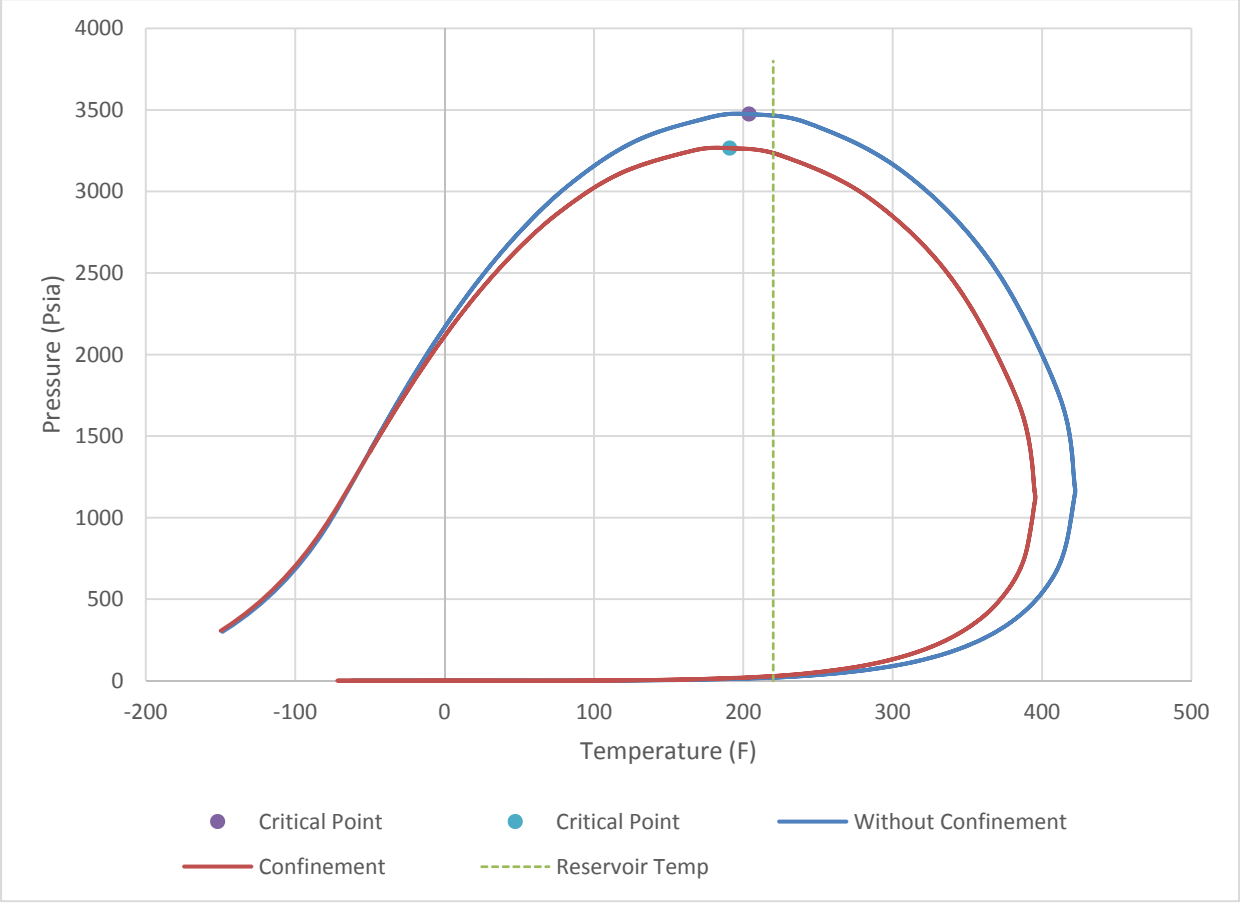

Figure 3.5: Phase envelope difference between the base case and the confinement in case one at r_p = 2.4 nm.

Figure 3.6 presents how the phase envelope changes with a pore size to demonstrate the importance of the confinement. As the pore radius decreases, the envelope becomes smaller. Therefore, based

on Darcy's law and keeping other conditions the same, the time of single phase flow will be longer, which contributes to the oil and gas production. Accordingly, a higher daily production should be expected. Consequently, without considering the confinement effect, there will result in an underestimation of oil and gas production.

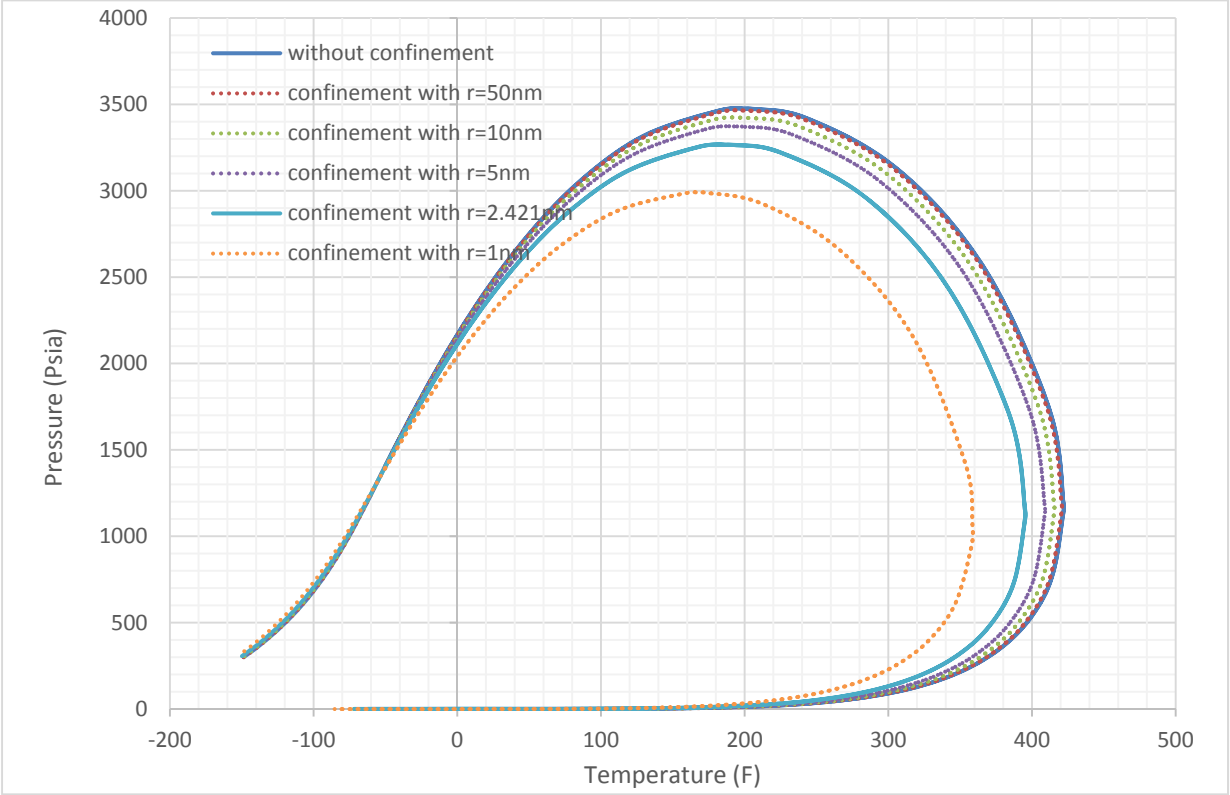

Figure 3.6: Phase envelope influence by the confinement effect at different r_p

According to the aforementioned assumptions, fluid property changes with pressure are plotted to see how the confinement affects gas production. Figure 3.7 presents that the percentage of a vapor phase volume is increased with the consideration of the confinement, which supports the expectation. Since the two-phase region becomes smaller with the confinement effect, the vapor phase volume becomes larger and the liquid phase volume becomes smaller. Also, the starting

point of the two-phase region is delayed by considering this effect. Similarly, Figure 3.8 represents that the percentage of the liquid phase volume is decreased with the confinement effect.

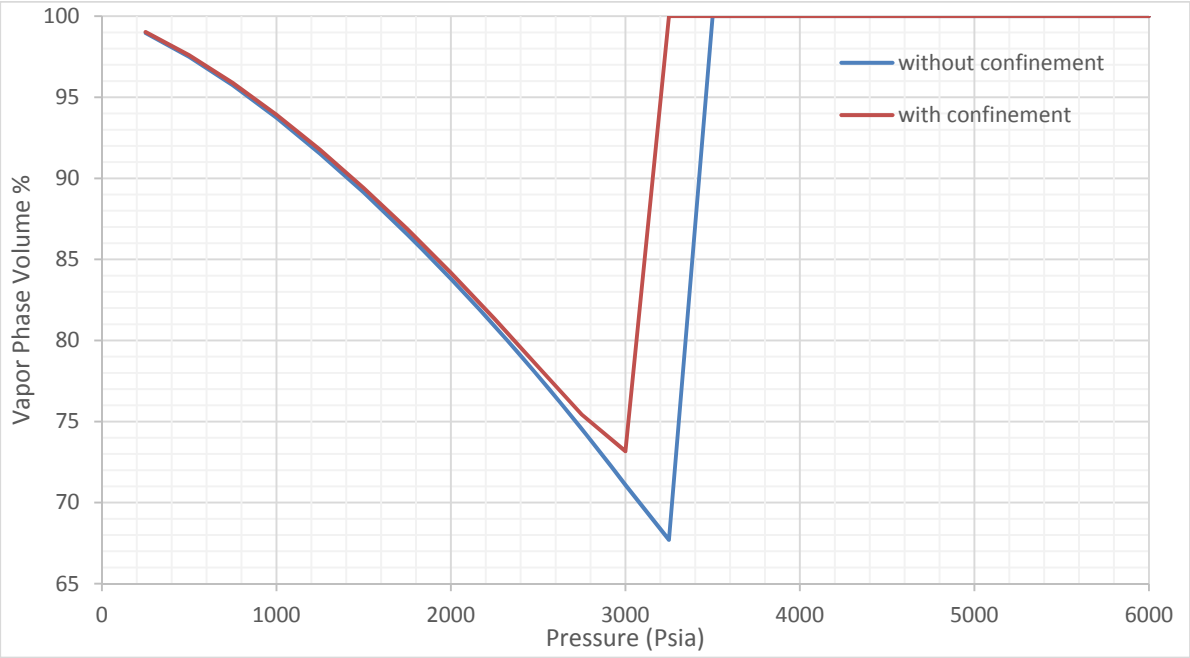

Figure 3.7: Percentage of vapor phase volume changes with the pressure at r_p = 2.4 nm

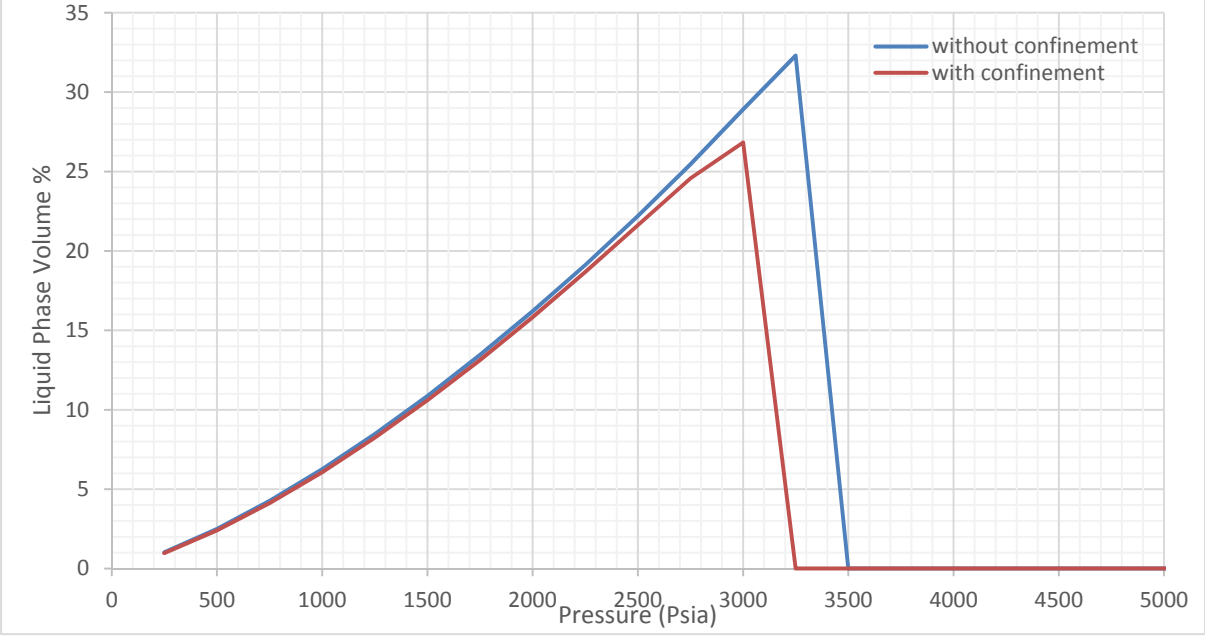

Figure 3.8: Percentage of liquid phase volume changes with the pressure at r_p = 2.4 nm

Figure 3.9 presents that the percentage of the vapor phase volume is changing with the pore size. This deviation becomes significant as the pore size decreases. Similar to the aforementioned results, the deviation starts when the pore radius is decreased to 50 nm and this deviation becomes significantly large when the pore radius is decreased to 5 nm.

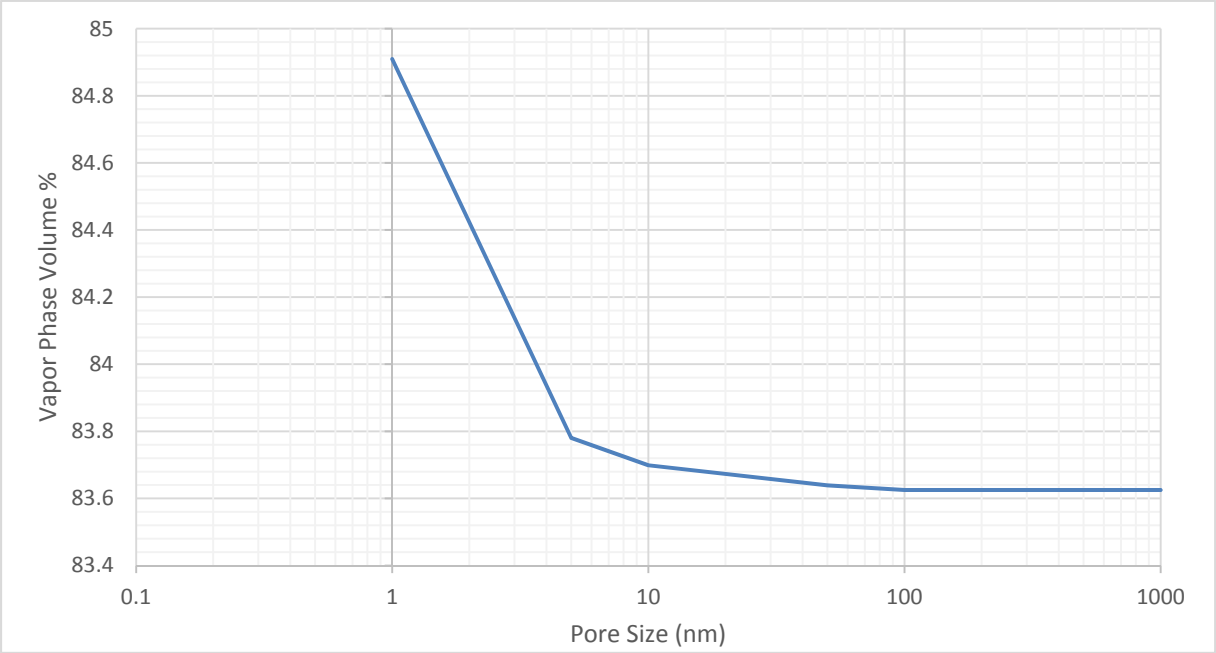

Figure 3.9: Percentage of vapor phase volume changes with pore size

The vapor viscosity changes with pressure and liquid viscosity changes with pressure plots are generated, shown in Figure 3.10 and Figure 3.11 respectively. By considering the confinement effect, the vapor viscosity becomes smaller before the pressure drops to the dew point pressure and the vapor viscosity becomes larger after the pressure depletes to the two-phase region. Such phenomenon reduces the vapor viscosity differences between the single gas phase and the liquid-gas phase. Moreover, when pressure depletes to the two-phase region, the vapor viscosity becomes larger than before and the liquid viscosity becomes smaller than before. Therefore, with a smaller vapor-liquid viscosity difference, the mobility of gas increases and will contribute to the gas flow.

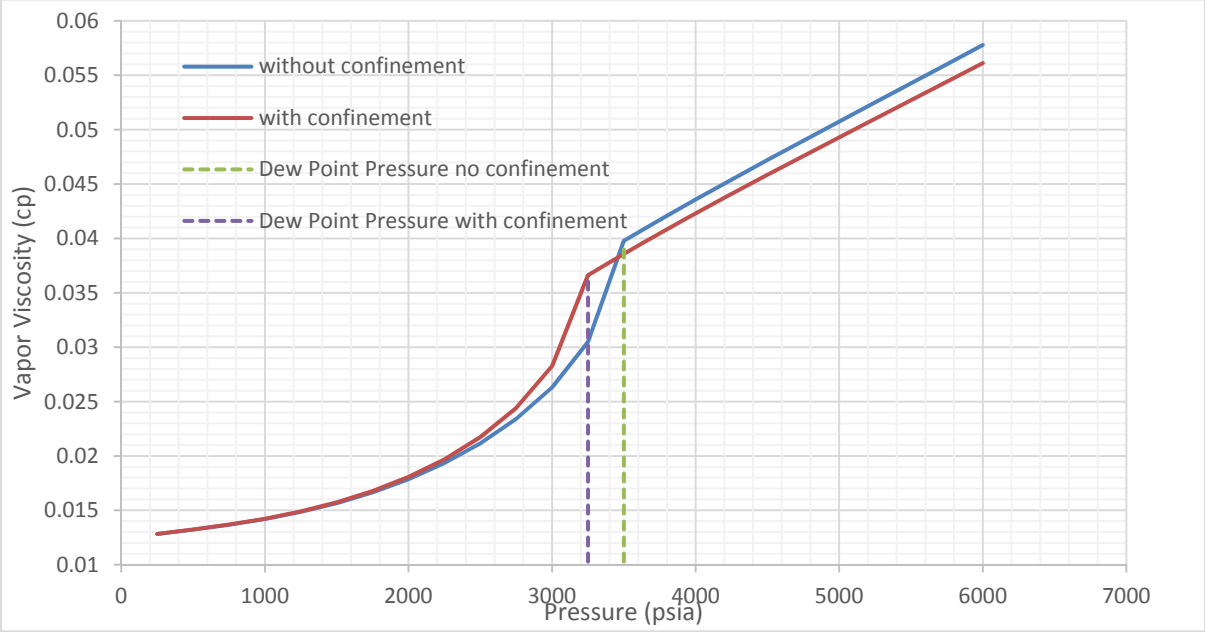

Figure 3.10: Vapor viscosity changes with pressure at r_p = 2.4 nm

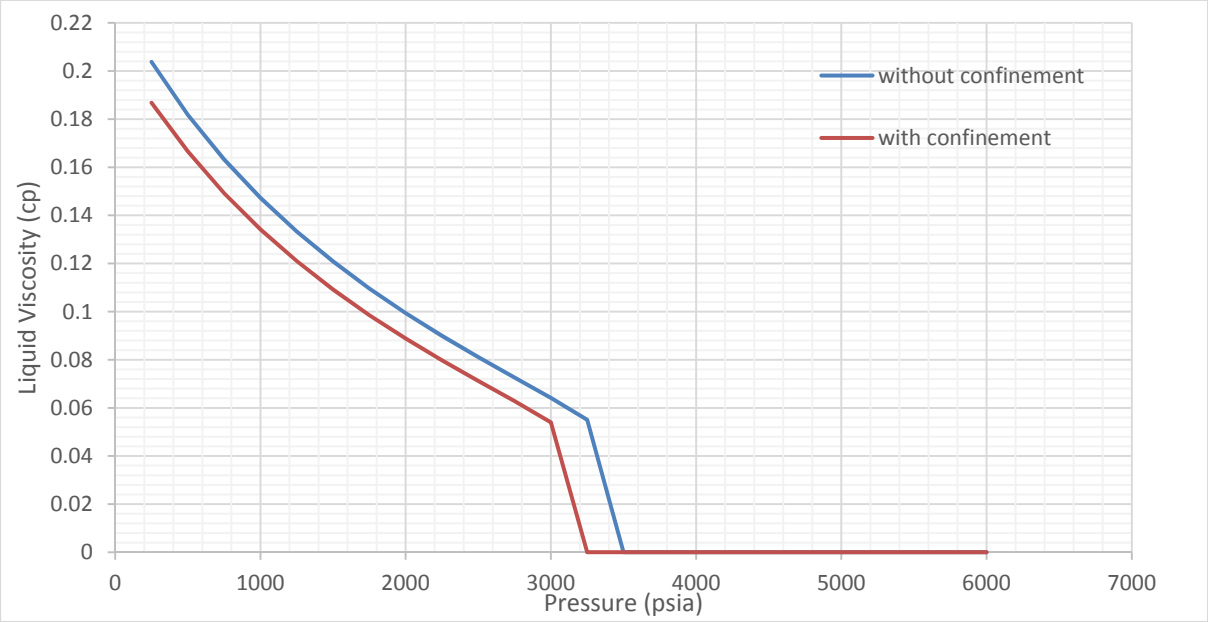

Figure 3.11: Liquid viscosity changes with pressure at r_p = 2.4 nm

However, the sorption process exists on organic surfaces in shale reservoirs and increases the original gas in place. According to that, not only does the molecule-wall interactions need to be

included, but also the adsorbed gas density affects the critical properties. In the coming scenario, a case study will be developed to take both the pore size and the adsorbed gas density correction into account and then demonstrate how this method is different than just modifying the pore size.

3.3 Confinement Effect Case Study when Considering both Pore Size and Adsorbed Phase Density Correction - Case Two

In this study, I will use the previously established model as the base model and then add property shifting parameters by considering the adsorbed gas to see how this methodology affects the phase behaviors. The equations suggested by Bilgesu (2016) are used to modify the critical temperatures and critical pressures by modifying both the adsorbed phase density and the pore size values. First, Table 3.5 presents the adsorbed phase density calculations and with an initial reservoir density of 368 kg/m^3, then $\rho_{corr} = 8.23$ is obtained.

Table 3.5: Adsorbed phase density calculations for case two

Component	Composition	b (L/mol)	a (L^2-atm/mol^2)	$x_i\rho_s$ (kg /m3)
CO_2	0.0053	0.0429	3.6108	5.4730
N_2	0.0057	0.0386	1.3505	4.1106
CH_4	0.6845	0.0431	2.2730	255.0154
C_2H_6	0.1016	0.0650	5.4968	47.0181
C_3H_8	0.0505	0.0905	9.2712	24.5993
IC_4	0.0082	0.1163	13.1415	4.0740
NC_4	0.0127	0.1163	13.6953	6.3620
IC_5	0.0164	0.1414	18.0277	8.3690
NC_5	0.0138	0.1446	18.8117	6.8835
FC_6	0.0308	0.1604	22.5392	16.5172
C_{7+}	0.0705	0.2941	52.2550	34.7591

Then, with the density correction, the equations suggested by Bilgesu (2016) are used to calculate the critical temperature shifting and critical pressure shifting at different pore radii as 50 nm, 10 nm, 5 nm, and 2.4 nm, as shown in Table 3.6 and Table 3.7. These corrected values are used to generate the phase envelope and other fluid properties for the gas mixture by using WinProp (2016).

Table 3.6: Component critical properties at r_p = 50 nm and at r_p = 10 nm

	r_p = 50 nm				r_p = 10 nm			
Component	ΔT_c^*	ΔP_c^*	P_{cp}^* (atm)	T_{cp}^* (K)	ΔT_c^*	ΔP_c^*	P_{cp}^* (atm)	T_{cp}^* (K)
CO_2	0.00007	0.005	72.465	304.179	0.00034	0.023	71.128	304.097
N_2	0.00006	0.004	33.354	126.192	0.00032	0.022	32.770	126.159
CH_4	0.00007	0.005	45.191	190.587	0.00034	0.023	44.355	190.535
C_2H_6	0.00008	0.006	47.927	305.374	0.00042	0.028	46.837	305.272
C_3H_8	0.00010	0.007	41.620	369.763	0.00049	0.033	40.502	369.618
IC_4	0.00011	0.008	35.728	408.054	0.00056	0.038	34.639	407.872
NC_4	0.00011	0.008	37.216	425.152	0.00056	0.038	36.082	424.962
IC_5	0.00012	0.008	33.121	460.343	0.00062	0.042	32.008	460.116
NC_5	0.00012	0.008	33.019	469.541	0.00062	0.042	31.896	469.307
FC_6	0.00013	0.009	32.171	507.433	0.00066	0.044	31.019	507.167
C_{7+}	0.00018	0.012	22.107	641.464	0.00089	0.060	21.032	641.008

Table 3.7: Component critical properties at r_p = 5 nm and at r_p = 2.4 nm

	r_p = 5 nm				r_p = 2.4 nm			
Component	ΔT_c^*	ΔP_c^*	P_{cp}^* (atm)	T_{cp}^* (K)	ΔT_c^*	ΔP_c^*	P_{cp}^* (atm)	T_{cp}^* (K)
CO_2	0.00068	0.046	69.459	303.994	0.001	0.095	65.911	303.775
N_2	0.00064	0.044	32.040	126.119	0.001	0.090	30.490	126.032
CH_4	0.00068	0.046	43.312	190.470	0.001	0.095	41.094	190.333
C_2H_6	0.00083	0.056	45.477	305.145	0.002	0.116	42.588	304.874
C_3H_8	0.00099	0.067	39.107	369.436	0.002	0.137	36.146	369.049
IC_4	0.00112	0.076	33.281	407.644	0.002	0.156	30.401	407.162
NC_4	0.00112	0.076	34.668	424.725	0.002	0.156	31.667	424.222
IC_5	0.00123	0.083	30.619	459.833	0.003	0.171	27.675	459.234
NC_5	0.00124	0.084	30.496	469.016	0.003	0.173	27.527	468.397
FC_6	0.00131	0.089	29.583	506.835	0.003	0.182	26.536	506.131
C_{7+}	0.00177	0.120	19.693	640.441	0.004	0.247	16.858	639.239

Figure 3.12 presents the critical temperature deviation at different pore radii by adding ρ_{corr} and Figure 3.13 shows the critical pressure deviation at different pore radii by adding ρ_{corr}. Similarly, as pore sizes get smaller, the deviation becomes larger. However, by adding the correction of the adsorbed phase density, the critical temperature deviation becomes smaller and the critical pressure deviation becomes larger compared to the case one, which supports the prediction based on these equations. Since $\Delta T_c^* \propto \frac{1}{\rho_{corr}}$, by adding ρ_{corr}, ΔT_c^* will be smaller than before in order to result in a higher T_{cp}^*. Therefore, the difference between T_{cp}^* and T_{cb}^* becomes smaller to result in a decreased deviation. Similarly, $\Delta P_c^* \propto \rho_{corr}$, by adding ρ_{corr}, ΔP_c^* will be larger than before to

result in a smaller P_{cp}^{*} . Consequently, the difference between P_{cp}^{*} and P_{cb}^{*} becomes larger to result in an increased deviation.

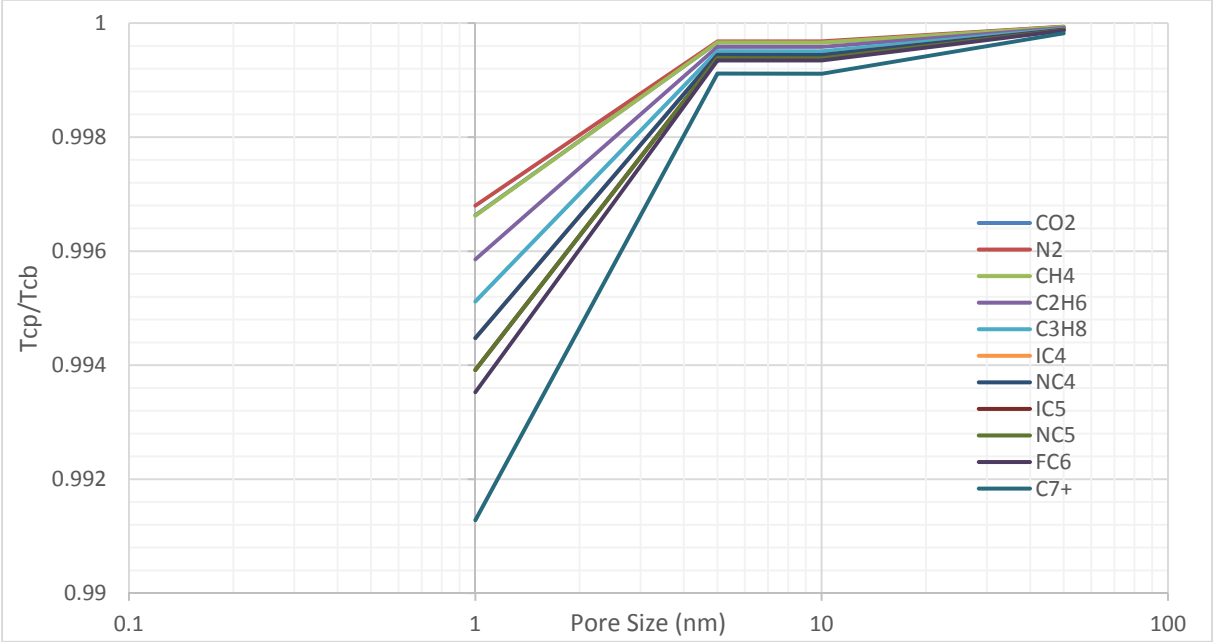

Figure 3.12: Critical temperature deviation changes with pore radius in case two

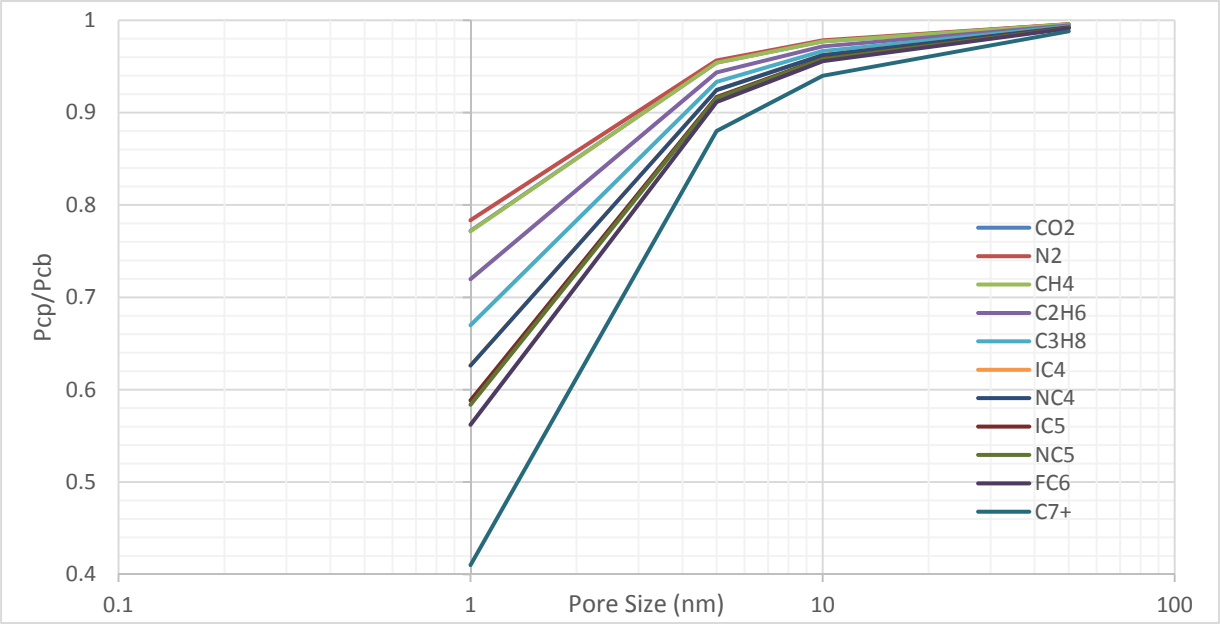

Figure 3.13: Critical pressure deviation changes with pore radius in case two

Figure 3.14 presents the difference of the phase envelope between the base case, which has no confinement effect considered, and case two at r_p = 2.4 nm. An envelope shrinkage is observed with the consideration of the confinement effect, which is the same compared to case one. Figure 3.15 shows how the phase envelope changes with a pore size in case two to demonstrate the profound influence of the confinement effect.

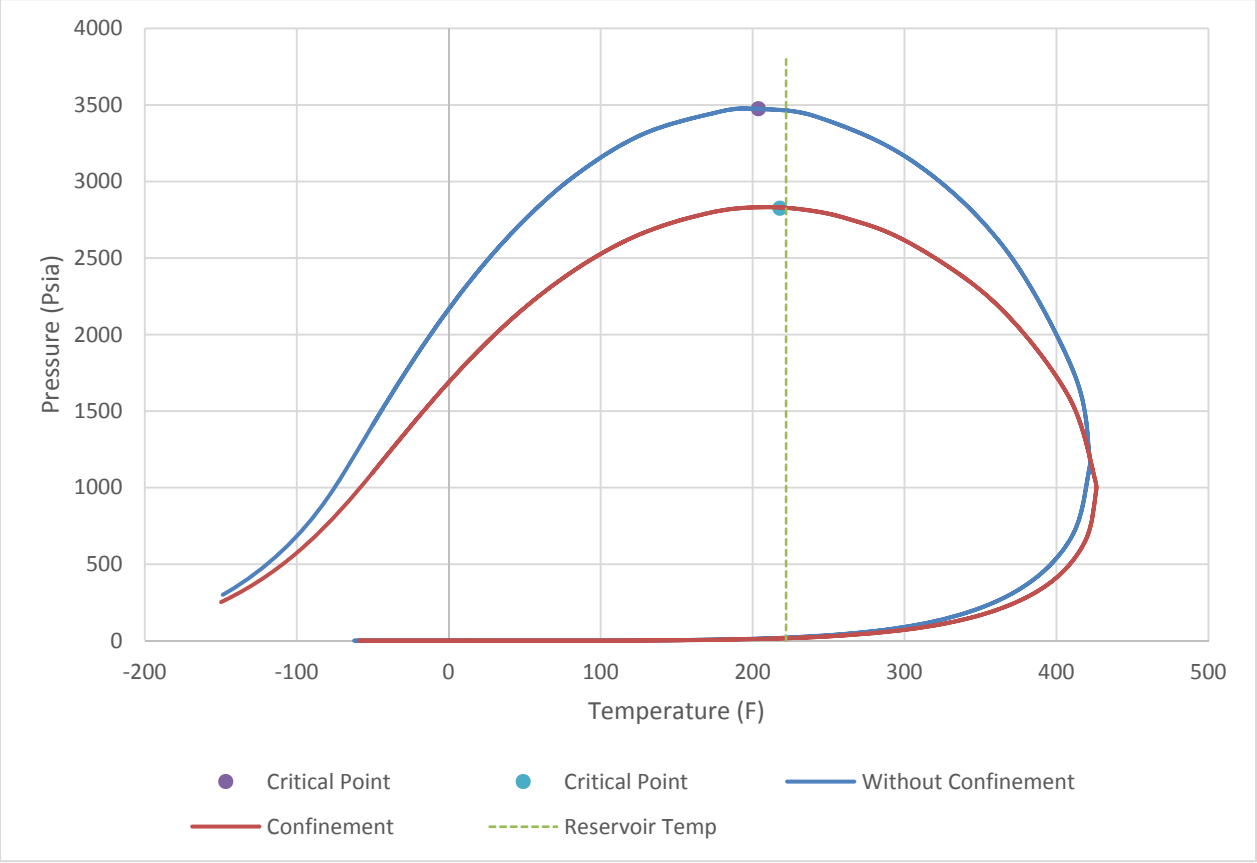

Figure 3.14: Difference of phase envelope between the base case and case two at r_p = 2.4 nm.

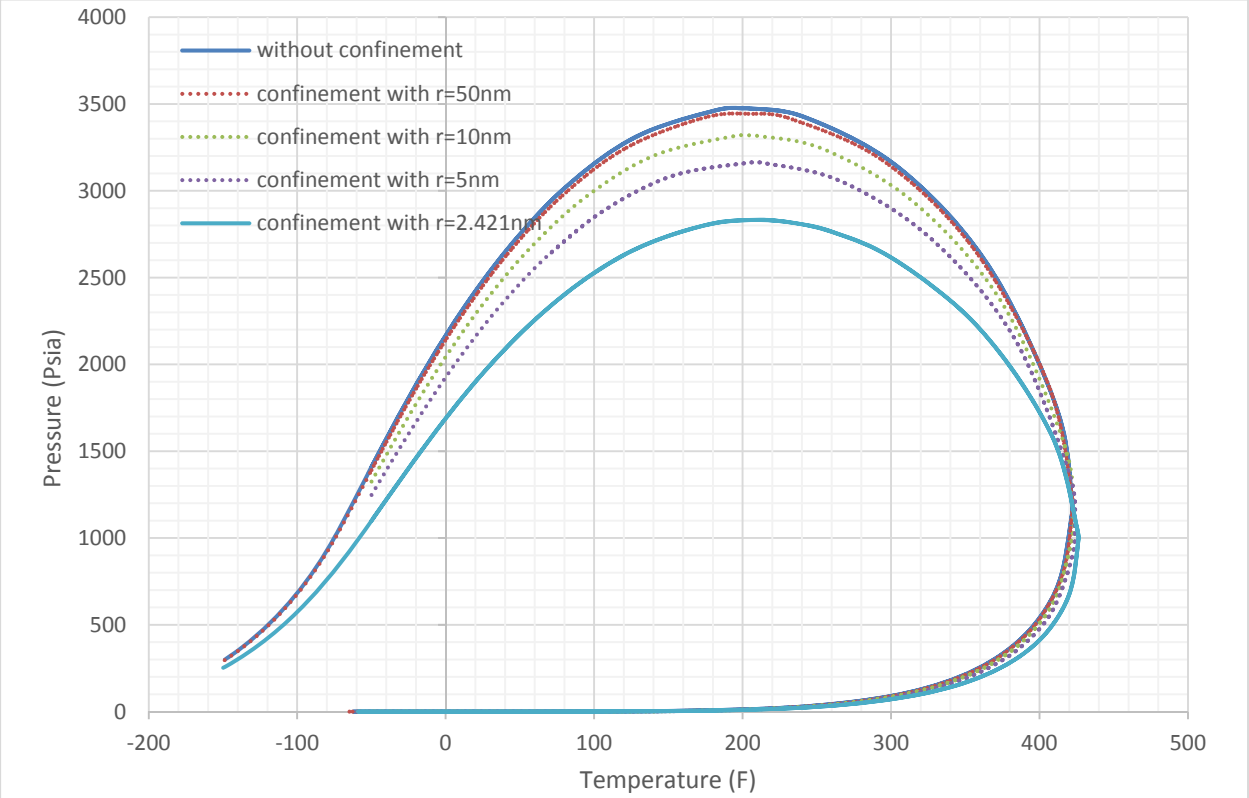

Figure 3.15: Phase envelope influence when considering the confinement effect in case two at different r_p

In the aforementioned two scenarios, the confinement effect is discussed by applying two different methods, including case one where only a pore size is considered and case two that considers both the pore size and adsorbed gas density. Subsequently, a comparison of these two methodologies is developed to see the difference between these two models.

3.4 Comparison

Figure 3.16 presents the difference of the phase envelope among the base case, case one with the consideration of the pore size, and case two considering the changes of both the pore size and

adsorbed gas density. It is a good indicative of that there are differences when the method is changed from Zarragoicoechea and Kuz (2004) to Bilgesu (2013).

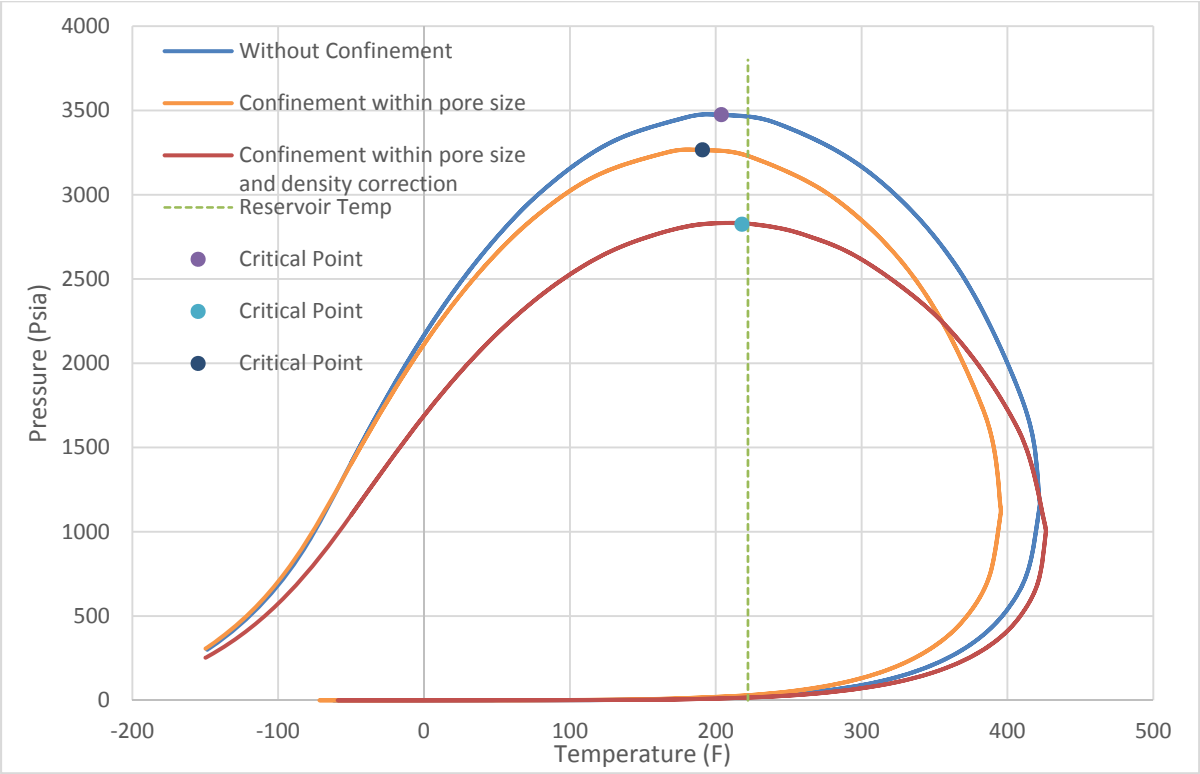

Figure 3.16: Phase envelope influence by different confinement methods at $r_p = 2.4\ nm$

Then fluid property plots are generated based on three different methods. Figure 3.17 presents how the percentage of the vapor phase volume changes with pressure in three different cases. From this figure, the minimum percentage of the vapor phase volume is increased by only correcting the pore size and that minimum value is decreased by correcting both the pore size and adsorbed gas density, which is corresponding to the phase envelope diagram. Since adsorbed gas is taken into account, parts of the gas volume were treated as free gas and now they are treated as adsorbed gas. Therefore, a reduction in the vapor phase volume occurs in the reservoir. Also, the critical point

shifts left with the confinement is considered, which means that the single gas phase flow time will be longer and higher oil and gas production can be expected.

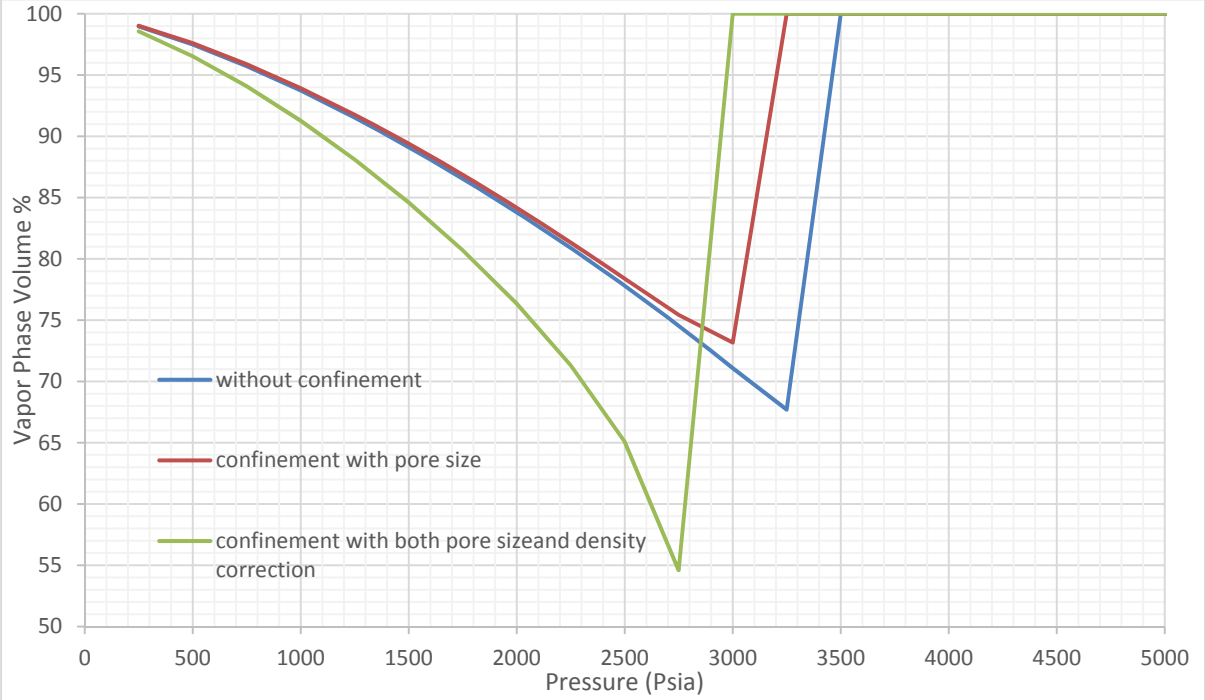

Figure 3.17: Percentage of vapor phase volume changes with pressure in three different cases at r_p = 2.4 nm

Similarly, Figure 3.18 shows how the percentage of the liquid phase volume changes with pressure in three different cases. In this graph, the maximum percentage of the liquid phase volume is decreased by only correcting the pore size and this maximum value is increased by correcting both the pore size and adsorbed gas density, which yields the same trend compared to Figure 3.17. Since the sorption process has been included, parts of the gas volume were regarded as free gas and now they are treated as adsorbed gas, which is an additional liquid phase. Therefore, an increment in

the liquid phase volume occurs in the reservoir. Similar to Figure 3.17, the critical points shifted left with confinement considered and higher oil and gas production can be expected.

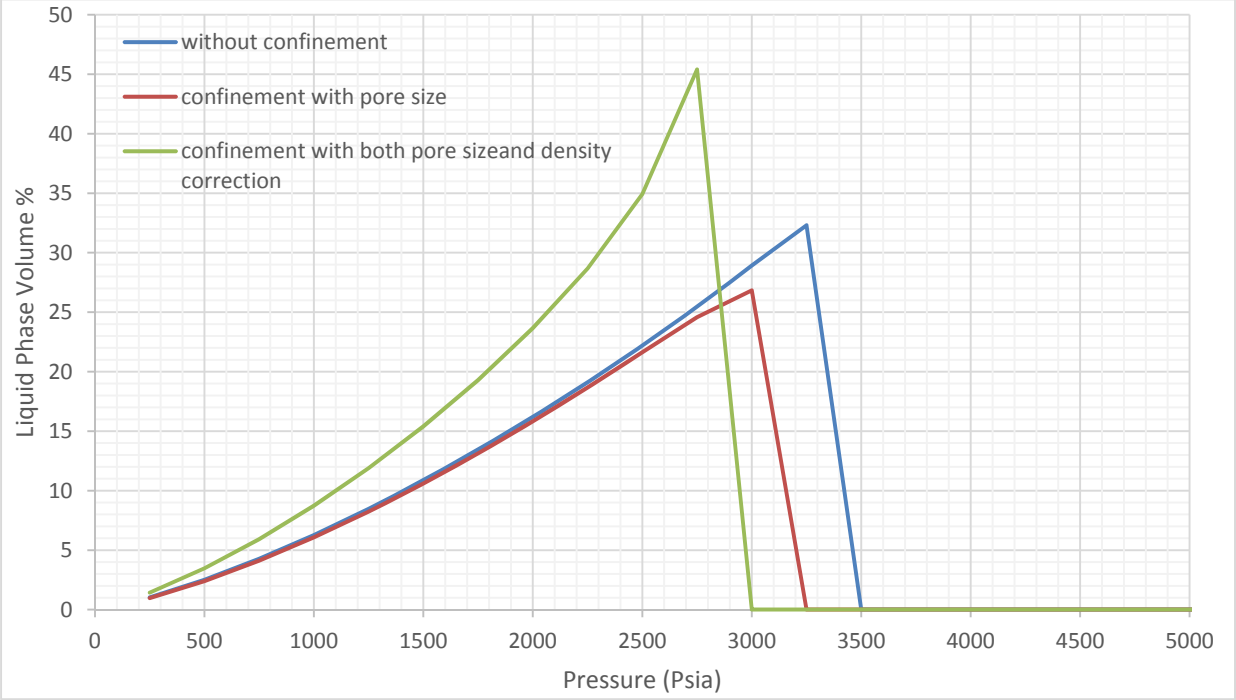

Figure 3.18: Percentage of liquid phase volume changes with pressure in three different cases at r_p = 2.4 nm

Moreover, Figure 3.19 and Figure 3.20 are plotted to describe how the vapor viscosity and the liquid viscosity are affected as pressure drops in three different models. From Figure 3.19, as pressure declines, the vapor viscosity yields a declined trend in all the methods. In addition, by taking the adsorption into account, this declination becomes extremely significant. From Figure 3.20, as pressure declines to the two-phase region, the liquid viscosity yields an incremental trend in all the methods. Additionally, if the confinement effect is considered, there exists a reduction in the liquid viscosity compared to the base case. This reduction becomes extremely significant if the

adsorption phase density has been taken into account. The adsorbed phase has a lower viscosity compared to the liquid phase.

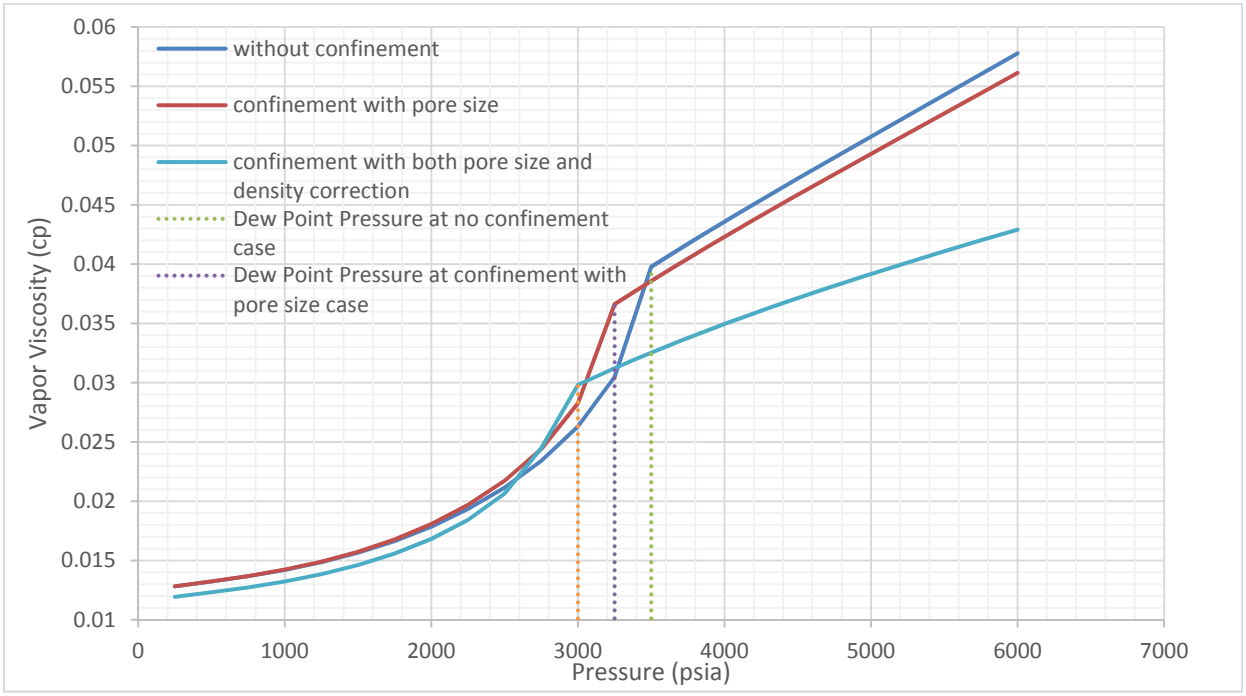

Figure 3.19: Vapor viscosity changes with pressure in three different cases at r_p = 2.4 nm

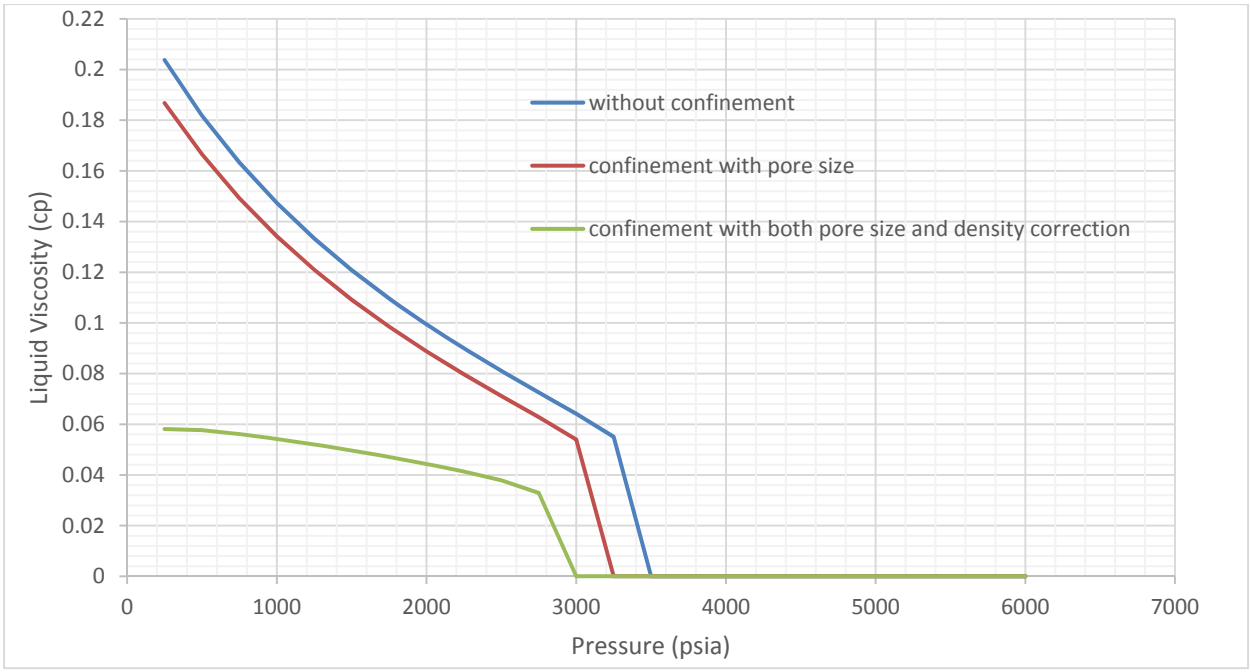

Figure 3.20: Liquid viscosity changes with pressure in three different cases at r_p = 2.4 nm

A conclusion can be reached that with the consideration of both the pore size and adsorbed phase density correction, the reservoir has a longer single gas flow time and smaller gas and liquid viscosity compared to the case one. According to that, an increment in oil and gas production can be predicted by applying Bilgesu's (2013) equations. Results of the daily production performance by three different methodologies will be discussed later in Chapter 5. Before I move to the next chapter, a Monte Carlo simulation is carried out to assess the impact of each variable on the output to deepen the understanding of these methodologies.

3.5 Monte Carlo Simulation and Sensitivity Analysis

Based on the Zarragoicoechea and Kuz (2004) correlations, a pore radius could affect the shifting of critical properties due to a confinement effect. Based on the extended Bilgesu (2016) equations, the corrected adsorbed phase density could also affect the shifting of critical properties. In order to use these new correlations to correct the critical properties, the impact of each variable on the output needs to be assessed. In this approach, I only focus on the trend of the critical property shifting. The One Variable at the Time (OVAT) technique is sufficient to reduce the run time, which is only one variable changes at the time while other variables keep constant. The interactions between the random variables are ignored.

3.5.1 CH_4 Monte Carlo Simulation

Since the highest composition is attributed to CH_4 in shale gas reservoirs, a Monte Carlo simulation is carried out on the component of CH_4 to represent the trend of the light components. In this approach, variables such as the pore size, the adsorbed phase density correction, and the combination of the pore size and adsorbed phase density correction are included in the CH_4 Monte

Carlo simulation. The Duvernay formation has an average porosity of 0.065, an average permeability of 0.000394 milli Darcy, and an average TOC of 0.045 (Dunn, 2012). By applying a pore radius 35 correlation, the average pore size is calculated to around 4 nm in this reservoir. In this simulation, the pore size varies from 1 nm to 10 nm, and the adsorbed phase density correction varies from 4.266 to 15.133. Table 3.8 shows the deviation of critical temperature by changing variables including the pore size, the density correction, and the combination of pore size and density correction. Similarly, Table 3.9 shows the deviation of critical pressure by changing variables such as the pore size, the density correction, and the combination of the pore size and density correction.

Table 3.8: Deviation of CH_4 critical temperature

	T_{cp} (K)			$T_{cp} - T^0{}_{cp}$ (K)	
	Original	Lower	Upper	- Deviation	+ Deviation
Pore Size (1 nm ,10 nm)	190.333	189.957	190.535	-0.3765	0.2022
ρ_{corr} (4.266, 15.153)	190.333	190.085	190.455	-0.2482	0.1219
Pore Size*ρ_{corr}	190.333	189.358	190.565	-0.9748	0.2318

Table 3.9: Deviation of CH_4 critical pressure

	P_{cp} (atm)			$P_{cp} - P^0{}_{cp}$ (atm)	
	Original	Lower	Upper	- Deviation	+ Deviation
Pore Size (1 nm , 10 nm)	41.091	35.014	44.354	-6.0772	3.2635
ρ_{corr} (4.266 ,15.153)	41.091	37.468	43.167	-3.6223	2.0762
Pore Size*ρ_{corr}	41.091	26.283	44.858	-14.8078	3.7673

By using the above tables, Tornado charts are generated to quantify the impact of each variable on the critical shifting. Figure 3.21 shows how critical temperature deviates from the original value if only a variable changes at the time and Figure 3.22 shows how critical pressure deviates from the original value if only a variable changes at the time. From both plots, the deviation forms by the pore size are observed to be larger than the deviation forms by the density correction. This result can extend to that the pore size effects are more than those from the correction of the adsorbed phase density in the confinement system. The combination effects of the pore size and density correction on the critical properties are significant and even can change the critical properties by 30%. So we need to have sufficient knowledge in obtaining the parameters of the pore size and corrected adsorbed phase density.

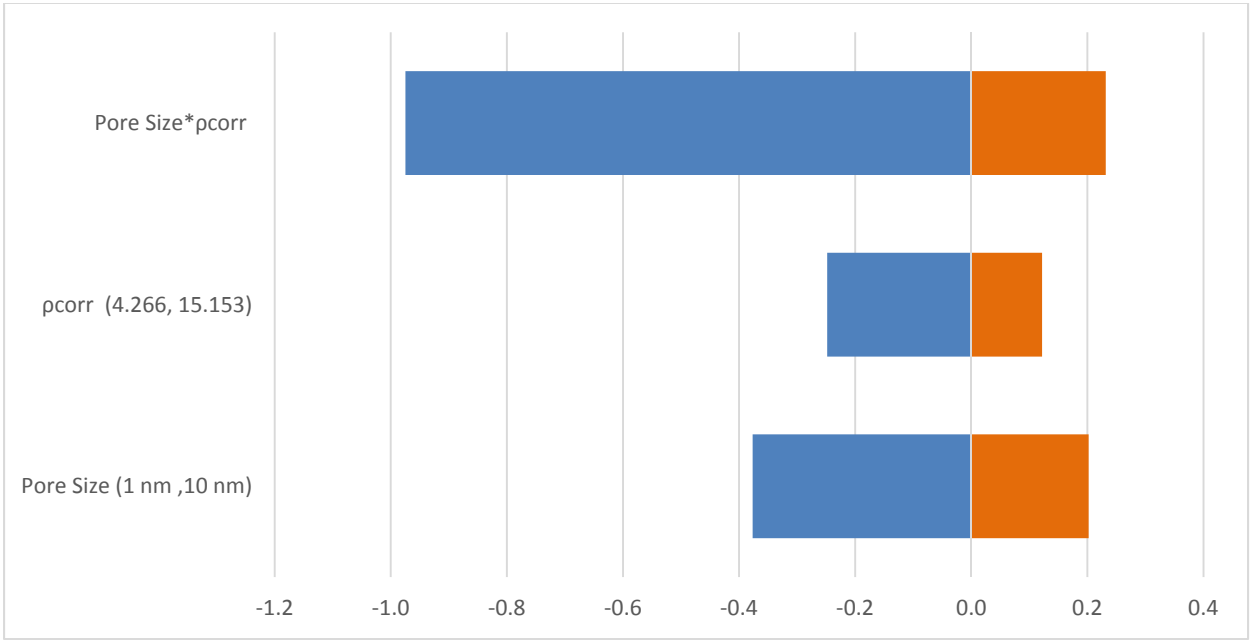

Figure 3.21: Tornado chart on the deviation of CH_4 critical temperature

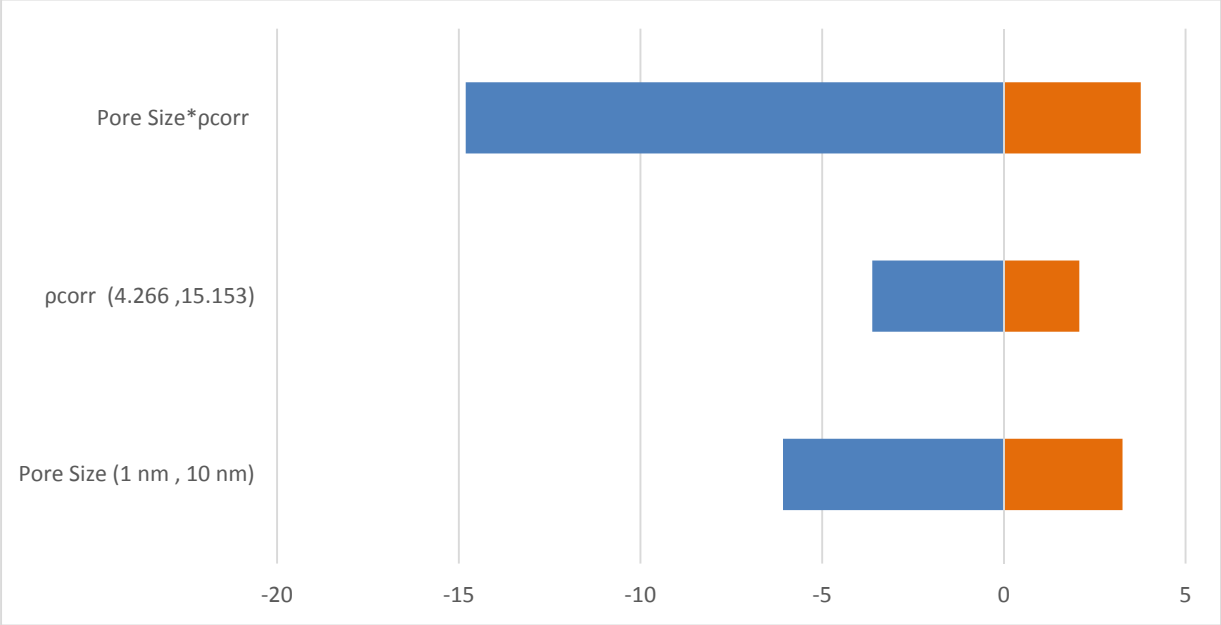

Figure 3.22: Tornado chart on the deviation of CH_4 critical pressure

3.5.2 C_{7+} Monte Carlo Simulation

Moreover, C_{7+} is a lumped component, which means that the bulk critical temperature and bulk critical pressure of C_{7+} may not be accurate. Therefore, a Monte Carlo simulation is carried out on the component of C_{7+} including variables of the pore size, adsorbed phase density correction, C_{7+} bulk critical temperature, and C_{7+} bulk critical pressure. Similar to the CH_4 Monte Carlo case, the pore size varies from 1 nm to 10 nm, and the adsorbed phase density correction varies from 4.266 to 15.133. Pure FC_7 has a bulk critical temperature of 543 K and bulk critical pressure of 31 atm. The pure FC_{20} has a bulk critical temperature of 783 K and bulk critical pressure of 14.5 atm. These values help us to estimate the critical temperature of the lumped component C_{7+} that varies from 620 K to 680 K and critical pressure of the lumped component C_{7+} that varies from 15 atm to 30 atm. Table 3.10 shows the deviation of critical temperature by changing variables including the pore size, adsorbed phase density correction, and bulk critical temperature of C_{7+}. Similarly,

Table 3.11 shows the deviation of critical pressure by changing variables such as the pore size, adsorbed phase density correction, and bulk critical pressure of C_{7+}.

Table 3.10: Deviation of C_{7+} critical temperature

	T_{cp} (K)			$T_{cp} - T^0{}_{cp}$ (K)	
	Original	Lower	Upper	- Deviation	+ Deviation
Pore Size (1 nm, 10 nm)	639.241	635.988	641.009	-3.2538	1.7673
ρ_{corr} (4.266, 15.153)	639.241	637.069	640.308	-2.1724	1.0671
C_{7+} Tcb (620 K, 680 K)	639.241	617.742	677.523	-21.4993	38.2822

Table 3.11: Deviation of C_{7+} critical pressure

	P_{cp} (atm)			$P_{cp} - P^0{}_{cp}$ (atm)	
	Original	Lower	Upper	- Deviation	+ Deviation
Pore Size (1 nm, 10 nm)	16.854	9.164	21.031	-7.6898	4.1768
ρ_{corr} (4.266, 15.153)	16.854	12.212	19.515	-4.6418	2.6605
C_{7+} Pcb (15 atm , 30 atm)	16.854	11.298	22.596	-5.5558	5.7423

By using the above tables, Tornado charts are generated to quantify the impact of each variable on the critical shifting. Figure 3.23 shows how critical temperature deviates from the original value if only one variable changes at the time and Figure 3.24 shows how critical pressure deviates from the original value if only one variable changes at the time. From Figure 3.23, the deviation forms by the bulk critical temperature of C_{7+} are observed to be larger than the deviation forms by the pore size and adsorbed phase density correction. From Figure 3.24, the deviation forms by the bulk critical pressure, adsorbed phase density correction, and the pore size are almost the same. For the

lumped component, this phenomenon indicates that accurately estimating the bulk critical temperature of the lumped component is the most important thing in the confinement system compared to other random variables.

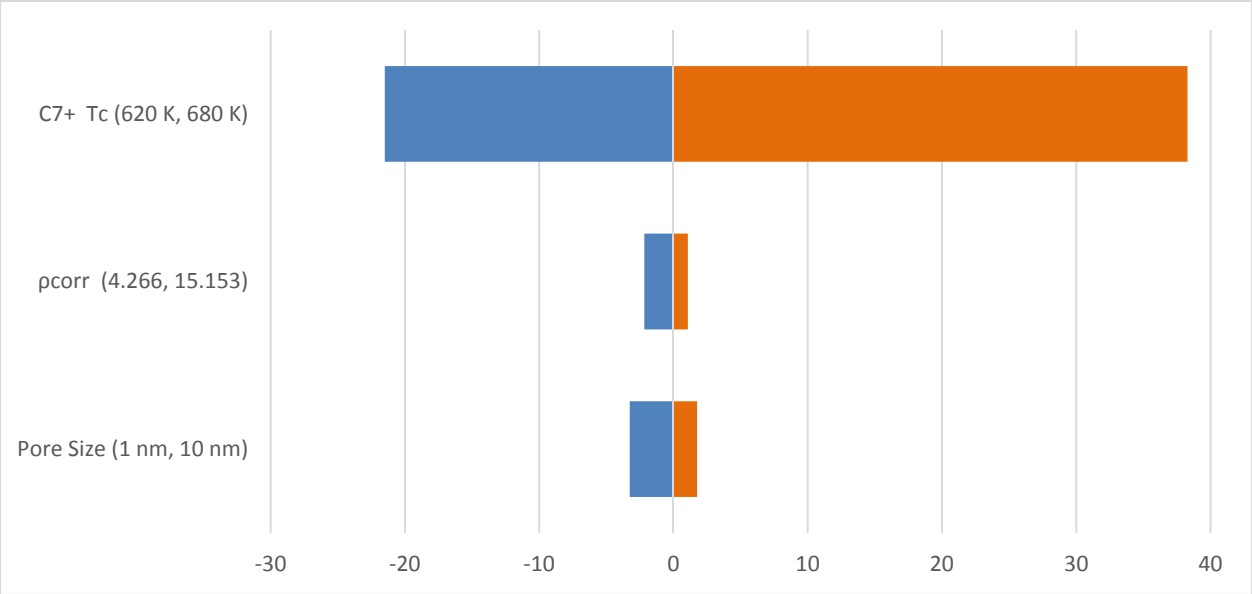

Figure 3.23: Tornado chart on the deviation of C_{7+} critical temperature

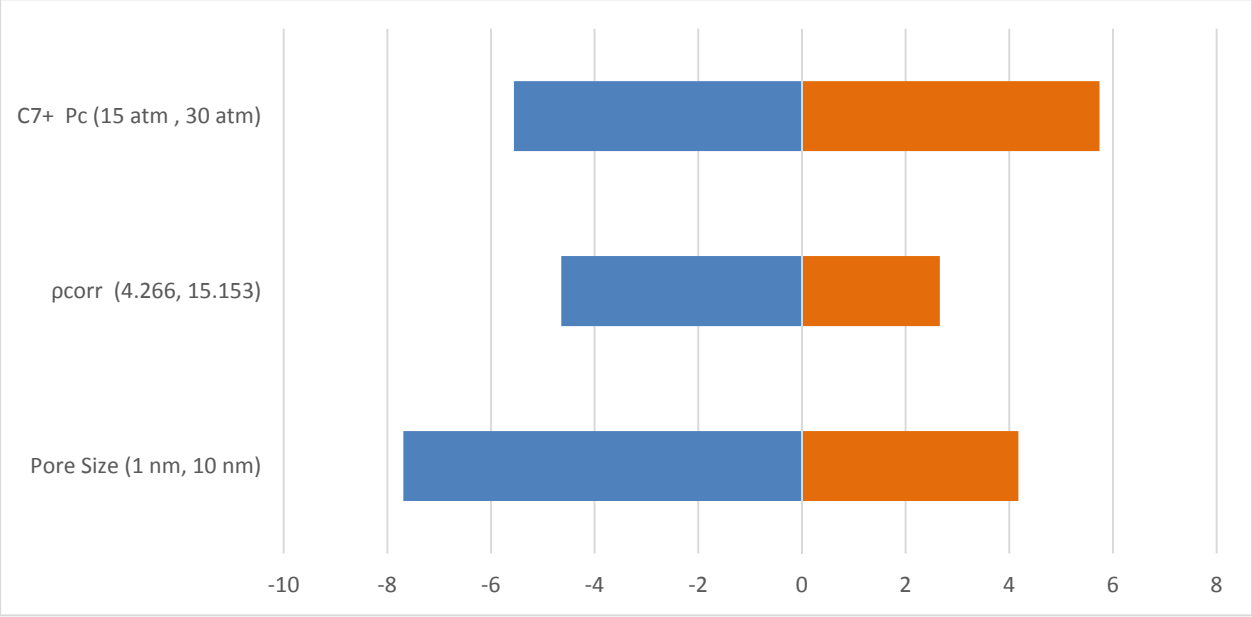

Figure 3.24: Tornado chart on the deviation of C_{7+} critical pressure

Chapter Four: **Adsorption Effect on Shale Gas Condensate Phase Behavior**

4.1 Vapor and Liquid Phase Adsorption Theory

4.1.1 IAST on Two-Phase Adsorption Modelling

As presented in Chapter 2, when pressure depletes under the dew point pressure, liquid will exist in the bulk. In order to be thermodynamically-consistent, adsorption from liquid needs to be considered as well. In 1965, Myers and Prausnitz first developed a thermodynamically-consistent multi-component adsorption model to calculate the total amount of adsorption from the gas-liquid mixture. Now, the relationship between the adsorption from vapors and the adsorption from liquids needs to be derived.

Rajput (2016) suggested an assumption that only considers a binary-component mixture, component 1 and component 2, in the bulk that contacted with solid adsorbent. At the beginning the system is under-saturated, and there exist a vapor phase and an adsorbed phase in equilibrium. Under these conditions, Gibbs' equation can be written as (Myers and Sircar, 1972):

$$n_1'(d\mu_1') + n_2'(d\mu_2') + n_a'(d\mu_a') = V'dP \tag{4.1}$$

By the assumptions of thermodynamic equilibrium and therefore the $V'dP$ term is neglected, an equation (Rajput, 2016) ends up with:

$$-\frac{n_a(d\mu_a)}{RT} = n_1' dln(Py_1) + n_2' dln(Py_2) \tag{4.2}$$

There still presents that three portions need to be described in the above adsorption and desorption equation (4.2), which are the vapor adsorption of component 2, adsorbent is immersed in a liquid

mixture of components 1 and 2, and the vapor desorption of component 1, respectively. Figure 4.1 presents this integration path.

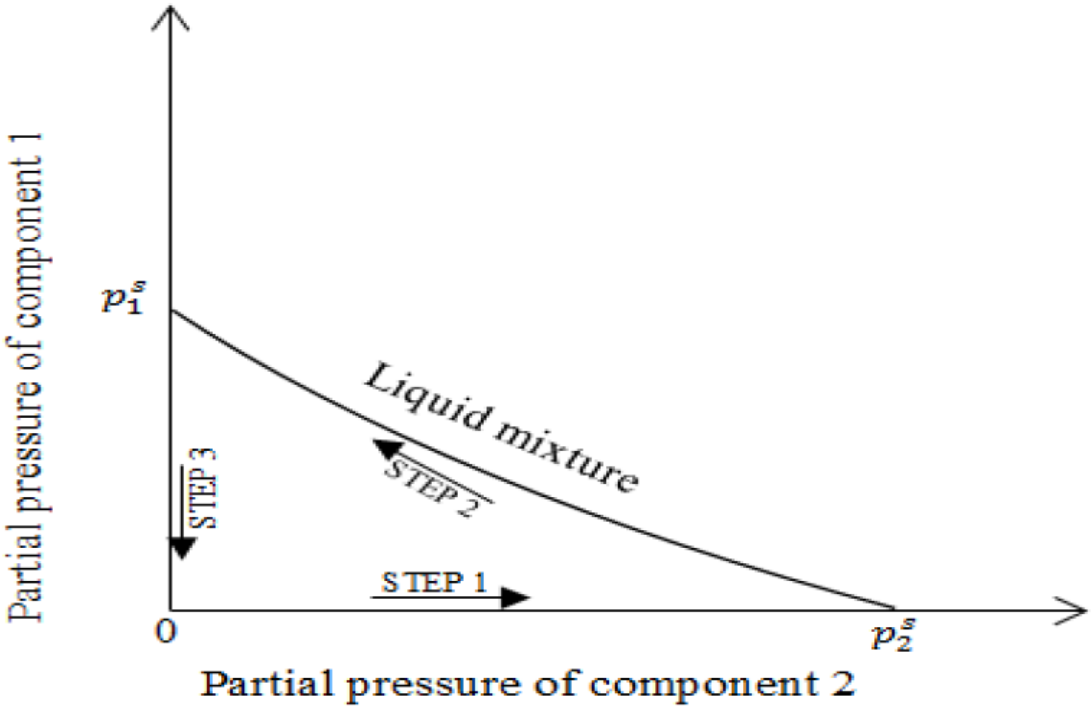

Figure 4.1: Integration path used for the derivation of thermodynamic consistency check (Rajput, 2016)

Finally, this adsorption integration equation (4.2) ends up with the following equation (4.3) (Rajput, 2016) by considering the thermodynamic consistency. The first integral represents the vapor adsorption of component 2, the second integral represents the vapor adsorption of component 1, and the last integral represents the adsorption from the liquid mixture of components 1 and 2.

$$\int_{P=0}^{P_2^S} \frac{n_2'}{p} dP - \int_{P=0}^{P_1^S} \frac{n_1'}{p} dP + \int_{x_1=0}^{1} \frac{n_1^e}{\gamma_1 x_1 x_2} d(\gamma_1 x_1) = 0 \quad (4.3)$$

4.1.2 Surface Excess

Now, an unknown variable n_i^e is still unexplained in the equation. In order to understand the liquid adsorption behavior, Sircar and Myers (1970) introduced a term called surface excess to represent the experimental amount of the adsorbed liquid at a liquid-solid interface. Then Rogue-Malherbe (2007) suggested an equation to describe the surface excess of the liquid phase as follows:

$$n_i^e = n_i{}^*(x_i^* - x_i) \tag{4.4}$$

where

n_i^e= Surface excess of liquid phase of component i in lbmol/kg

$n_i{}^*$= Moles of liquid mixture brought into contact with unit mass of adsorbent of component i

x_i^*= Fraction of component i in the liquid phase before contact with adsorbent

x_i= Fraction of component i in the liquid phase after contact with adsorbent

Similarly, the surface excess of the vapor phase is defined as:

$$n_i^{ev} = n_i{}^* - x_i^*(\sum n_i{}^*) \tag{4.5}$$

where

n_i^{ev}= Surface excess of vapor phase of component i in lbmol/kg

$n_i{}^*$= Moles of liquid mixture brought into contact with unit mass of adsorbent of component i

$\sum n_i{}^*$= Total moles adsorbed

x_i^*= Fraction of component i in the liquid phase

As pressure is approaching to the saturation pressure, the surface excess of the liquid phase equals that of the vapor phase (Sircar and Myers, 1970), presenting an equation:

$$n_i^e = \lim_{P \to P^S} (n_i^{ev}) \tag{4.6}$$

Based on the aforementioned assumptions, if the reservoir is initially at a single liquid phase, a calculation at the bubble point pressure should be carried out and presents its equivalent vapor and liquid compositions. Oppositely, if the reservoir is initially at a single vapor phase, a calculation at the dew point pressure should be carried out and presents its equivalent liquid and vapor compositions. Accordingly, the total amount of adsorption can be calculated based on the IAST and finally the equivalent gas composition after contacting with adsorbent within the consideration of a phase change can be estimated.

4.2 Adsorption Calculation

In this study, three different methodologies are imposed to test the aforementioned phenomenon, which are the ML method, the EL method, and the IAST-EL method. Later on, Monte Carlo simulations of important adsorption variables will be established to find out which parameter is more sensitive.

4.2.1 Monolayer Langmuir Model

A Duvernay gas condensate reservoir with the initial pressure of 4500 psia and the initial temperature of 220 ºF is used and such a system is initially at the single gas phase condition. These conditions will hold the same for all the following calculations.

In the reservoir, around 68% of the reservoir gases are attributed to CH_4. Therefore, CH_4 is chosen to represent all the adsorbed gas in the Monolayer Langmuir model. Then the Langmuir volume and Langmuir pressure of CH_4 are inputted into the simulator. Based on the information from Accumap, Table 4.1 presents the composition and the experimental Langmuir data of CH_4 which are used in this approach.

Table 4.1: Gas composition and experimental data for ML model

					Input number into GEM	
Component	composition	MW	V_{Li} (SCF/ton)	P_{Li} (psia)	V_{Li} ((gmol/lb)	$\frac{1}{P_{Li}}$ (1/psia)
CH_4	0.6845	16.043	60	1100	0.0359	0.0009

4.2.2 Extended Langmuir Model

Similarly, by considering the multi-components existing in the adsorbed gas, the EL model is established by adding Langmuir consideration of other components. Then all these Langmuir volumes and Langmuir pressures are inputted into the simulator, which are from Accumap. Table 4.2 presents the fluid system composition and the experimental Langmuir data of each component for this approach.

Table 4.2: Gas compositions and experimental data for EL model

					Input number into GEM	
Component	composition	MW	V_{Li} (SCF/ton)	P_{Li} (psia)	V_{Li} ((gmol/lb)	$\frac{1}{P_{Li}}$ (1/psia)
CO_2	0.0053	44.010	150	455	0.0897	0.0022
N_2	0.0057	28.013	30	1400	0.0179	0.0007
CH_4	0.6845	16.043	60	1100	0.0359	0.0009
C_2H_6	0.1016	30.070	90	811	0.0538	0.0012
C_3H_8	0.0505	44.097	180	800	0.1076	0.0013
IC_4	0.0082	58.124	190	500	0.1136	0.0020
NC_4	0.0127	58.124	200	480	0.1195	0.0021
IC_5	0.0164	72.151	220	350	0.1315	0.0029
NC_5	0.0138	72.151	240	320	0.1434	0.0031
FC_6	0.0308	86.000	270	300	0.1614	0.0033
C_{7+}	0.0705	145.000	300	250	0.1793	0.0040

4.2.3 Ideal Adsorbed Solution Theory Calculation

However, thermodynamics is inconsistent in both the ML model and the El model, since the Langmuir models have not taken a phase change into consideration. When pressure drops below the dew point pressure, the single gas phase system will become the gas-liquid phase system.

Therefore, IAST calculations will be carried out to take the phase change into account in this study (Myers et. al, 1965).

First, IAST calculations need the compositions at the saturation pressure, which is the dew point pressure in this reservoir condition. In WinProp CMG (2016), a two-phase envelope and two-phase flash calculations are performed at initial reservoir temperature of 220 º F and initial reservoir pressure of 4500 psia. At the given compositions and temperature, the dew point pressure is calculated to be 3464 psia by using the Peng-Robinson EOS. For later calculations, the reservoir volume is set to be 4000 X 1000 X 300 cubic feet, porosity is around 0.03, and TOC is 5% (Dunn, 2012). Based on these assumptions, the adsorbent amount is estimated to be 1700 tons in 1000 lbmol fluid mixtures. At this saturation pressure condition, equilibrium properties are obtained by WinProp (2016) and the data are given in Table 4.3.

Table 4.3: Vapor and liquid phase compositions at dew point pressure of 3464 psia and reservoir temperature of 220 º F

Component	Composition	Liquid phase composition x_i	Vapor phase composition y_i
CO_2	0.0053	0.0053	0.0053
N_2	0.0057	0.0054	0.0057
CH_4	0.6845	0.6687	0.6845
C_2H_6	0.1016	0.1019	0.1016
C_3H_8	0.0505	0.0516	0.0505
IC_4	0.0082	0.0084	0.0082
NC_4	0.0127	0.0132	0.0127
IC_5	0.0164	0.0173	0.0164
NC_5	0.0138	0.0146	0.0138
FC_6	0.0308	0.0330	0.0308
C_{7+}	0.0705	0.0806	0.0705

Second, adsorption capacity needs to be calculated at the saturation pressure by the ideal adsorbed solution theory. The Langmuir volume and Langmuir pressure of each component have been selected and presented based on experimental data from Accumap. Therefore, by using the Langmuir isothermal equations (4.7) and (4.8), adsorption capacity is calculated and presented in Table 4.4.

$$V_i = V_{Li}\frac{P_g}{P_{Li}+P_g} \tag{4.7}$$

$$n_i = n_{Li}\frac{P_g}{P_{Li}+P_g} \tag{4.8}$$

Table 4.4: Adsorption capacity at dew point pressure of 3464 psi and reservoir temperature of 220 º F

Component	V_{Li} (SCF/ton)	P_{Li} (psia)	Adsorption capacity (lbmol/ton)
CO_2	150	455	0.0019
N_2	30	1400	0.0003
CH_4	60	1100	0.0822
C_2H_6	90	811	0.0196
C_3H_8	180	800	0.0195
IC_4	190	500	0.0036
NC_4	200	480	0.0059
IC_5	220	350	0.0086
NC_5	240	320	0.0080
FC_6	270	300	0.0202
C_{7+}	300	250	0.0520

Third, the surface excess of the vapor phase needs to be obtained. At the saturation condition, the surface excess of the vapor phase is approximately equal to the surface excess of the liquid phase. Then the amount of the adsorbed liquid at the liquid-solid interface is estimated first and is used to find the surface excess of the vapor phase. As discussed previously, adsorbent is estimated to be 1700 tons. Based on the surface excess equations (4.5) and (4.6), calculation results are obtained and shown in Table 4.5.

Table 4.5: Surface excess of vapor phase and liquid phase

Component	n_i^* $(lbmol)$	$x_i\left(\sum n_i^*\right)$ $(lbmol)$	Surface Excess of vapor phase n_i^{ev} (lbmol)	Surface Excess of liquid phase n_i^e (lbmol)
CO_2	3.1698	2.0062	1.1636	1.1636
N_2	0.5434	2.0494	-1.5060	-1.5060
CH_4	139.8192	252.1862	-112.3671	-112.3671
C_2H_6	33.2409	38.4253	-5.1844	-5.1844
C_3H_8	33.1234	19.4404	13.6830	13.6830
IC_4	6.0697	3.1746	2.8950	2.8950
NC_4	10.0302	4.9876	5.0426	5.0426
IC_5	14.6985	6.5053	8.1932	8.1932
NC_5	13.5996	5.4954	8.1042	8.1042
FC_6	34.3283	12.4465	21.8818	21.8818
C_{7+}	88.4822	30.3882	58.0940	58.0940
SUM	377.1051			

From the above table, a total 377 lbmol of gas was adsorbed initially based on the IAST calculations.

Moreover, adsorption capacity can be affected by the molecular weight of a component and the mole fraction of that component. As the molecular weight becomes larger, the maximum adsorbed gas volume is increased as well. Therefore, adsorption capacity is also increased. That is the reason that a comparably large amount of the adsorbed gas is attributed to C_{7+} as 88.48 lbmol initially. Similarly, as the mole fraction becomes larger, the maximum adsorbed gas volume is increased as well. Since the highest amount of the mole fraction is attributed to CH_4, the initially largest amount of the adsorbed gas is attributed to CH_4 as 139.82 lbmol.

In addition, some negative surface excess values representing the amount of the adsorbed liquid are large enough and even more than the total adsorbed fluids. This phenomenon is an indicative of that a phase change should be considered during the adsorption process. Such CH_4 yields a negative value of 112.37 lbmol, which indicates that there is a huge amount of the adsorbed liquid at the liquid-solid interface when the dew point condition is applied, since CH_4 is more sensitive to pressure.

Finally, by using the definition of success excess of the liquid phase, the liquid phase compositions after contacting with adsorbent are calculated by applying equation (4.4). Similarly, the gas phase compositions can also be calculated. Table 4.6 and Table 4.7 summarize these calculated values.

Table 4.6: Liquid phase compositions after contact with adsorbent

Component	x_i^*	Liquid phase composition after contact x_i	% change
CO_2	0.0053	0.0052	-2.74%
N_2	0.0054	0.0065	20.42%
CH_4	0.6687	0.6692	0.07%
C_2H_6	0.1019	0.1020	0.08%
C_3H_8	0.0516	0.0514	-0.30%
IC_4	0.0084	0.0082	-2.25%
NC_4	0.0132	0.0130	-1.50%
IC_5	0.0173	0.0170	-1.27%
NC_5	0.0146	0.0143	-1.62%
FC_6	0.0330	0.0328	-0.75%
C_{7+}	0.0806	0.0803	-0.31%

Table 4.7: Gas phase compositions after contact with adsorbent

Component	y_i^*	Vapor phase composition after contact y_i	% change
CO_2	0.0053	0.0052	-2.75%
N_2	0.0057	0.0068	19.55%
CH_4	0.6845	0.6848	0.05%
C_2H_6	0.1016	0.1017	0.06%
C_3H_8	0.0505	0.0503	-0.33%
IC_4	0.0082	0.0080	-2.34%
NC_4	0.0127	0.0125	-1.58%
IC_5	0.0164	0.0162	-1.36%
NC_5	0.0138	0.0136	-1.73%
FC_6	0.0308	0.0305	-0.83%
C_{7+}	0.0705	0.0702	-0.37%

A two-phase envelope is generated by applying these values into the WinProp CMG (2016), which is shown in Figure 4.2. It is noted that the two-phase envelope is slightly swelled by considering the compositional change during the effective adsorbed phase calculations. Parts of the adsorbed gas were traded as single gases before the ideal adsorbed solution theory is applied. However, when this IAST method is imposed, phase change during the pressure depletion is considered and the adsorbed gas is traded as adsorbed gas, which fixes those previously existent mistakes. In this study at the reservoir temperature of 220 ºF and the reservoir pressure of 4500 psia, the compositional difference between the original and IAST cases is not large. A relatively small oil and gas production difference will be expected in the Chapter 5.

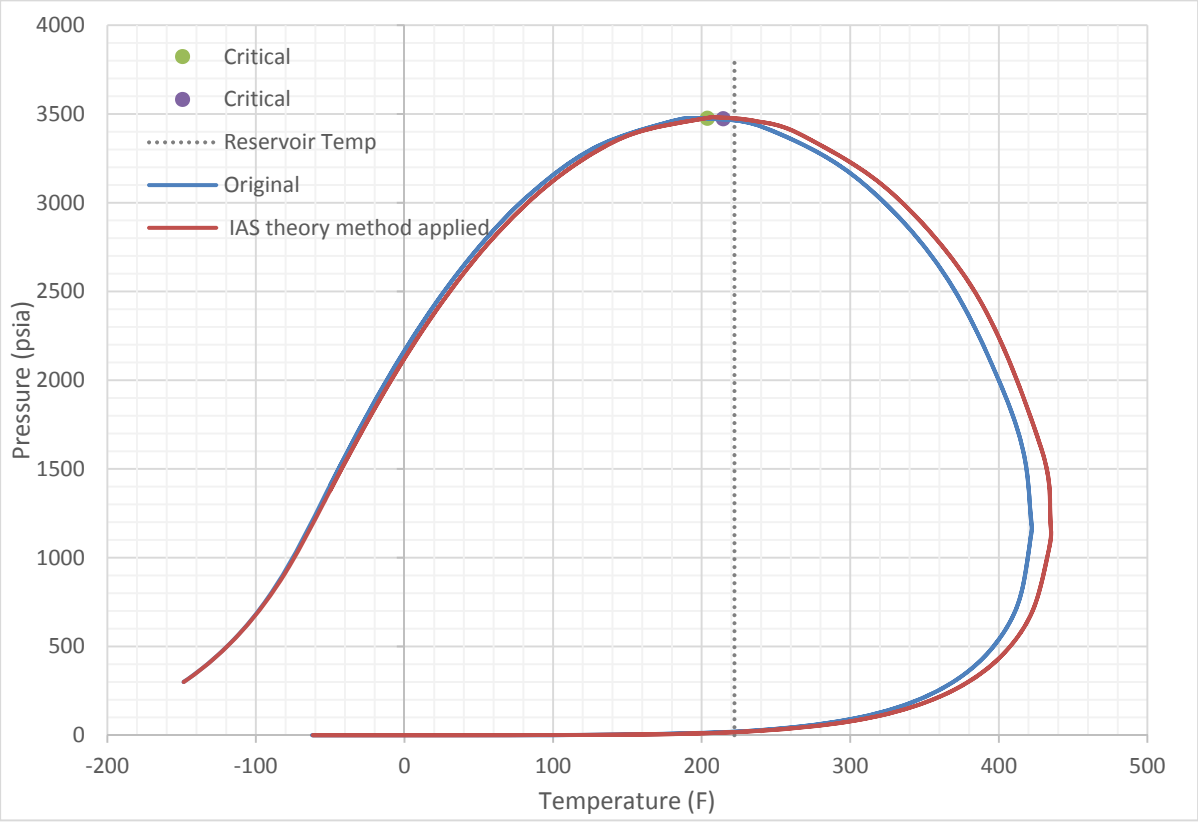

Figure 4.2: Comparison of two phase envelope between the original case and IAST case

Additionally, the percentage of the vapor phase volume changing with pressure is plotted for both the original case and the IAST case, as shown in Figure 4.3. Similarly, Figure 4.4 presents the percentage of the liquid phase volume changing with pressure for both the original case and the IAST case. From these figures, it is observed that the vapor phase volume slightly decreased by considering the IAST calculation, which supports the expectation. Also, the liquid phase volume slightly increased by considering the IAST calculation. It is because those parts of the adsorbed gas were traded as single gases before the ideal adsorbed solution theory is applied. When the IAST method is imposed, a phase change during the pressure depletion is considered and the adsorbed gas is traded as adsorbed gas, which fixes those previously existent mistakes. Therefore, the liquid phase volume is slightly increased and the vapor phase volume is slightly decreased.

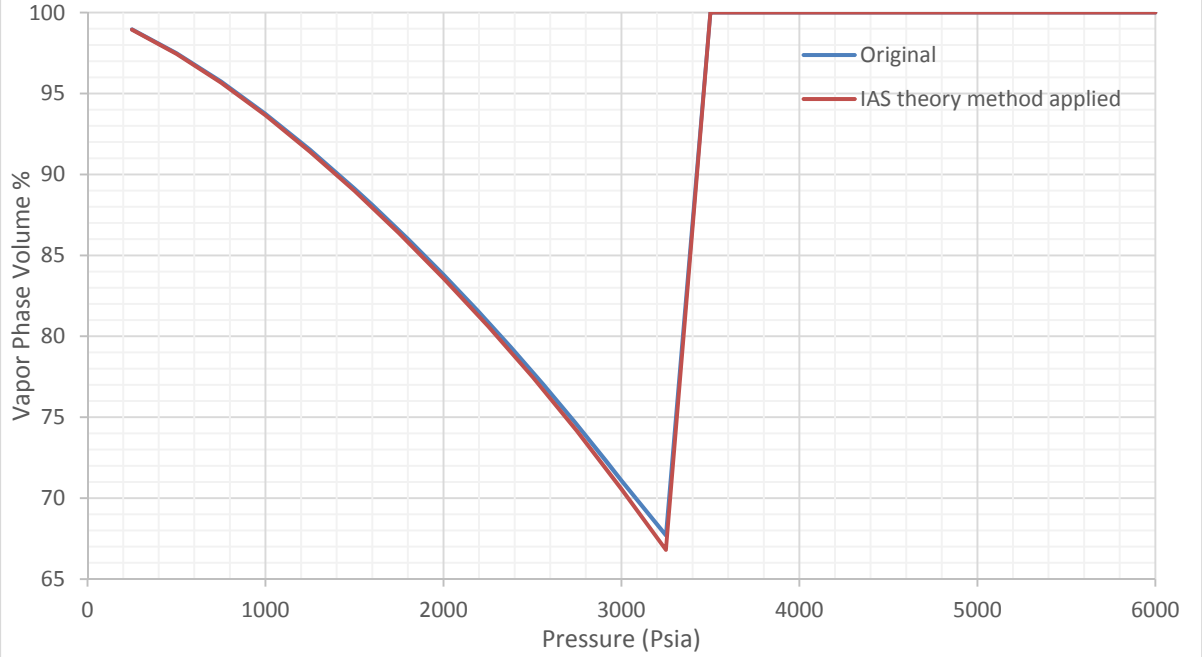

Figure 4.3: Comparison of vapor phase volume between the original case and the IAST case

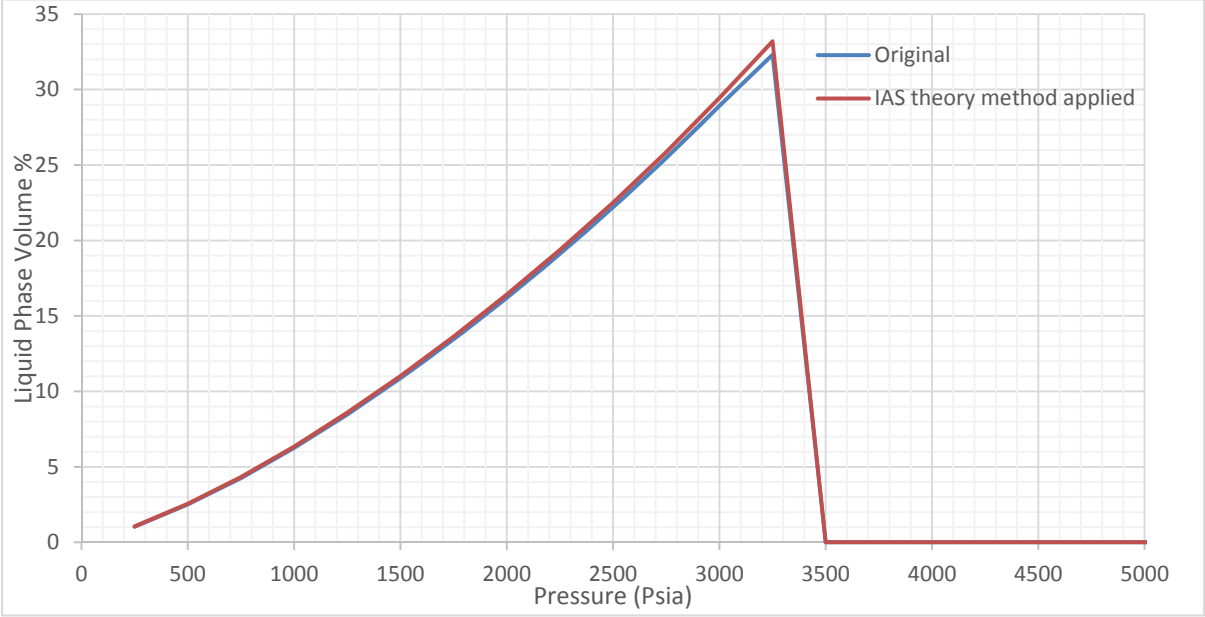

Figure 4.4: Comparison of liquid phase volume between the original case and the IAST case

Table 4.8: Gas compositions and experimental data for IAST-EL model

					Input number into GEM	
Component	composition	MW	V_{Li} (SCF/ton)	P_{Li} (psia)	V_{Li} ((gmol/lb)	$\frac{1}{P_{Li}}$ (1/psia)
CO_2	0.0052	44.010	150	455	0.0897	0.0022
N_2	0.0068	28.013	30	1400	0.0179	0.0007
CH_4	0.6848	16.043	60	1100	0.0359	0.0009
C_2H_6	0.1017	30.070	90	811	0.0538	0.0012
C_3H_8	0.0503	44.097	180	800	0.1076	0.0013
IC_4	0.0080	58.124	190	500	0.1136	0.0020
NC_4	0.0125	58.124	200	480	0.1195	0.0021
IC_5	0.0162	72.151	220	350	0.1315	0.0029
NC_5	0.0136	72.151	240	320	0.1434	0.0031
FC_6	0.0305	86.000	270	300	0.1614	0.0033
C_{7+}	0.0702	145.000	300	250	0.1793	0.0040

The fluid system compositions and experimental Langmuir data for the IAST-EL model are presented in Table 4.8 for a further study. Right now, three models that are based on different methodologies have been established, including the ML model, EL model, and IAST–EL model. In Chapter 5, these models will be validated in the simulator and result in a production performance for further comparison. So, before I move to the next chapter, a Monte Carlo simulation is carried out to assess the impact of each variable on the output to deepen the understanding of these methodologies.

4.3 Monte Carlo Simulation and Sensitivity Analysis

Based on the IAST correlations, there are different variables that may affect the value of total moles of gas adsorbed. In order to use these new correlations to estimate the total moles of gas adsorbed, the impact of each variable on the output needs to be assessed. Since I only focus on the trend of total moles of gas adsorbed changes with random variables, the One Variable at the Time (OVAT) technique is sufficient to reduce the run time, which is only one variable changes at the time while keeping other variables constant. Moreover, the interactions between the random variables are ignored in this approach.

4.3.1 CH_4 Monte Carlo Simulation

Since the highest composition is attributed to CH_4 in shale gas reservoirs, a Monte Carlo simulation is carried out on the component of CH_4 to represent the light components. In this approach, variables including the Langmuir volume of CH_4, the Langmuir pressure of CH_4, and the amount of adsorbent are included in the CH_4 Monte Carlo simulation. The Duvernay formation has an average CH_4 Langmuir volume varying from 40 SCF/ton to 80 SCF/ton and an average CH_4

Langmuir pressure varying from 800 psia to 1500 psia. The amount of adsorbent is calculated to be around 1700 tons, which helps us to estimate the amount of adsorbent varying from 1300 tons to 2100 tons. Table 4.9 shows the deviation of the total moles gas adsorbed by changing the variables including the Langmuir volume of CH_4, the Langmuir pressure of CH_4, and the amount of adsorbent.

Table 4.9: Deviation of total moles gas adsorbed by changing CH_4 properties

	$Total\ moles\ gas\ adsorbed\ (lbmol)$ $\sum n_i^*$			Deviation $(lbmol)$ $(\sum n_i^* - \sum n_i^{*^0})$	
	Original	Lower	Upper	- Deviation	+ Deviation
CH_4 V_{Li} (40 SCF/ton, 80SCF/ton)	377.105	330.499	423.712	-46.606	46.606
CH_4 P_{Li} (800 psia , 1500 psia)	377.105	386.942	365.838	9.837	-11.267
Adsorbent (1300 tons, 2100 tons)	377.105	344.207	410.004	-32.899	32.899

By using the above table, a Tornado chart is generated to quantify the impact of each variable on the deviation of the total moles gas adsorbed. Figure 4.5 shows how total moles gas adsorbed deviates from the original value if only one variable changes at the time. From the plot, the deviation forms by the Langmuir volume of CH_4 is observed to be larger than the deviation forms by the Langmuir pressure of CH_4 and the amount of adsorbent. Although both the Langmuir volume and the amount of adsorbent have a proportional relationship with the total moles gas adsorbed, the Langmuir volume of CH_4 still affects the most on the total moles gas adsorbed. Moreover, the Langmuir pressure yields an inverse proportional relationship with the total moles

gas adsorbed, which means that as the Langmuir pressure increases, less total moles gas adsorbed is presented. However, the effect of the Langmuir pressure on the total moles gas adsorbed is not that profound. For light components, the Langmuir volumes have effects on the total moles gas adsorbed that are larger than those by the Langmuir pressures and the amount of adsorbent in the adsorption system. Therefore, we need to have sufficient knowledge in obtaining both the Langmuir temperature and the amount of adsorbent for light components.

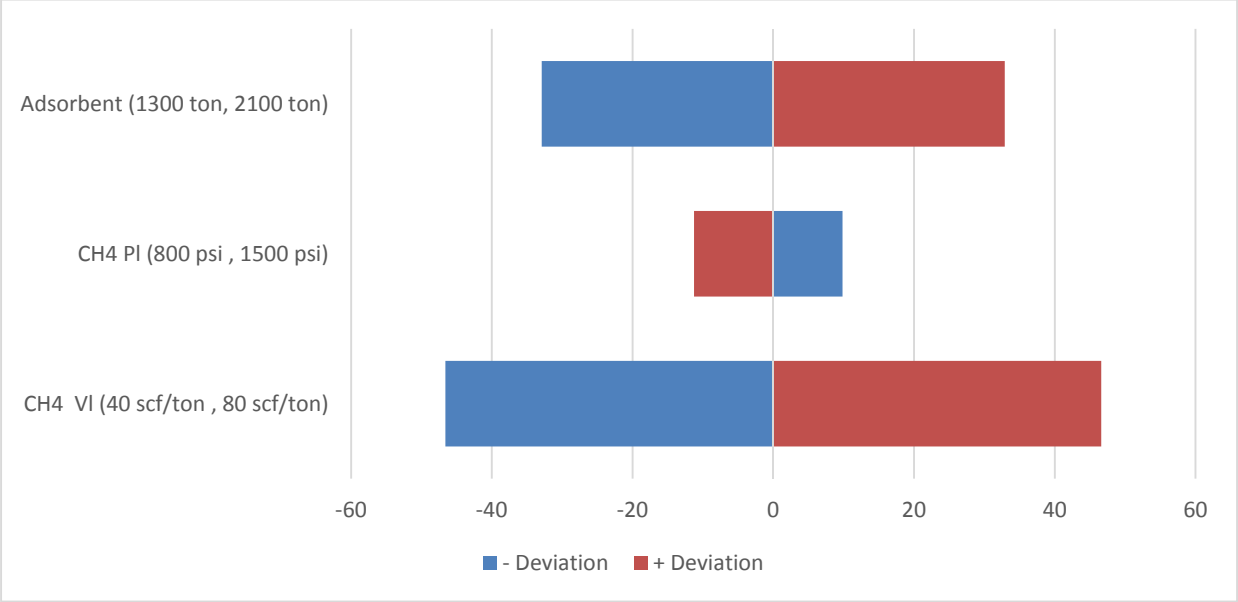

Figure 4.5: Tornado chart on the deviation of total moles gas adsorbed by changing CH_4 properties

4.3.2 C_{7+} Monte Carlo Simulation

Additionally, C_{7+} is not only the heaviest component but also a lumped component, which means that the Langmuir volume and the Langmuir pressure of C_{7+} may not be accurate enough. Therefore, a Monte Carlo simulation is also carried out on the component of C_{7+} to represent the trend of the heavy components including the Langmuir volume of C_{7+}, the Langmuir pressure of

C_{7+}, and the amount of adsorbent. Similar to the CH_4 Monte Carlo case, the amount of adsorbent varies from 1300 tons to 2100 tons. Based on the research results, the Langmuir volume of C_{7+} varies from 260 SCF/ton to 340 SCF/ton and the Langmuir pressure of C_{7+} varies from 150 psia to 450 psia. Tables 4.10 shows the deviation of the total moles gas adsorbed by changing variables including the Langmuir volume of C_{7+}, the Langmuir pressure of C_{7+}, and the amount of adsorbent.

Table 4.10: Deviation of total moles gas adsorbed by changing C_{7+} properties

	$Total\ moles\ gas\ adsorbed\ (lbmol)$ $\sum n_i^*$			Deviation $(lbmol)$ $(\sum n_i^* - \sum n_i^{*0})$	
	Original	Lower	Upper	- Deviation	+ Deviation
C_{7+} V_{Li} (260SCF/ton,340SCF/ton)	377.105	365.308	388.903	-11.798	11.798
C_{7+} P_{Li} (150 psia , 450 psia)	377.105	379.553	372.584	2.448	-4.521
Adsorbent (1300 tons, 2100 tons)	377.105	356.286	397.924	-20.819	20.819

By using the above table, a Tornado chart is generated to quantify the impact of each variable on the deviation of the total moles gas adsorbed. Figure 4.6 presents how total moles gas adsorbed deviates from the original value if only one variable changes at the time. From the plot, the deviation forms by the amount of adsorbent is observed to be larger than the deviation forms by the Langmuir pressure of C_{7+} and the Langmuir volume of C_{7+}, which has a different result than the CH_4 Monte Carlo simulation case. Although both the Langmuir volume and the amount of adsorbent have a proportional relationship with the total moles gas adsorbed, the amount of adsorbent still affects the most on the total moles gas adsorbed. This phenomenon is because the

low composition is attributed to C_{7+}. Therefore, as the composition of C_{7+} increases, the deviation forms by the Langmuir volumes of C_{7+} will also increase to be the most important factor. Additionally, the Langmuir pressure has an inverse proportional relationship with the total moles gas adsorbed, which means that as the Langmuir pressure of C_{7+} increases, less total moles gas adsorbed is presented. That has the same results compared to the CH_4 Monte Carlo case.

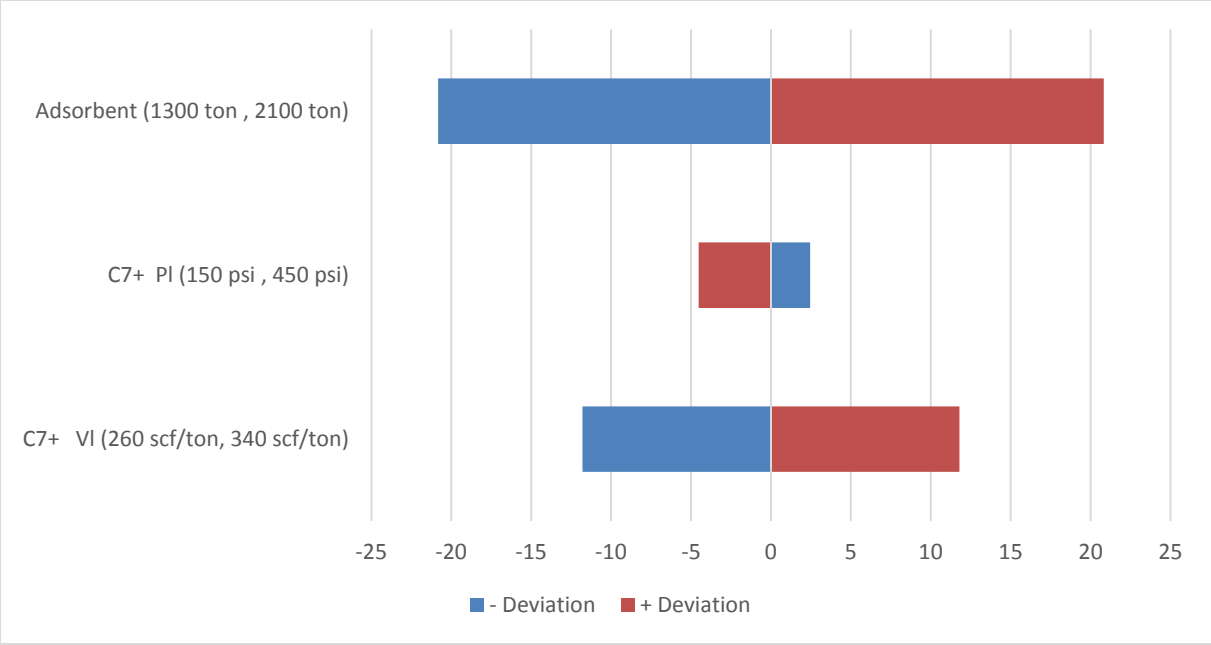

Figure 4.6: Tornado chart on the deviation of total moles gas adsorbed by changing C_{7+} properties

4.3.3 Combination Results

A combination study of these two sensitivity cases is shown in Figure 4.7. From this plot, the deviation forms by the Langmuir volume of CH_4 is observed to be the largest and then followed by the amount of adsorbent in the CH_4 case, the amount of adsorbent in the C_{7+} case, the Langmuir volume of C_{7+}, the Langmuir pressure of CH_4, and the Langmuir pressure of C_{7+}. Therefore, a

conclusion can be reached that for not only light components but also heavy components, Langmuir volumes affect more than Langmuir pressures and the amount of adsorbent in the adsorption system. However, as the composition of that single component decreases, the amount of adsorbent also has a chance to play an important role in the adsorption system. In addition, even the smallest case presents that at least 330 lbmol adsorbed gas in shale organics are neglected, if the adsorption effect has not been included. Consequently, we need to have sufficient knowledge in obtaining both the Langmuir volumes and the amount of adsorbent for modelling an adsorption effect.

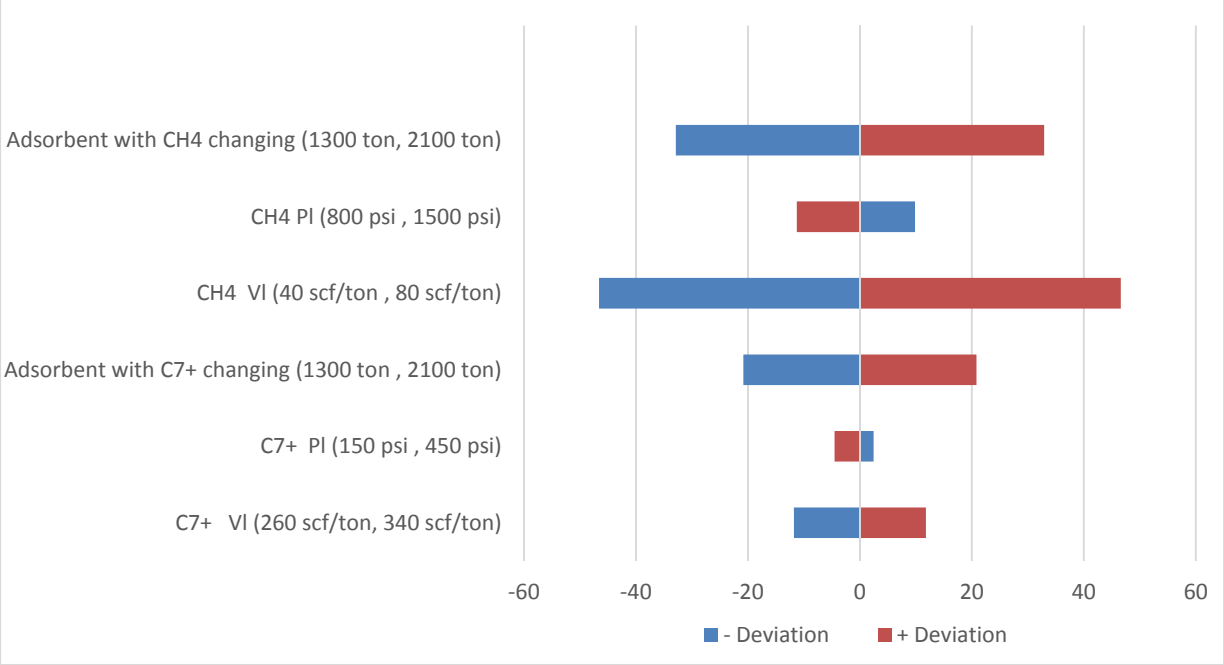

Figure 4.7: Tornado chart on the deviation of total moles gas adsorbed by changing both the CH_4 and C_{7+} properties

Chapter Five: **Confinement Adsorption and Diffusion Effects on Production Behavior**

5.1 Numerical Compositional Model

In the previous two chapters, a compositional Duverany gas condensate with the confinement and the adsorption effect considered PVT is developed in WinProp (2016) to describe the fluid phase behaviors. In this chapter, a three-dimensional, three-phase, dual-porosity, dual-permeability, and multi-mechanistic compositional Duverany gas condensate model is established in GEM (2016) to account for the confinement, adsorption, and diffusion effects on shale oil and gas production performance.

Table 5.1: Reservoir properties

Parameter	Value
Reservoir size (ft)	$4000 \times 1000 \times 300$
Number of Grid block	$80 \times 20 \times 10$
Grid thickness I direction (ft)	50
Grid thickness J direction (ft)	50
Grid thickness K direction (ft)	30
Grid top (ft)	10500
Reservoir temperature (ºF)	220
Initial reservoir pressure (psia)	4500
Matrix porosity	0.0344
Natural fracture porosity	4×10^{-5}
Initial matrix permeability (md)	0.0004
Natural fracture permeability (i,j,k) (md)	$2 \times 10^{-5}, 2 \times 10^{-5}, 4 \times 10^{-5}$
Fracture spacing (ft)	50
Matrix initial water saturation	0.2
Fracture initial water saturation	0.2

The relevant input data of reservoir properties are given in Table 5.1, which are based on the CMG's published resources and business intelligence, and the compositional properties are given

in Table 5.2, which are based on the Accumap. As discussed in Chapter 2, due to the nature of low permeability in the matrix, hydraulic fracturing along horizontal wells needs to be established to create freeways for the fluid flow and fracture properties for complex fracture model are given in Table 5.3, which based on the same CMG's published resources and business intelligence. The non-Darcy flow option has been included in all the cases presented in this section. As the basic case, the effects of confinement, adsorption, and diffusion are neglected at this moment. The total production time is set to be 5 years.

Table 5.2: Component compositional properties

Component	Composition	MW	P_{cb}^{*} (atm)	T_{cb}^{*} (K)	Acentric factor
CO_2	0.0053	44.01	72.80	304.20	0.225
N_2	0.0057	28.01	33.50	126.20	0.040
CH_4	0.6845	16.04	45.40	190.60	0.008
C_2H_6	0.1016	30.07	48.20	305.40	0.098
C_3H_8	0.0505	44.10	41.90	369.80	0.152
IC_4	0.0082	58.12	36.00	408.10	0.176
NC_4	0.0127	58.12	37.50	425.20	0.193
IC_5	0.0164	72.15	33.40	460.40	0.227
NC_5	0.0138	72.15	33.30	469.60	0.251
FC_6	0.0308	86.00	32.46	507.50	0.275
C_{7+}	0.0705	145.00	22.38	641.58	0.435

Table 5.3: Fracture properties for complex fracture model

Parameter	Value
SRV size (number of grid block)	75×11
Fracture width (ft)	0.001
Fracture height (ft)	180
Intrinsic permeability (md)	10000

5.2 Comparison of Confinement Model

A complex fracture model with the SRV size of 75×11 and the flow-back effect included is established as the basic case for a further study of nano-pore confinement. Previously in Chapter 3, the effect of molecule-wall interactions has been explained and related PVT models have been developed to take the change of critical properties into account. In this approach, a confinement effect model with only a pore size considered is applied in GEM (2016) first as case 1. The equations suggested by Zarragoicoechea and Kuz (2004) were applied to modify the critical temperatures and critical pressures at different pore radii, as shown in Table 5.4 and Table 5.5.

Table 5.4: Case 1 - Component compositional properties when considering the confinement effect at different pore sizes

		Original case		r_p = 50 nm case		r_p = 10 nm case	
Component	Composition	Pc (atm)	Tc (K)	Pc (atm)	Tc (K)	Pc (atm)	Tc (K)
CO_2	0.0053	72.80	304.20	72.76	304.03	72.60	303.35
N_2	0.0057	33.50	126.20	33.48	126.13	33.41	125.87
CH_4	0.6845	45.40	190.60	45.38	190.49	45.27	190.07
C_2H_6	0.1016	48.20	305.40	48.17	305.19	48.03	304.35
C_3H_8	0.0505	41.90	369.80	41.87	369.50	41.73	368.30
IC_4	0.0082	36.00	408.10	35.97	407.72	35.84	406.22
NC_4	0.0127	37.50	425.20	37.47	424.81	37.33	423.25
IC_5	0.0164	33.40	460.40	33.37	459.93	33.23	458.07
NC_5	0.0138	33.30	469.60	33.27	469.12	33.13	467.19
FC_6	0.0308	32.46	507.50	32.43	506.95	32.29	504.76
C_{7+}	0.0705	22.38	641.58	22.34	640.64	22.21	636.89

Table 5.5: Case 1 - Component compositional properties when considering the confinement effect at different pore sizes

		r_p = 5 nm case		r_p = 2.4 nm case		r_p = 1 nm case	
Component	Composition	Pc (atm)	Tc (K)	Pc (atm)	Tc (K)	Pc (atm)	Tc (K)
CO_2	0.0053	72.39	302.50	71.96	300.70	70.78	295.77
N_2	0.0057	33.32	125.53	33.13	124.82	32.62	122.88
CH_4	0.6845	45.15	189.53	44.88	188.40	44.14	185.30
C_2H_6	0.1016	47.87	303.30	47.52	301.08	46.56	294.99
C_3H_8	0.0505	41.56	366.80	41.20	363.63	40.22	354.95
IC_4	0.0082	35.67	404.35	35.32	400.38	34.36	389.56
NC_4	0.0127	37.16	421.30	36.79	417.16	35.80	405.88
IC_5	0.0164	33.06	455.74	32.70	450.81	31.73	437.36
NC_5	0.0138	32.96	464.79	32.60	459.70	31.62	445.83
FC_6	0.0308	32.11	502.03	31.74	496.24	30.73	480.48
C_{7+}	0.0705	22.05	632.22	21.71	622.34	20.77	595.56

Similar to the expectation that was depicted in Chapter 3, cumulative oil production is increased when considering the effect of confinement that is compared to the base case, as shown in Figure 5.1. In addition, if the pore radius is larger than 50 nm, the results when the confinement effect is considered and ignored are almost the same, which also supports that the confinement effect can be neglected if a pore size is larger than 50 nm. In other words, the confinement effect on oil and gas production becomes more and more crucial as pore radii decrease. Therefore, it can reach the conclusion that at same reservoir conditions, the effect of nano-pore confinement on production behavior is significant and cannot be neglected for nano pore radius reservoirs. It does not mean that the pore sizes the smaller the better. It only shows that the effect of nano-pore confinement becomes more and more crucial as pore radii decrease.

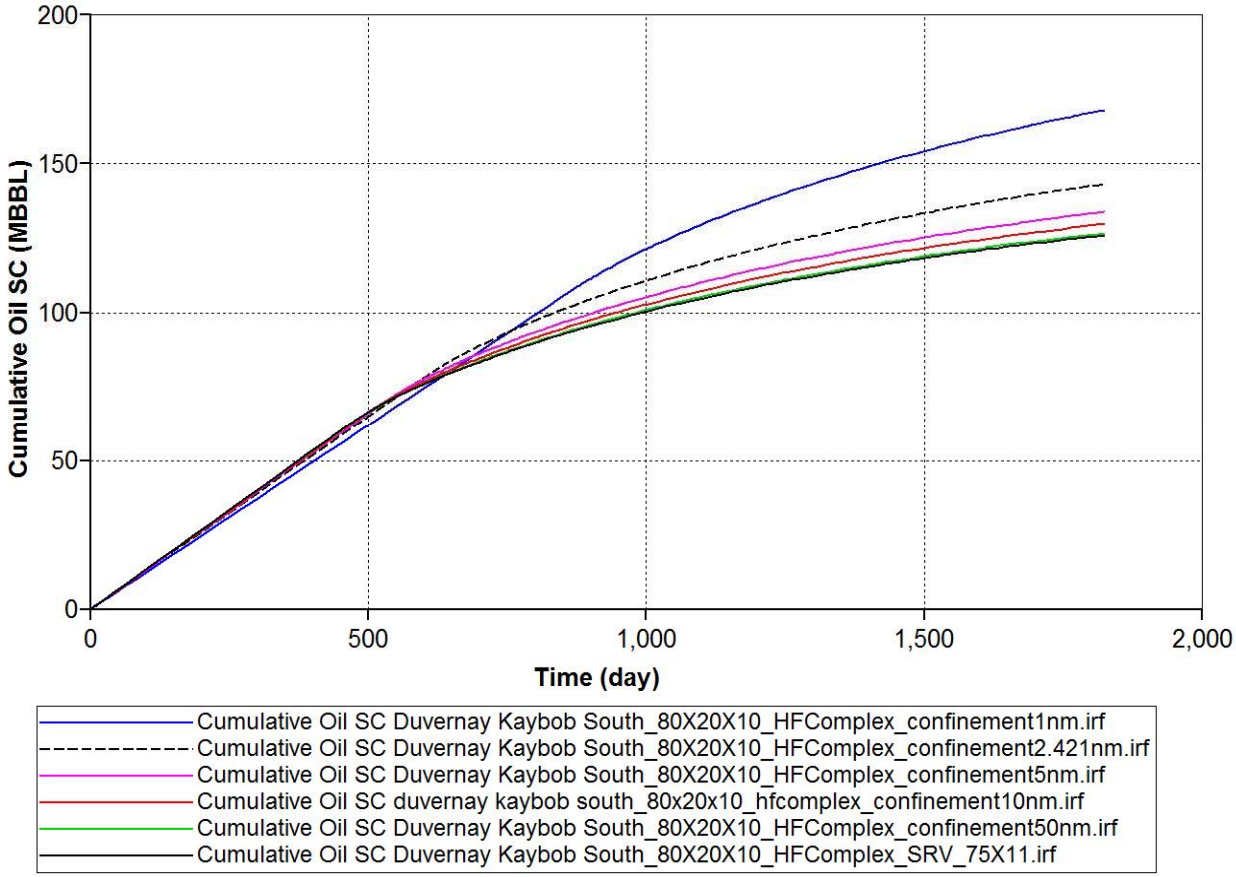

Figure 5.1: Case 1 - Comparison of cumulative oil productions when considering the confinement effect at different pore sizes

Next, due to the nature of a sorption process existing in shales, a new confinement model is applied to not only considering the changing of a pore size but also take the correction of the adsorbed phase density into account. Similarly, the equations suggested by Bilgesu (2016) were applied to modify the critical temperatures and critical pressures and the related PVT models were established in Chapter 3. Two confinement cases are obtained by using two different methodologies. Case 1 is set to only take the changing of a pore size into account and case 2 is set to take both the pore size and the adsorbed phase density correction into account. In Table 5.6, a comparison of component properties at a pore radius of 50 nm is obtained. These cases are the original case, case

1 at $r_p = 50\ nm$, and case 2 at $r_p = 50\ nm$. Based on the data from Table 5.6, critical temperatures and critical pressures from three cases are almost the same at the pore size of 50 nm, which evidences that the effect of confinement can be neglected at large pore radii.

Table 5.6: Comparison of compositional properties among original case, case 1 at $r_p = 50$ nm, and case 2 at $r_p = 50$ nm

		Original case		Case 1		Case 2	
		r_p = 50 nm		r_p = 50 nm		r_p = 50 nm	
Component	Composition	Pc (atm)	Tc (K)	Pc (atm)	Tc (K)	Pc (atm)	Tc (K)
CO_2	0.0053	72.80	304.20	72.76	304.03	72.47	304.18
N_2	0.0057	33.50	126.20	33.48	126.13	33.35	126.19
CH_4	0.6845	45.40	190.60	45.38	190.49	45.19	190.59
C_2H_6	0.1016	48.20	305.40	48.17	305.19	47.93	305.37
C_3H_8	0.0505	41.90	369.80	41.87	369.50	41.62	369.76
IC_4	0.0082	36.00	408.10	35.97	407.72	35.73	408.05
NC_4	0.0127	37.50	425.20	37.47	424.81	37.22	425.15
IC_5	0.0164	33.40	460.40	33.37	459.93	33.12	460.34
NC_5	0.0138	33.30	469.60	33.27	469.12	33.02	469.54
FC_6	0.0308	32.46	507.50	32.43	506.95	32.17	507.43
C_{7+}	0.0705	22.38	641.58	22.34	640.64	22.11	641.46

In Table 5.7 and Table 5.8, the comparison of compositional properties at different pore sizes are obtained to compare the results from case 1 and case 2.

Table 5.7: Case1 & Case2 - Comparison of compositional properties at different pore sizes

	r_p = 10 nm				r_p = 5 nm			
	Case 1		Case 2		Case 1		Case 2	
Component	Pc (atm)	Tc (K)	Pc (atm)	Tc (K)	Pc (atm)	Tc (K)	Pc (atm)	Tc (K)
CO_2	72.60	303.35	71.13	304.10	72.39	302.50	69.46	303.99
N_2	33.41	125.87	32.77	126.16	33.32	125.53	32.04	126.12
CH_4	45.27	190.07	44.36	190.54	45.15	189.53	43.31	190.47
C_2H_6	48.03	304.35	46.84	305.27	47.87	303.30	45.48	305.15
C_3H_8	41.73	368.30	40.50	369.62	41.56	366.80	39.11	369.44
IC_4	35.84	406.22	34.64	407.87	35.67	404.35	33.28	407.64
NC_4	37.33	423.25	36.08	424.96	37.16	421.30	34.67	424.73
IC_5	33.23	458.07	32.01	460.12	33.06	455.74	30.62	459.83
NC_5	33.13	467.19	31.90	469.31	32.96	464.79	30.50	469.02
FC_6	32.29	504.76	31.02	507.17	32.11	502.03	29.58	506.84
C_{7+}	22.21	636.89	21.03	641.01	22.05	632.22	19.69	640.44

Table 5.8: Case1 & Case2 - Comparison of compositional properties at different pore sizes

	r_p = 2.4 nm				r_p = 1 nm			
	Case 1		Case 2		Case 1		Case 2	
Component	Pc (atm)	Tc (K)	Pc (atm)	Tc (K)	Pc (atm)	Tc (K)	Pc (atm)	Tc (K)
CO_2	71.96	300.70	65.91	303.78	70.78	295.77	56.20	303.18
N_2	33.13	124.82	30.49	126.03	32.62	122.88	26.24	125.80
CH_4	44.88	188.40	41.09	190.33	44.14	185.30	35.02	189.96
C_2H_6	47.52	301.08	42.59	304.87	46.56	294.99	34.69	304.14
C_3H_8	41.20	363.63	36.15	369.05	40.22	354.95	28.06	368.00
IC_4	35.32	400.38	30.40	407.16	34.36	389.56	22.54	405.85
NC_4	36.79	417.16	31.67	424.22	35.80	405.88	23.48	422.85
IC_5	32.70	450.81	27.68	459.23	31.73	437.36	19.65	457.60
NC_5	32.60	459.70	27.53	468.40	31.62	445.83	19.44	466.71
FC_6	31.74	496.24	26.54	506.13	30.73	480.48	18.24	504.22
C_{7+}	21.71	622.34	16.86	639.24	20.77	595.56	9.18	635.98

Similar to the previous result that was obtained in case 1, cumulative oil production is increased with the consideration of the confinement effect that is compared to the original case, as shown in Figure 5.2. In addition, if the pore radius is larger than 50 nm, the results from the confinement case 2 and the confinement ignored case are almost the same. This phenomenon also demonstrates that the confinement effect can be neglected if a pore size is larger than 50 nm. It yields the same conclusion by applying the aforementioned two methodologies.

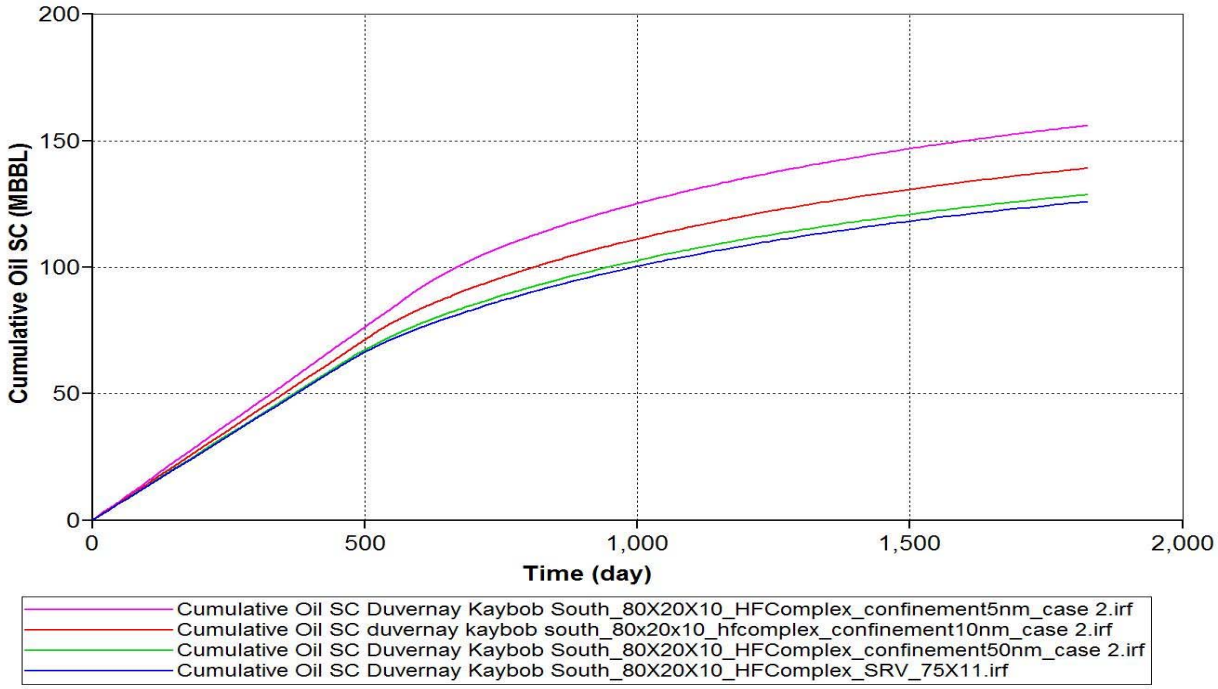

Figure 5.2: Case 2 - Comparison of cumulative oil productions when considering the confinement effect at different pore sizes

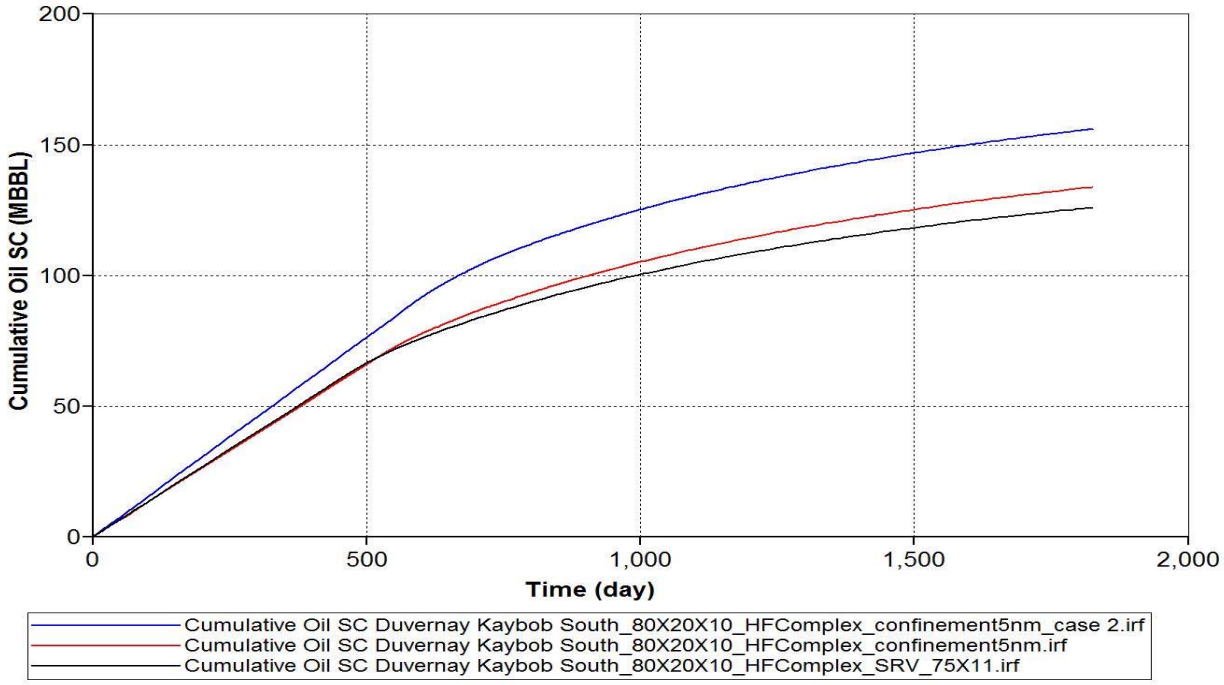

Figure 5.3: Case1 & Case2 - Comparison of cumulative oil productions at the pore radius of 2.4 nm

To achieve the comparison of cumulative oil production between case 1 and case 2, a figure is generated at a pore radius of 2.4 nm that is shown in Figure 5.3. From the plot, an increment in oil production is observed by using the second methodology, which is within our estimation. Since a sorption process exists in shales, not only changing of a pore size should be included but also the correction of the adsorbed phase density should be taken into account.

From the simulation results of case 1, it is observed that nano pore confinement can increase the total fluid recovery by 14% at a pore radius of 2.4 nm. From the simulation results of case 2, the confinement can account for even about 24% of the total fluid recovery at a pore size of 2.4 nm. Right now, two confinement cases are obtained by using two different methodologies in this study and the second case is much closer to reality that based on the existing of the organic matter in the

reservoir. Therefore, both the correction of the pore size and the adsorbed phase density should be considered and the second case will be used for further comparison.

5.3 Comparison of Adsorption Model

Similarly, a complex fracture model with the SRV size of 75×11 and the flow-back effect included is established as the basic case for the study of the sorption process. In Chapter 4, the phenomenon that parts of shale gases are stored as adsorbed gas on shale surfaces has been explained and related PVT models have been developed to take the thermodynamic consistency into account. In order to simulate the effect of adsorption, a variety of theoretical methods are developed including the ML model, EL model, and IAST-EL model.

First, a ML model which only considers the sorption of CH4 is established in GEM (2016). The Langmuir volume of CH_4 is assigned with different values as 0.0209 gmol/lb, 0.0359 gmol/lb, and 0.1 gmol/lb to make a comparison, as shown in Table 5.9. Based on the lab results from Sportfire, V_{Li} of CH_4 is estimated to around 0.0359 gmol/lb. A lower value of 0.0209 gmol/lb is set to be the compared case 1 and a higher value of 0.1 gmol/lb is set to be the compared case 2.

Table 5.9: Input data for Monolayer Langmuir model

	Component	V_{Li} (SCF/ton)	P_{Li} (psia)	V_{Li} ((gmol/lb)	$\frac{1}{P_{Li}}$ (1/psia)
Compared case 1	CH_4	35	1100	0.0209	0.0009
Real case	CH_4	60	1100	0.0359	0.0009
Compared case 2	CH_4	170	1100	0.1	0.0009

Figure 5.4 presents the comparison of cumulative oil production when considering the adsorption effect by using the Monolayer Langmuir model at different Langmuir volumes of CH_4. As the

Langmuir volume of CH_4 increases, more initial adsorbed CH_4 exists. Therefore, more cumulative oil production is presented. This understanding will help us to extend the ML model to the EL model.

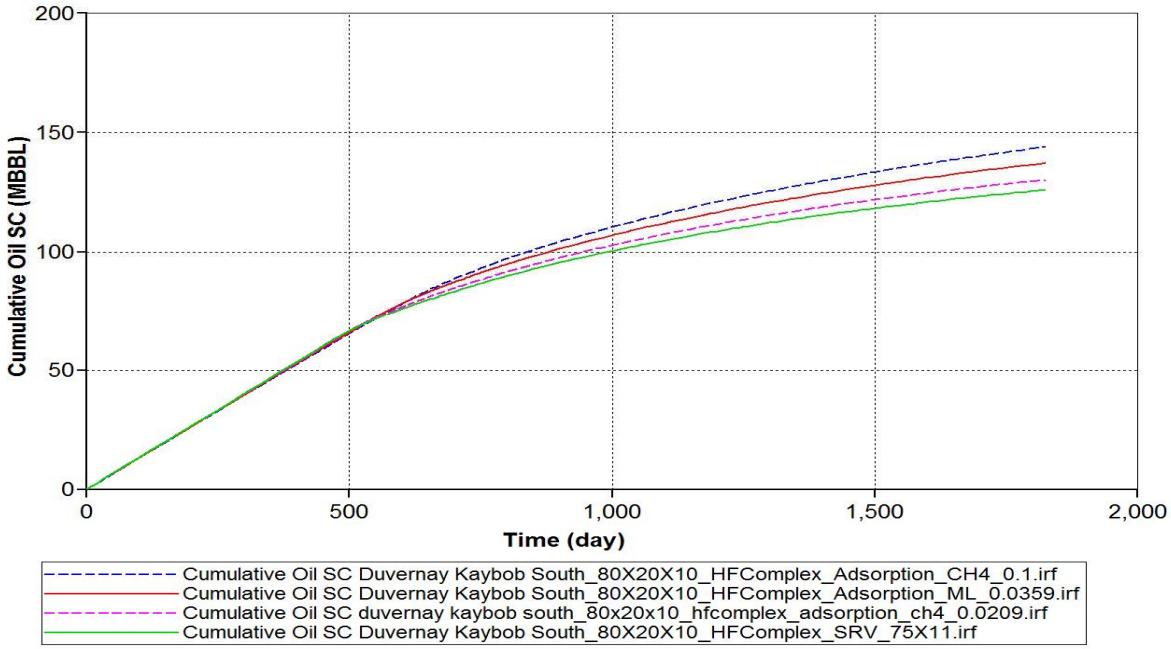

Figure 5.4: Comparison of cumulative oil productions when using Monolayer Langmuir models at different CH_4 Langmuir volumes

The Monolayer Langmuir model just developed for adsorbed gas is related to only one component and the aforementioned study demonstrates the significance of adsorbed gases' contribution to oil production. An extension is developed from a single component system to a multi-components system and the related Extend Langmuir model is established with the input data that based on the lab results from Sportfire, shown in Table 5.10.

Table 5.10: Input data for Extend Langmuir model

Component	Composition	V_{Li} (SCF/ton)	P_{Li} (psia)	V_{Li} ((gmol/lb)	$\frac{1}{P_{Li}}$ (1/psia)
CO_2	0.0053	150	455	0.0897	0.0022
N_2	0.0057	30	1400	0.0179	0.0007
CH_4	0.6845	60	1100	0.0359	0.0009
C_2H_6	0.1016	90	811	0.0538	0.0012
C_3H_8	0.0505	180	800	0.1076	0.0013
IC_4	0.0082	190	500	0.1136	0.0020
NC_4	0.0127	200	480	0.1195	0.0021
IC_5	0.0164	220	350	0.1315	0.0029
NC_5	0.0138	240	320	0.1434	0.0031
FC_6	0.0308	270	300	0.1614	0.0033
C_{7+}	0.0705	300	250	0.1793	0.0040

Table 5.11: Input data for IAST-EL model

Component	Composition	V_{Li} (SCF/ton)	P_{Li} (psia)	V_{Li} ((gmol/lb)	$\frac{1}{P_{Li}}$ (1/psia)
CO_2	0.0052	150	455	0.0897	0.0022
N_2	0.0068	30	1400	0.0179	0.0007
CH_4	0.6848	60	1100	0.0359	0.0009
C_2H_6	0.1017	90	811	0.0538	0.0012
C_3H_8	0.0503	180	800	0.1076	0.0013
IC_4	0.0080	190	500	0.1136	0.0020
NC_4	0.0125	200	480	0.1195	0.0021
IC_5	0.0162	220	350	0.1315	0.0029
NC_5	0.0136	240	320	0.1434	0.0031
FC_6	0.0305	270	300	0.1614	0.0033
C_{7+}	0.0702	300	250	0.1793	0.0040

However, the Extend Langmuir model still has limitations to simulate the adsorption effect. As pressure depletes, the compositional change of shale gas condensate is extremely large. This result is an indicative of that the thermodynamic consistency should be included during the modelling of a sorption process. In Chapter 4, a related PVT model has been developed, which is based on the ideal adsorbed solution theory. Subsequently, this PVT model is applied in GEM (2016) by using the Extend Langmuir methodology. All the input properties are shown in Table 5.11.

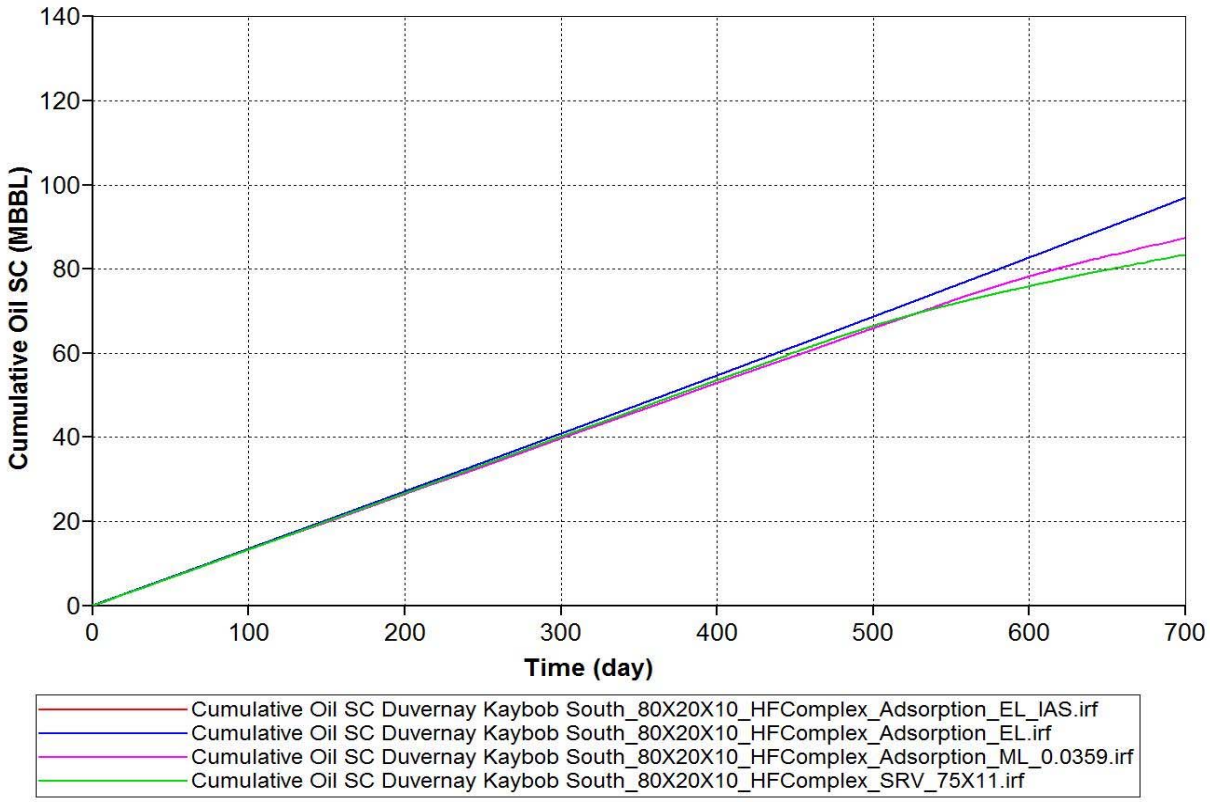

Figure 5.5: Comparison of cumulative oil productions when considering the adsorption effect by different methods

As a result, Figure 5.5 is plotted to show the comparison of cumulative oil production when considering the adsorption effect by different methodologies. A slight increase in the cumulative

oil production is observed when the Monolayer Langmuir model is applied. In addition, this increment in cumulative oil production becomes larger by applying the Extend Langmuir model. Since the EL model extends to a multi-components system, initial Langmuir volumes are increased, which means that more initial adsorbed gases exist in the reservoir. Accordingly, more cumulative oil production is presented. From the simulation results, it is found that adsorbed gas can account for 10% of the original fluid in place by applying the ML model and adsorbed gas can account for 21% of the original fluid in place by applying the EL model.

However, the cumulative oil curves that are plotted by the IAST-EL model and the EL model are almost superposed in 700 days' production. This phenomenon has been explained in Chapter 4 when we discussed the phase behaviors by applying the ideal adsorbed solution theory. As pressure depletes, the compositional change of shale gas condensate has been included during the modelling of the sorption process by using the ideal adsorbed solution theory. However, the two-phase envelope is just slightly swelled by such IAST method, which can estimate that the cumulative oil production does not yield a huge difference than just applying the EL model. Since the IAST-EL model is closer to reality, which considers the existing of the compositional change. Therefore, its result will be used for further comparison.

5.4 Comparison of Diffusion Model

Due to the nature of low permeability in the matrix for shale reservoirs, a multi-mechanistic flow containing convective flow and diffusive flow needs to be performed. As reservoir permeability decreases, convective flow may not respond to the fluid flow and the diffusive flow may play an important role in the transport system. In Chapter 2, the effective coefficients can be obtained to represent the diffusive flux. With the values of these effective coefficients, correlations in the CMG

GEM (2016) are imposed to calculate the gas and liquid phase diffusional fluxes. Therefore, the diffusion contribution to flow mechanisms is able to be evaluated for shale reservoirs. A variety of diffusion models are applied with different coefficient constants starting from 0.093 ft^2/day to 2.790 ft^2/day, as shown in Table 5.12. Case 2 with the coefficient of 0.930 ft^2/day is set to be the reference case. Case 1 with the coefficient of 0.093 ft^2/day, case 3 with the coefficient of 1.395 ft^2/day, and case 4 with the coefficient of 2.790 ft^2/day are set to be the compared cases to yield a relationship between a diffusion coefficient and cumulative oil production.

Table 5.12: Input data for diffusion model

		Diffusion coefficient	
		ft^2/day	cm^2/s
Case 1	compared case	0.093	0.001
Case 2	reference case	0.930	0.01
Case 3	compared case	1.395	0.015
Case 4	compared case	2.790	0.03

Figure 5.6 presents the comparison of cumulative oil production when considering the diffusive flow with different coefficient constants. From the plot, the total fluid production is increased when considering the diffusive flow, which supports our expectation. The increasing of the coefficient constant slightly increased the cumulative oil production, since the diffusional flux contributes to the fluid flow. Figure 5.7 is generated to zoom in such a result and presents the increased total fluid production by adding the diffusion flow. It is observed that when including the diffusive flow, the total fluid recovery is increased by 2% in 5 years' production at a pore size of 2.4 nm. In addition, with the increasing of the diffusion coefficient, the total fluid production is also slightly

increased. However, this increment is not that significant. Case 2 will be used for further comparison, which has a diffusion coefficient of 0.93 ft^2/day.

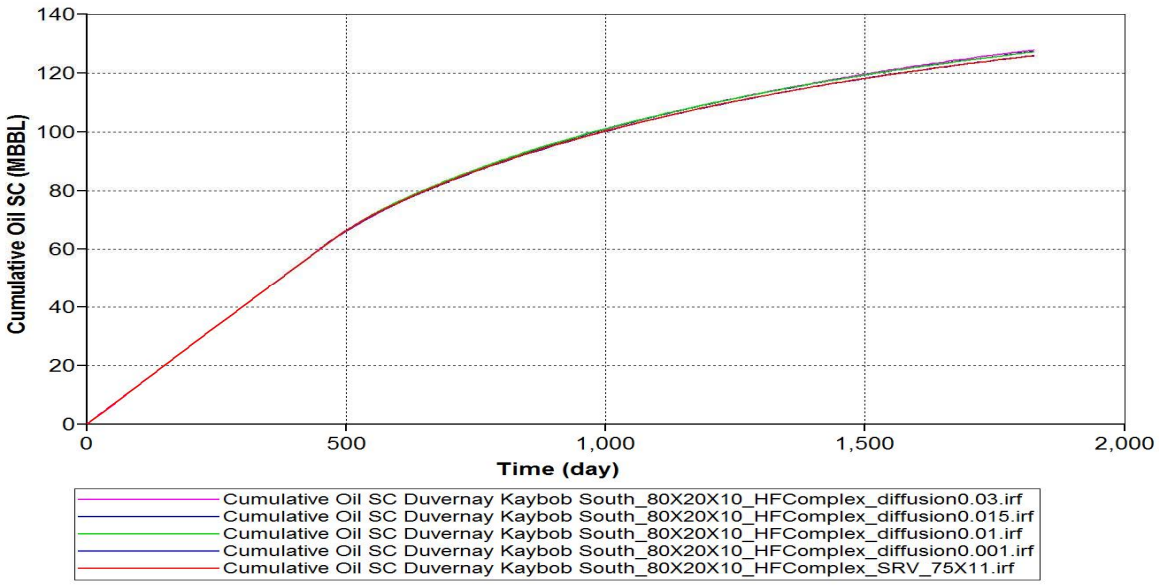

Figure 5.6: Comparison of cumulative oil productions when considering the diffusive flow with different coefficient constants_ original

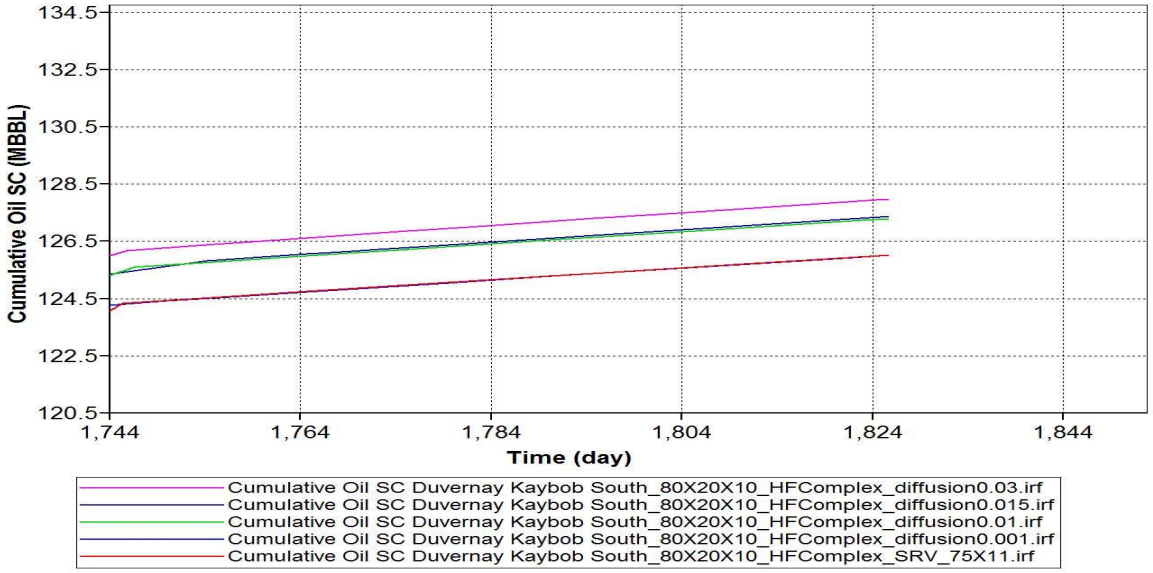

Figure 5.7: Comparison of cumulative oil productions when considering the diffusive flow with different coefficient constants_ zoom in

5.5 Comparison of Confinement Adsorption and Diffusion Effects

In order to evaluate the profoundness of the confinement, adsorption, and diffusion effects, a comparison of these models is developed to define which phenomenon plays the most important role in the oil production, as shown in Figure 5.8.

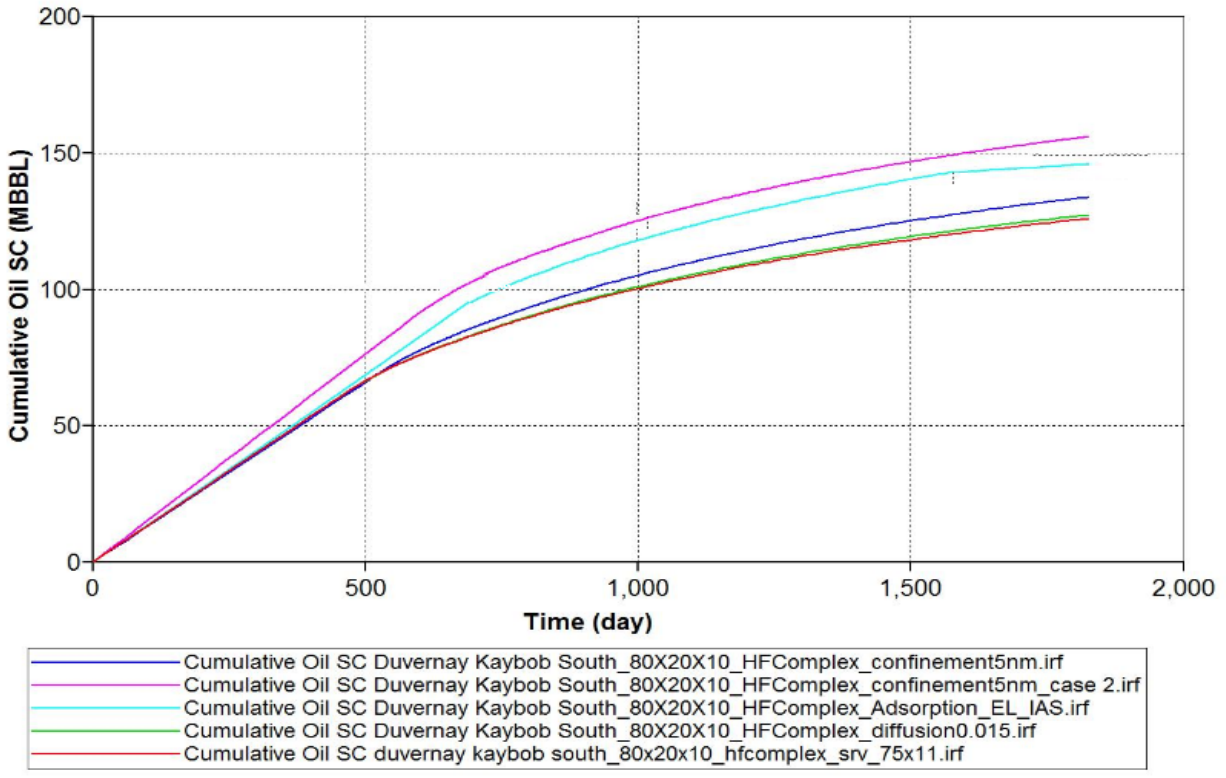

Figure 5.8: Comparison of cumulative oil productions when considering the confinement adsorption and diffusion effects separately

From the above plot, an increment in cumulative oil production is observed when applying the diffusion, adsorption, and confinement models separately. The confinement model with the correction of the adsorption phase density and pore size included increased the oil production the most and then followed by the IAST-EL adsorption model the confinement model that only

considers the pore radius correction, and the diffusion model. In this research at a pore size of 2.4 nm, it is observed that the confinement case 2 can account for 24% of the total fluid production, the IAST-EL adsorption case can account for 21% of the original fluid in place, the confinement case 1 can account for 14% of the total fluid production, and the diffusion process contributes to around 2% of the total fluid recovery in 5 years' production. These results demonstrate that both the confinement effect and the adsorption effect cannot be neglected in modeling of Duvernay shale gas condensate. This study also makes a conclusion that there presents huge differences in shale reservoirs and by considering these phenomena will dramatically increase the cumulative oil production.

Chapter Six: **Conclusions and Recommended Future Work**

6.1 Conclusions

I. In order to model the confinement effect, two case studies are developed and implemented in GEM (2016), where case 1 only considers a pore size and case 2 considers both a pore size and the correction of the adsorbed phase density. It is found that a reduced pore size increased the influence of the confinement effect. This research demonstrates that a nano pore confinement effect cannot be neglected when a pore radius is less than 50 nm. From the simulation results of case 1, it is observed that nano pore confinement can increase the total fluid recovery by 14% at a pore radius of 2.4 nm. Moreover, by considering both the pore size and the correction of the adsorbed phase density, the effect of confinement can account for even about 24% of the total fluid recovery at a pore size of 2.4 nm. Additionally, Monte Carlo simulations of light components and heavy components are performed separately to evaluate the sensitivity of a pore size, the adsorbed phase density, and lumped component's bulk critical properties on components' critical properties. For both light components and heavy components, the combination effect of a pore size and a density correction on critical properties is significant. Accordingly, we need to have sufficient knowledge in obtaining the parameters of a pore size and a corrected adsorbed phase density. For the lumped component, accurately estimating the initial bulk critical temperature is the most important thing in the confinement system.

II. To achieve a successful modelling of the adsorption effect, three different types of models are developed and implemented in GEM (2016), including the ML model, EL model, and IAST-EL model. From the simulation results, it is found out that adsorbed gas can account for 10% of the original fluid in place by applying the ML model and adsorbed gas can

account for 21% of the original fluid in place by applying the EL model. Moreover, by considering a fluid compositional change during pressure depletions and combining with the EL model, adsorbed gas can account for 21% of the original fluid in place at a pore size of 2.4 nm. Additionally, Monte Carlo simulations of light components and heavy components are performed separately to evaluate the sensitivity of the amount of adsorbent, Langmuir volumes, and Langmuir pressures on the amount of gas adsorbed. The deviation forms by a Langmuir volume of CH_4 is observed to be the largest and then followed by the amount of adsorbent in the CH_4 case, the amount of adsorbent in C_{7+} case, and the Langmuir volume of C_{7+}. Consequently, a conclusion can be reached that the Langmuir volume has a more profound effect than the Langmuir pressure and the amount of adsorbent in the adsorption system for both light components and heavy components.

III. Based on a concentration potential gradient, diffusion models are developed and implemented in GEM (2016) to account for the diffusion effect on shale oil and gas production portfolios. The simulation results are used to compare against those models that just consider Darcy's flow in the matrix. It is observed that the diffusion process contributed to the total fluid recovery by 2% in 5 years' productions at a pore size of 2.4 nm. If the diffusive flow is able to be simulated more accurately, the diffusion contributions should be more than that.

IV. Finally, to evaluate the importance of the confinement, adsorption, and diffusion effects, a comparison of these models is carried out to define which phenomenon plays the most important role in the total fluid recovery. In this research at a pore size of 2.4 nm, it is observed that the confinement case 2 can account for 24% of the total fluid production, the IAST-EL adsorption case can account for 21% of the original fluid in place, and the

diffusion process contributed to around 2% of the total fluid recovery in 5 years' productions. These results demonstrated that both the confinement effect and the adsorption effect cannot be neglected in modeling of Duvernay shale gas condensate.

6.2 Recommended Future Work

This study can be extended by the following additions:

I. A hydraulic fracture model can be incorporated with micro seismic data to improve the accuracy of estimation by evaluating the intensity and quality of each micro seismic event.

II. A diffusion model can be extended by introducing a chemical potential gradient as well. Then such a gradient is incorporated with a concentration potential gradient and a pressure gradient to calculate the diffusional flux. This methodology may improve the accuracy of the diffusional estimation, since this method is consistent when a phase is of discontinuity across a matrix-fracture interface.

III. A diffusion model can be improved by separating the effect of molecular diffusion and Knudsen diffusion. Since a pore radius is in the range of micro to nano meters in shale reservoirs, the free path may be greater than a pore diameter to strengthen the molecule-wall collisions.

References

Abdallah Elamin. (2013). *Simulation of Multi-Component Gas Flow and Condensation in Marcellus Shale Reservoir.* Morgantown, West Virginia.

Adelola, G., Adesida, I., Yucel, A., Daniel, E., Resasco, & Chandra, S. R. (2011). *Characterization of Barnett shale pore size distribution using DFT analysis and Monte Carlo simulations*. Denver, CO.

Aguilera, R. and Lopez, B. (2013). *Evaluation of Quintuple Porosity in Shale Petroleum Reservoirs*. Pittsburgh, Pennsylvania. SPE 165681-MS.

Akkutlu, I.Y., & Ebrahim F. (2012). *Multiscale gas transport in shales with local kerogen heterogeneities*. SPE Journal, 17(4).

Alharthy, N.S., Nguyen, T., Kazemi, H., Teklu, T. and Graves, R. (2013). *Multiphase Compositional Modeling in Small-Scale Pores of Unconventional Shale Reservoirs.* New Orleans, Louisiana. SPE 166306-MS.

Al-Ajmi, N., Putthaworapoom, N., Kazemi, H. (2011). *A New Practical Method for Modeling Hydraulic Fracture Propagation in 3-D Space*. San Francisco, California.

Ambrose, R.J., Hartman, R.C., and Akkutlu, I.Y. (2011). *Multi-component Sorbed-phase Considerations for Shale gas-in-place Calculations*. Oklahoma City, Oklahoma, SPE 141416-MS.

Ambrose, R.J., Hartman, R.C., Mery, D., Yucel, A., & Carl, H.S. (2010). *New pore-scale considerations in shale gas in-place calculations*. Pittsburgh, PA.

Arukhe, J. O., Aguilera, R., & Harding, T. G. (2009). *Dominant considerations for effective hydraulic fracturing in naturally fractured tight gas carbonates*. Calgary, Alberta.

Arri, L.E., Yee, D., Morgan, W.D. and Jeansonne, M.W. (1992). *Modeling Coalbed Methane Production with Binary Gas Sorption*. Casper, Wyoming. SPE 24363-MS.

Aslan, E. (2013). *Development and Testing of an Advanced Coalbed Methane Numerical Reservoir Simulator*. The Pennsylvania State University, Pennsylvania.

Ayala, L.F. (2004). *Compositional Modeling of Naturally-Fractured Gas-Condensate Reservoirs in Multi-mechanistic Flow Domains*. The Pennsylvania State University, Pennsylvania.

Ayala, L.F., Ertekin, T. and Adewumi, M. (2006). *Compositional Modeling of Retrograde Gas-Condensate Reservoirs in Multi-mechanistic Flow Domains*. SPE-94856-PA.

Aziz, K. (1993). *Reservoir Simulation Grids: Opportunities and Problems.* Journal of Petroleum Technology. SPE-25233-PA.

Batenburg, D.W., Bosch, M., Boerrigter, P., De Zwart, A. and Vink, J.C. (2011). *Application of Dynamic Gridding Techniques to IOR/EOR-Processes*. The Woodlands, Texas. SPE 141711-MS.

Behrenbruch, P., & Goda H.M. (2006). *Two-Phase Relative Permeability Prediction: A comparison of the modified Brooks-Corey methodology with a new Carman-Kozeny based flow formulation*. Adelaide, Australia.

Bengherbia, M., & Tiab, D. (2002). *Gas-condensate well performance using compositional simulator: a case study*. Calgary, Alberta.

Biterge, M.B. and Ertekin, T. (1992). *Development and Testing of a Static/Dynamic Local Grid Refinement Technique*. SPE-19803-PA.

Bourdet, D., Whittle, T.M., Douglas, A.A. and Pirard, Y.M. (1983). *A new set of type curves simplifies well test analysis*. World Oil Report.

Bourbiaux B.J. (1994). *Parametric study of gas-condensate reservoir behavior during depletion: a guide for development planning*. London, United Kingdom.

Campos, M.D., Yucel, A., & Sigal, R.F. (2009). *A molecular dynamics study on natural gas solubility enhancement in water confined to small pores*. New Orleans, LA.

Chang, M. (1993). *Deriving the Shape Factor of a Fractured Rock Matrix*. Bartlesville, Oklahoma.

Chareonsuppanimit, P., Mohammed, S.A., Robinson, R.L. and Gasem, K. (2012). *High pressure adsorption of gases on shales: Measurements and Modeling*. International Journal of Coal Geology 95 (01).

Chawathe, A., Ertekin, T. and Grader, A. (1996). *Numerical Simulation of Multi-mechanistic Gas-Water Flow in Fractured Reservoirs.* Midland, Texas. SPE 35186-MS.

Cipolla, C.L., Lolon, E.P., Erdle, J.C. and Rubin, B. (2010). *Reservoir Modeling in Shale-Gas Reservoirs*. SPE-125530-PA.

Clarkson, C.R. (2003). *Application of a New Multicomponent Gas Adsorption Model to Coal Gas Adsorption Systems*. SPE-78146-PA.

Clarkson, C.R. and Haghshenas, B. (2013). *Modeling of Supercritical Fluid Adsorption on Organic-Rich Shales and Coal*. Woodlands, Texas. SPE 164532-MS.

Cochran, T.W., Kabel, R.L. and Danner, R.P. (1985). *Vacancy Solution Theory of Adsorption Using Flory-Huggins Activity Coefficient Equations*. AIChEJ 31 (02): 268-277.

Curtis. H, Whitson, Pera, F. & Aud, S. (1999). *Gas condensate relative permeability for well calculation*. Houston. TX.

Curtis, M.E., Ambrose, R.J., Sondergeld, C.H., & Rai, C.S. (2010). *Structural characterization of gas shales on the micro- and nano-scales.* Calgary, Alberta.

Darvish, G.R., Lindeberg, E., Holt, T., Kleppe, J. and Utne, S.A. (2006). *Reservoir Conditions Laboratory Experiments of CO2 Injection into Fractured Cores*. Vienna, Austria. SPE 99650-MS.

Da Silva, F.V. and Belery, P. (1989). *Molecular Diffusion in Naturally Fractured Reservoirs: A Decisive Recovery Mechanism*. SPE 19672

Devegowda, D., Sapmanee, K., Civan, F., & Sigal, R. (2012). *Phase behavior of gas condensates in shales due to pore proximity effects: Implications for transport, reserves and well productivity*. San Antonio, TX.

Du, C.M., Zhang, X., Zhan, L., Gu, H., Hay, B., Tushingham, K. and Ma, Y. (2010). *Modeling Hydraulic Fracturing Induced Fracture Network in Shale Gas Reservoirs as a Dual Porosity System*. Beijing, China. SPE 132180-MS.

Dubinin, M.M. (1960). *The potential theory of adsorption of gases and vapors for adsorbents with energetically non-uniform surfaces*. Chemical Reviews. 60(2). 235-241.

Dunn, L., Schmidt, G., Hammermaster, K., Brown, M., Bernard, R., Wen, E., Befus, R., and Gardiner, S. (2012). *The Duvernay Formation (Devonian): Sedimentology and Reservoir Characterization of a Shale Gas/Liquids play in Alberta, Canada*. Alberta, Canada

Ertekin, T., King, G. and Schwerer, F.C. (1986). *Dynamic Gas Slippage: A Unique Dual-Mechanism Approach to the Flow of Gas in Tight Formations*. SPE-12045-PA.

Fan, L., Billy, W.H., A. Jamaluddin, A., Jairam, K., Robert, M., & Gary, A.P., Alexander, S, & Curtis H. W. (2005). *Understanding gas condensate reservoirs*. Oilfield Review.

Fevang, O., & Whitson, C. (1996). *Modeling gas-condensate well deliverability*. SPE Reservoir Engineering. 11(4). 221–230.

Firincioglu, T., Ozkan, E. and Ozgen, C. (2012). *Thermodynamics of Multiphase Flow in Unconventional Liquids-Rich Reservoirs*. San Antonio, Texas. SPE 159869-MS.

Fisher, M.K., Wright, C.A., Davidson, B.M., Goodwin, A.K., Fielder, E.O., Buckler, W.S. and Steinsberger, N.P. (2002). *Integrating Fracture Mapping Technologies to Optimize Stimulations in the Barnett Shale*. San Antonio. SPE 77441-MS.

Fisher, M.K., Heinze, J.R., Harris, C.D., Davidson, B.M., Wright, C.A. and Dunn, K.P. (2004). *Optimizing Horizontal Completion Techniques in the Barnett Shale Using Micro-seismic Fracture Mapping*. Houston, Texas. SPE 90051-MS.

Gelb, L.D., Gubbins, K.E., Radhakrishnan, R., Sliwinska, M. (1999). *Phase separation in confined systems*. Reports on Progress in Physics.

Ghorayeb, K. and Firoozabadi, A. (2000). *Modeling Multicomponent Diffusion and Convection in Porous Media*. SPE-62168-PA.

Ghorayeb, K., Firoozabadi, A. and Anraku, T. (2003). *Interpretation of the Unusual Fluid Distribution in the Yufutsu Gas-Condensate Field*. SPE 84953-PA.

Guillermo J., Zarragoicoechea, & Victor A. K. (2002). *Vander Waals equation of state for a fluid in a nanopore*. Physical Review E. 65(2).

Haghshenas, B., Clarkson, C.R. and Chen, S. (2013). *Multi-porosity Multi-permeability Models for Shale Gas Reservoirs*. Calgary, Canada. SPE 167220-MS.

Haghshenas, B., Soroush, M., Brohi, I. and Clarkson, C.R. (2014). *Simulation of Liquids Rich Shale Gas Reservoirs With Heavy Hydrocarbon Fraction Desorption*. The Woodlands, Texas. SPE 168968-MS.

Hartman, R.C., Ambrose, R.J., Akkutlu, I.Y., and Clarkson, C.R. (2011). *Shale Gas-in-Place Calculations Part II - Multicomponent Gas Adsorption Effects*. The Woodlands, TX. SPE 144097-MS.

Heinemann, Z.E., Gerken, G. and Hantelmann, G. (1983). *Using Local Grid Refinement in a Multiple-Application Reservoir Simulator*. San Francisco, California. SPE 12255-MS.

Hikley, R., Gu, Z., Wong, T. and Camilleri, D. (2013). *Multi-Porosity Simulation of Unconventional Reservoirs*. Calgary, Canada. SPE 167146-MS.

Hirasaki, G.J. and O'Dell, P.M. (1970). *Representation of Reservoir Geometry for Numerical Simulation*. SPE-2807-PA.

Hoteit, H. and Chawathe, A. (2014). *Making Field-Scale Chemical EOR Simulations a Practical Reality Using Dynamic Gridding*. Muscat, Oman. SPE 169688-MS.

Hoteit, H. and Firoozabadi, A. (2009). *Numerical Modeling of Diffusion in Fractured Media for Gas-Injection and –Recycling Schemes.* SPE-103292-PA.

Hudson, J.D., Civan, F., Michel, G., Devegowda, D. and Sigal, R. (2012). *Modeling Multiple-Porosity Transport in Gas-Bearing Shale Formations.* Mexico City, Mexico. SPE 153535-MS.

Imo-Jack, O. (2010). *PVT characterization of a gas condensate reservoir and investigation of factors affecting deliverability*. Calabar, Nigeria.

Jiang, J., Sanley, I.S., Merijn, S., & Berend, S. (2005). *Adsorption and separation of linear and branched Alkanes on Carbon nano-tube bundles from configurationalbias Monte Carlo simulation*. Physical Review B. 72(4).

Jossi, J.A., Leonard, I.S., & George, T. (2004). *The viscosity of pure substances in the dense gaseous and liquid phases.* AIChE Journal. 8 (1). 59-63.

Kim, B.H., Gyeong-Ho, K., & Yamg-Gon, S. (2003). *Adsorption of Methane and Ethane into single-walled Carbon nano-tubes and slit-shaped carbonaceous pores*. Korean Journal of Chemical Engineering. 20(1). 104-109.

Kilic, A. and Ertekin, T. (2003). *Application of a Local Grid Refinement Protocol in Highly Faulted Reservoir Architectures.* Journal of Canadian Petroleum Technology 42 (04).

Kresse, O., Weng, X., Wu, R. and Gu, H. (2012). N*umerical Modeling of Hydraulic Fractures Interaction in Complex Naturally Fractured Formations*. Chicago, Illinois.

Kulga, B. (2014). *Analysis of the Efficacy of Carbon Dioxide Sequestration in Depleted Shale Gas Reservoirs.* The Pennsylvania State University, Pennsylvania.

Kniazeff, V.J., Nvaille, S. A. (1965). *Two-phase flow of volatile hydrocarbons*. SPE Journal. 5(1). 37-44.

Leahy-Dios, A., Das, M., Agarwal, A., and Kaminsky, R.D. (2011). *Modeling of Transport Phenomenon and Multicomponent Sorption for Shale Gas and Coalbed Methane in an Unstructured Grid Simulator*. Denver, CO. SPE 147352-MS.

Leahy-Dios, A. and Firoozabadi, A. (2007). *Unified Model for Nonideal Multicomponent Molecular Diffusion Coefficients*. AIChEJ 53 (11).

Lenormand, R., Romancer, J.K., Gallo, Y. and Bourbiaux, B. (1998). *Modeling the Diffusion Flux between Matrix and Fissure in a Fissured Reservoir*. New Orleans, Louisiana. SPE 49007-MS.

Lin, A. and Ma, J. (2015). *Stimulated-Rock Characteristics and Behavior in Multistage Hydraulic-Fracturing Treatment.* SPE-167716-PA.

Loucks, R.G., Robert, M.R., Stephen, C. R., & Daniel, M. J. (2009). *Morphology, genesis, and distribution of nanometer-scale pores in siliceous mudstones of the Mississippian Barnett shale*. Journal of Sedimentary Research. 79.

Lu, X., Li, F. and Watson, A.T. (1995). *Adsorption Studies of Natural Gas Storage in Devonian Shales*. SPE-26632-PA.

Manik, J. (1999). *Compositional Modeling of Enhanced Coalbed Methane Recovery*. The Pennsylvania State University, Pennsylvania.

Manik, J., Ertekin, T. and Kohler, T.E. (2002). *Development and Validation of a Compositional Coalbed Simulator.* Journal of Canadian Petroleum Technology 41 (04).

Mayerhofer, M.J., Lolon, E., Warpinski, N.R., Cipolla, C.L., Walser, D.W. and Moortgat, J. and Firoozabadi, A. (2013). *Fickian Diffusion in Discrete-Fractured Media from Chemical Potential Gradients and Comparison to Experiment.* Energy & Fuels 27 (10).

Miskimins, J. L., Lopez-Hernandez, H.D., Barree, R.D., & Assocs. (2005). *Nondarcy flow in hydraulic fractures: does it really matter*. Dallas, TX.

Mott, R., Andrew, C., & Mike, S. (1999). *A New Method of Measuring Relative Permeabilities for Calculating Gas-Condensate Well Deliverability*. Houston, TX.

Moncrieff, J., Sondergeld, C., Ambrose, R., & Rai, C. (2010). *Micro-structural studies of gas shales*. Pittsburgh, PA.

Morishige, K. & Shikimi, M. (1998). *Adsorption hysteresis and pore critical temperature in a single cylindrical pore.* Journal of Chemical Physics. 108 (18). 7821-7824.

Muskat, M. & Meres, M.W. (1936). *The flow of heterogeneous fluid through porous media.* Jurnal of Applied Physics. 7(9). 346-363.

Myers, A.L. and Prausnitz, J.M. (1965). *Thermodynamics of Mixed-Gas Adsorption*. AIChEJ 11 (01): 121-127.

Myers, A.L., and Sircar, S. (1972). *Analogy between Adsorption from Liquids and Adsorption from Vapors.* J.Phys. Chem. 76 (23).

Nacul, E.C. and Aziz, K. (1991). *Use of Irregular Grid in Reservoir Simulation*. Dallas, Texas. SPE 22886-MS.

Nojabaei, B., Johns, R.T. and Chu, L. (2013). *Effect of Capillary Pressure on Phase Behavior in Tight Rocks and Shales*. SPE-159258-PA.

Orangi, A., Nagarajan, N. R., Honarpour, M. M., & Rosenzweig, J. (2011). *Unconventional shale oil and gas-condensate reservoir production, impact of rock, fluid, and hydraulic fractures.* The Woodlands, TX.

Ortiz, V., Lopez Y.M. & Lopez, G.E. (2005). *Phase diagrams and capillarity condensation of methane confined in single- and multi-layer nanotubes*. Molecular Physics. 103 (19). 2587–2592.

Panagiotopoulos, A.Z., (1987). *Direct determination of phase coexistence properties of fluids by Monte Carlo simulation in a new ensemble*. Molecular Physics. 61(4). 813-826.

Peaceman, D.W. (1983). *Interpretation of Well-Block Pressures in Numerical Reservoir Simulation with Non-square Grid Blocks and Anisotropic Permeability*. SPE-10528-PA.

Pedrosa, O. and Aziz, K. (1986). *Use of a Hybrid Grid in Reservoir Simulation*. SPE-13507-PA.

Peng, D., and Robinson, D.B. (1976). *A New Two-Constant Equation of State*. Chem. Fundament. 15 (1): 59-64.

Peterson, B.K., Keith,E., Gubbins, G.S., Heffelfinger, U. M., Bettolo, M., & Frank, V. S. (1988). *Lennard-Jones fluids in cylindrical pores: Nonlocal theory and computer simulation.* Journal of Chemical Physics 88 (10).

Qi, Z., Sinopec, Z., Baosheng, L., Ruijian, D., Zhimin, Du., Shouping, W. & Wei, Z. (2007). *Phase behavior study in the deep gas-condensate reservoir with low permeability*. London, U.K.

Quandalle, P. (1983). *The Use of Flexible Gridding for Improved Reservoir Modeling*. San Francisco, California. SPE 12239-MS.

Rahmani, B. D. (2012). *Multi-component shale gas in-place calculations*. University of Oklahoma, Norman, OK.

Rajput, V. (2012). *A Production Performance Prediction and Field Development Design Tool for Coalbed Methane Reservoirs: An Artificial Neural Network Approach.* The Pennsylvania State University, Pennsylvania.

Remner, D.J., Ertekin, T., Sung, W. and King, G.R. (1986). *A Parametric Study of the Effects of Coal Seam Properties on Gas Drainage Efficiency.* SPE-13366-PA.

Robertson, G.E. (1978). *Grid-Orientation Effects and the Use of Orthogonal Curvilinear Coordinates in Reservoir Simulation*. SPE-6100-PA.

Roque-Marherbe, R. (2007). *Adsorption and Diffusion in Nanoporous Materials*. CRC Press, New York.

Ruthven, D.W. (1984). *Principles of Adsorption and Adsorption Processes.* Wiley, New York.

Samandarli, O., Ahmadi, H.A. and Wattenbarger, R.A. (2011). *A New Method for History Matching and Forecasting Shale Gas Reservoir Production Performance with a Dual Porosity Model*. The Woodlands, TX. SPE 144335-MS.

Sanaei, A., Jamili, A. and Callard, J. (2014). *Effect of Pore Size Distribution and Connectivity on Phase Behavior and Gas Condensate Production from Unconventional Resources*. The Woodlands, Texas. SPE 168970-MS.

Sapmanee, K. (2011). *Effect of pore proximity on behavior and production of Gas Condensate.* University of Oklahoma. Norman, OK.

Sarma, P. and Aziz, K. (2006). *New Transfer Functions for Simulation of Naturally Fractured Reservoirs with Dual Porosity Models.* SPE-90231-PA.

Schettler, P.D., Parmely, C.R. and Lee, W.J. (1989). *Gas Storage and Transport in Devonian Shales*. SPE-17070-PA.

Shree, V. and Ertekin, T. (1996). *A Patch-Type Adaptive Local Grid Refinement Technique and Its Application to Horizontal Wells.* Columbus, Ohio. SPE 37352-MS.

Sigmund, P.M. (1976). *Prediction of Molecular Diffusion at Reservoir Conditions. Part 1– Measurement and Prediction of Binary Dense Gas Diffusion Coefficients*. Journal of Canadian Petroleum Technology 15 (02).

Singh, S.K., Sinha, A., Deo, G. and Singh, J.K. (2009). *Vapor-Liquid Phase Coexistence, Critical Properties, and Surface Tension of Confined Alkanes*. The Journal of Physical Chemistry 113 (17): 7170-7180.

Sircar, S. (1970). *Thermodynamic Studies of Adsorption at the Liquid-Solid Interfac*e. University of Pennsylvania, Philadelphia, Pennsylvania.

Sircar, S., and Myers, A.L. (1970). *Statistical Thermodynamics of Adsorption from Liquid Mixtures on Solids. I. Ideal Adsorbed Phase*. J.Phys. Chem. 74 (14): 2828-2835.

Siripatrachai, N. (2014). *Development of a Multi-mechanistic, Triple-porosity, Triple-permeability, Compositional Model for Unconventional Reservoirs*. The Pennsylvania State University, Pennsylvania.

Sondergeld, C. H., Newsham, K. E., Comisky, T. E., Rice, M. C. & Rai, C. S. (2010). *Petrophysical considerations in evaluating and producing shale gas resources.* Pittsburgh, PA.

Spivak, A. (1974). *Gravity segregation in two-phase displacement process*. SPE Journal 14(6).

Stevenson, M.D., Pinczewski, W.V., Somers, M.L. and Bagio, S.E. (1991). *Adsorption/Desorption of Multicomponent Gas Mixtures at In-Seam Conditions*. Perth, Australia. SPE 23026-MS.

Sun, H., Chawathe, A., Hoteit, H., Shi, X. and Li, L. (2015). *Understanding Shale Gas Flow Behavior Using Numerical Simulation*. SPE-167753-PA.

Telku, T.W., Alharthy, N., Kazemi, H., Yin, X., Graves, R. and Alsumaiti, A. (2014). *Phase Behavior and Minimum Miscibility Pressure in Nano-pores.* SPE-168865-PA.

Thararoop, P. (2010). *Development of a Multi-mechanistic, Dual-porosity, Dual permeability, Numerical Flow Model for Coalbed Methane Reservoirs Accounting for Coal Shrinkage and Swelling Effects*. The Pennsylvania State University, Pennsylvania.

Vaibhav H Rajput. (2016). *Development of a Compositional Simulator for Liquid -Rich Shale Reservoirs.* The Pennsylvania State University, Pennsylvania.

Wan, T., Meng, X., Sheng, J. and Watson, M. (2014). *Compositional Modeling of EOR Process in Stimulated Shale Oil Reservoirs by Cyclic Gas Injection.* Tulsa, Oklahoma. SPE 169069-MS.

Wan, T. and Sheng, J. (2015). *Compositional Modeling of the Diffusion Effect on EOR Process in Fractured Shale-Oil Reservoirs by Gas-flooding*. Journal of Canadian Petroleum Technology 54 (02). 107-115.

Wang, L., Parsa, E., Gao, Y., Ok, J., Neeves, K., Yin, X. and Ozkan, E. (2014). *Experimental Study and Modeling of the Effect of Nano-confinement on Hydrocarbon Phase Behavior in Unconventional Reservoirs*. Denver, Colorado. SPE 169581-MS.

Wang, Y., Yan, B. and Killough, J. (2013). *Compositional Modeling of Tight Oil Using Dynamic Nanopore Properties*. New Orleans, Louisiana. SPE 166267-MS.

Wang, F. P., & Reed, R. M. (2009). *Pore Networks and Fluid Flow in Gas Shales*. New Orleans, LA.

Warpinski, N.R., Mayerhofer, M.J., Vincent, M.C., Cipolla, C.L. and Lolon, E. (2008). *Stimulating Unconventional Reservoirs: Maximizing Network Growth While Optimizing Fracture Conductivity*. Keystone, Colorado. SPE 114173-MS.

Warpinski, N.R., Wolhart, S.L. and Wright, C.A. (2004). *Analysis and Prediction of Microseismicity Induced by Hydraulic Fracturing*. SPE-87673-PA.

Warren, J.E. and Root, P.J. (1963). *The Behavior of Naturally Fractured Reservoirs*. SPE-426-PA.

Wheaton, R. J., & Zhang, H. R. (2000). *Condensate banking dynamics in gas condensate fields: compositional changes and condensate accumulation around production wells*. Dallas, TX.

Whitson, C.H., Lei, G. and Cheng, N. (2014). *Liquid-Rich Shale versus Conventional Depletion Performance*. Vienna, Austria. SPE 167788-MS.

Whitson, C.H. and Sunjerga, S. (2012). *PVT in Liquid-Rich Shale Reservoirs*. San Antonio, Texas. SPE 155499-MS.

Wilke, C.R. and Chang, P. (1955). *Correlation of Diffusion Coefficients in Dilute Solutions.* AIChEJ 1 (02) 264-270.

Wu, Y., Li, N., Wang, C., Ran, Q., Li, J. and Yuan, J. (2013). *A Multiple-Continuum Model for Simulation of Gas Production from Shale Gas Reservoirs*. Abu Dhabi, UAE. SPE 165991-MS.

Xiong, Y., Winterfeld, P.H., Wang, C., Wu, Y. and Huang, Z. (2015). *A Compositional Model Fully Coupled With Geomechanics for Liquid-Rich Shale and Tight Oil Reservoir Simulation*. Houston, Texas. SPE 173261-MS.

Yang, R.T. (1987). *Gas Separation by Adsorption Processes*. Boston, Massachusetts: Butterworth.

Yuan, P. and Laura, S. (2006). *Equations of state in a lattice Boltzmann model*. Physics of Fluids. 18(4).

Zarragoicechean G.J., and Kuz, V.A. (2004). *Critical shift of confined fluid in a nano pore*. Fluid Phase Equilibria. 220(1).7-9.

Zhilin, Qi. Baosheng, L., Ruijian, D., Zhimin, D., Zhimin, W., & Wei, Z. (2007). *Phase Behavior Study in the Deep Gas-Condensate Reservoir with Low Permeability*. London, UK.

Zhou, C., Hall, F., Gasem, K. and Robinson, R.L. (1994). *Predicting Gas Adsorption Using Two-Dimensional Equations of State*. Ind. Eng. Chem. Res. 33 (05).1280-1289.